Project Number: CHE-JW1-0307

NUMERICAL STUDIES OF ZINC OXIDE SYNTHESIS VIA PHYSICAL VAPOR TRANSPORT

A Major Qualifying Project Report:
submitted to the Faculty
of the
WORCESTER POLYTECHNIC INSTITUTE
in partial fulfillment of the requirements for the
Degree of Bachelor of Science

by

Diana M. Otálvaro
Date: March 2, 2007

Approved:

Professor Jennifer Wilcox, Major Advisor

1. zinc oxide
2. growth from vapor
3. numerical modeling

Professor Tawatchai Charinpanitkul, Co- Advisor

Abstract

This project examined the transport phenomena occurring in the synthesis of zinc oxide by physical vapor transport. In the numerical simulations zinc and oxygen were treated as diluted species transported in a nitrogen medium. The modes of transport were investigated and the velocity, temperature and concentration profiles in the reactor under reaction conditions elucidated. Also a parametric examination was conducted to determine the effect of physical variables on the flow. It was found that in open reaction conditions at high pressures convective transport dominates, while lower pressures lead to diffusive dominance and significant mass transport resistance. The linear temperature profile assumption was validated; further it was found that thermal expansion is insignificant, hence free convection can be neglected.

Executive Summary

As the urge to develop materials suitable for the rapidly developing optical and microprocessor industries becomes more pronounced, zinc oxide presents itself as a promising alternative in the search of developing electronic and optical materials at the nanolevel. The wide band gap of ZnO crystal coupled with its high exciton binding energy make ZnO a coveted n-type semiconductor. Similarly the surface and quantum effects arising from the vibration of surface atoms make ZnO a highly desirable material in the optical industry given its capacity to emit infrared light. To fully exploit these properties, the synthesis and growth of ZnO aggregates must be meticulously controlled, since these properties stem from the particular morphology of the resulting aggregates. The preferred method of ZnO synthesis is physical vapor transport, PVT. In PVT, the metal reactant sublimes from a powder form forming a vapor and is then carried along with the reacting gas through the reactor chamber; the species are transported in an inert gas which aids in the reacting process by providing a medium through which both species can interact. PVT is favored over other synthesis processes due to the higher diffusivities of the species in the gas phase as compared to the liquid phase and also due to the purity of the resulting materials.

In ZnO synthesis by PVT there are a multitude of variables that have been identified as influencing the final product and many more remain that need identification. Moreover, the complex interplay of these variables may provide confounding observations. In order to better understand the conditions that lead to one type of morphology over another, it is important to understand the flow and transport conditions in the reactor. Computational fluid dynamics, CFD, a vigorously growing branch of fluid mechanics, provides a powerful tool for understanding transport phenomena. There is a gamut of different codes upon which CFD is based; nevertheless, they all share a basic structure. In CFD the non-linear, partial integral difference equations that govern momentum, mass and energy transport are solved by first discretizing these equations to render a set of algebraic equations and then solving the resulting linear system in a finite grid. Thus the result of CFD codes comes in the form of information about the state of the desired variables in

each cell, which effectively give positional profiles. Computational fluid dynamics is particularly attractive since it allows us to conduct parametric analysis at an insignificant lower cost as compared to an experimental setting, thus proving useful in determining the behavioral trends of a given system

This major qualifying project is concerned with modeling physical vapor transport in the ZnO synthesis system. The project comprises two main objectives. The first is to acquaint the author with the partial differential equation solver COMSOL Multiphysics®, which serves as a tool for solving the highly non-linear equations that result from transport phenomena. To accomplish such goal, the author has developed a number of models related directly to the PVT system. The complexity of the models rises with each simulation, as the ultimate goal is to produce a model that realistically represents the physical system. A second goal involves the analysis of the computational results as they apply to the PVT system. The interest is to understand how flow characteristics influence crystal growth. This information can then be used to modify existing experimental settings.

A total of four sets of models were completed, each at a different level of complexity. The first set of models is concerned with the relative dominance of convective and diffusive flux under reaction conditions. Determining which mass transport mode dominates at different sections of the reactor chamber can help us elucidate the deposition patterns observed in experimental settings, as well as to evaluate the influence of mass transfer resistance in the reaction kinetics. A second set of models focuses on multicomponent, low pressure PVT. In this pressure regime Maxwell-Stefan diffusion predominates; in this transport mode the interaction between solutes and solvent are more intricate and diffusivities become concentration dependent and are hence anisotropic. Moreover, in this set of models reaction is incorporated as a diffusive transport term at an interface. Understanding the interactions between reacting and non-reacting species can help us elucidate the mechanisms by which reaction occurs. Further, a third set of models treats non-isothermal fluid energy interactions. In this set of models the effect of temperature gradients on the concentration and velocity distribution were investigated. This set of models offers a more realistic approach to PVT as it occurs in experimental conditions; in particular, it is of interest to determine if there is free convection in the

reactor chamber, as it might lead to recirculation patterns and non-uniform growth at the crystal interface. Lastly, we have incorporated all the intricacies of PVT modeling into a fourth model, which seeks to recreate the results obtained by Tena-Zaera on the ZnO system.

From the models it was seen that under the experimental conditions at Chulalongkorn University convective transport may be dominant in all but the vicinity of the crystal-vapor interface. Moreover, the results of this simulation suggest that at low pressures, of the order of 10^{-2} atm, there may be counter diffusion of the inert component nitrogen in the vicinity of the crystal interface which could lead to recirculation. These results allow us to make the suggestion that the pressure drop in the reactor should be carefully monitored to prevent convection to override diffusion, which is part of the mechanism by which reaction is thought to occur; moreover, the value of the Peclet number at experimental conditions suggests that mass transport limitations introduced by low diffusivities may be the kinetically limiting step in the conversion of O_2 to ZnO. The results of the second set of models provided important insight about the reacting species' concentration profiles along the reactor. It was shown that, in spite of concentration gradients that may induce pressure driven convection, diffusive transport was dominant in the whole domain. The streamlines for the flow were shown to be linear and the concentration gradient was nearly constant thus leading naturally to the conclusion that diffusive transport is, in fact, the dominant transport mode. Interestingly, the simulation results show that the flow is two-dimensional, as diffusive flux of both species is observed in the radial as well as in the axial direction, although the latter is dominant. The non-isothermal simulations allowed us to quantify the magnitude of thermal expansion in the chamber at experimental conditions. It was shown that this expansion is of the order of 0.0035% which allows us to neglect the compressibility of the system in our calculations and thus disregards the possibility of significant free convection. Moreover, a constant gradient temperature profile was observed, which complied well with the experimental profile. Finally, a clear laminar velocity profile was obtained from these simulations reinforcing the absence of free convection.

Acknowledgments

The results of this work are not only my own. I have a debt of gratitude with so many people that played a part on it coming to a successful conclusion. I would like to thank Professor Jennifer Wilcox and Acaan especially. Not only were they my advisors, but they also showed an inspiring enthusiasm throughout the project leading me to new ways of learning. Also, it was because of their open mind and love of science that I was able to fulfill my dream of coming to Thailand. I owe a special thank you to Thailand as a whole, for the gentle warmth of its beautiful people, who greeted me always with a smile and made me feel less of a farang; but also, to the land, whose sometimes exuberant, sometimes calm beauty inspired my work throughout. I must also thank my colleagues at the CEPT lab; a group of happy, active and talented people, who bestow an unmistakable spirit of joy to the lab and to everyone that works in it. To my friend Eve for her company and friendship and to my friend and partner Tee who provided me with experimental data for my work. To IGSD and WPI I owe a debt that I cannot repay, for their flexibility, understanding and indefatigable efforts that made the logistics of my travel possible. From WPI I must thank Dr. Adriana Hera and Dr. Siamak Najafi especially without whose efforts I could not have performed my simulations. Last, but not least, I would like to thank Vicky, Cody, Gabe, Ravi, Kyle and the Mademoiselle Julie with whom I enjoyed the chaos of Bangkok and the evenings at Suskit. I leave Thailand with an ailing that seeks to return as soon as possible.

TABLE OF CONTENTS

Table of Figures

List of Tables

Introduction

The scientific phenomena that have marveled and confounded scientist for decades are presently being understood by a mixture experimental and computational results. The latter is a powerful tool to gauge the trends of a given system and its response to changes in the parameters that define it. Though experimental data is of vital importance and can never be fully supplanted by simulations, these offer the advantage of providing results at a relative low cost as compared to costly parametric analysis in laboratory settings. Moreover, as the microprocessor industry vigorously grows both in size and product capabilities, it is becoming increasingly advantageous to develop theoretical models of a particular system to solve by discrete computational methods. In fact, it is now possible to couple transport phenomena with reaction kinetics in what is a more comprehensive model of chemical reaction engineering.

Zinc oxide is a crystalline material whose optical properties and conductivity capacities have rendered it the interest of the microprocessor and optical industries. Nevertheless, to fully exploit its powerful properties, the synthesis and growth of ZnO nano particles must be understood and controlled. Although many methods of synthesis are available, physical vapor transport, PVT, is largely favored due to the purity of the resulting material and the favorable kinetics of the mechanism. However, PVT is a complex mechanism as it incorporates a multitude of variables that account for the interplay of momentum, mass and energy transport. Modeling PVT is a challenging but fascinating task which is ultimately accompanied by important results.

This major qualifying project is concerned with modeling physical vapor transport in the ZnO synthesis system. The project comprises two main objectives. The first is to acquaint the author with the partial differential equation solver COMSOL Multiphysics®, which serves as a tool for solving the highly non-linear equations that result from transport phenomena. To accomplish such goal, the author has developed a number of models related directly to the PVT system. The complexity of the models rises with each simulation, as the ultimate goal is to produce a model that realistically represents the physical system. A second goal involves the analysis of the computational results as they apply to the PVT system. The interest is to

understand how flow characteristics influence crystal growth. This information can then be used to modify existing experimental settings.

Background

ZnO synthesis model

The multiple relevant uses of ZnO in various fields have spurred a keen interest in development of a cost-effective method of ZnO synthesis at an industrial level. Many efforts have been and are currently being made to optimize ZnO synthesis and to understand the mechanism of ZnO nucleation and growth.

Properties of ZnO single crystals

The material, ZnO is a crystalline solid. Its crystalline structure corresponds to that of wurzite as shown in Figure 1.

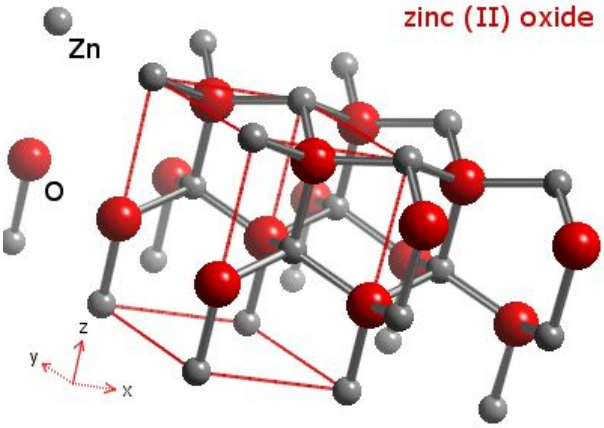

Figure 1: ZnO crystal structure (WebElements, 2007)

Zinc oxide displays important properties that make it a coveted material in many industrial sectors ranging from user commercial applications to biomedical applications. In particular, ZnO possesses high strength and wear resistance making it highly relevant in the manufacture of high-performance materials. In addition, since ZnO is a n-type semiconductor with a wide band gap of 3.37 eV and a large exciton binding energy of 60 meV its crystal is extremely desirable in electronic applications. When doped with some impurities zinc oxide's conductivity properties are further enhanced. Moreover, the optical industry finds in ZnO a nearly ideal material with powerful optical properties arising from its surface effects and quantum size effects.

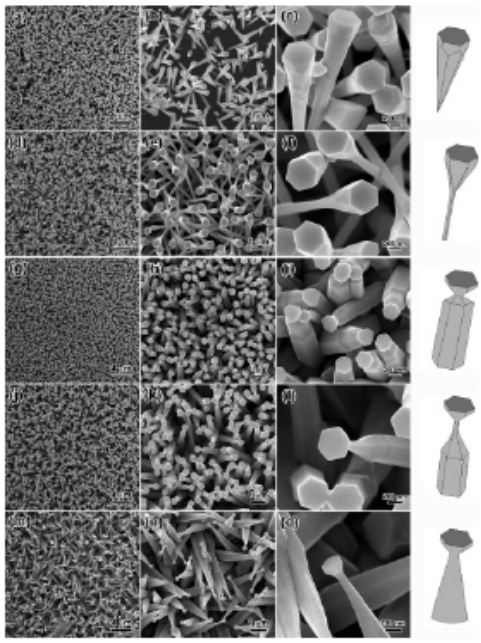

Interestingly, ZnO aggregates come in a multitude of different morphologies at a nanolevel. Each of these morphologies possesses distinct properties that make them specific for different industries. Some examples of different ZnO morphologies can be found in the extensive work done by Shen et al. who reports obtaining up to five distinct ZnO morphologies at the nano-level by monitoring thermodynamic conditions.

Figure 2: different morphologies of ZnO (Shen, 2006)

In fact, much effort has been invested to determine the variables that give rise to such a variety of ZnO morphologies. These morphologies can be highly ordered; in addition to displaying important physical, electronic and optical properties, they have a high degree of aesthetic value. The crystal morphologies obtain a wide range of classification, a brief list of which will be summarized. Zinc oxide can adopt the shape of spheroid nanoparticles, nanobelts and nanorings, nanowires, polycrystalline nanowires within nanochannels of porous alumina, vertically well-aligned nano-needles and nano-tetrapods. Particular interest is placed on nanowires and nano-tetrapods. Indeed, the literature on the synthesis of these two structures is voluminous. More specifically, nanowires are attractive due to their optical and electronic properties, given by their wide band gap and exciton binding energy. Zinc oxide in this form has been reported to be important in the fabrication of nanolasers. Similarly, ZnO nano-tetrapods are of interest for a number of applications. Zhang argues that this morphology has enhanced infrared light absorption as compared to ZnO nanoparticles, which is a result of the high surface to volume ratio of this structure. The optical properties of ZnO are explained by the vibration of surface atoms in the {1 0 10} plane. Such vibration serves to transform light energy into kinetic and heat energy. The electronic movement of nanowhiskers changes according to the number of electrons in the zinc surface at the center of the nanowhiskers. Furthermore, there is a large

dipole layer formed at the interface of the Zn and Zn oxide, which serves as a potential trap for electron capture. The capacity to absorb IR light is attributed to lattice distortion and the surface effects of nanowhiskers, as reported by Wu et al. Lattice distortions can be a result of compressing stress caused by a lattice defect. In addition the adsorption coefficient is directly proportional to the imaginary number of the dielectric function which is determined by lattice distortion. Preliminary studies focus on the use of this specific tetrapod form of the crystal in microbacterial applications (Tawatchai, et al.)

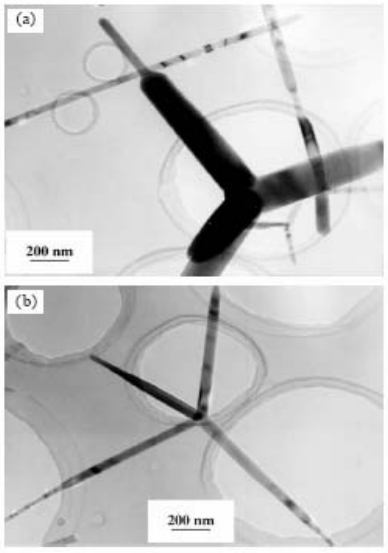

Figure 3: TEM image of ZnO tetrapods (Zhang, 2005)

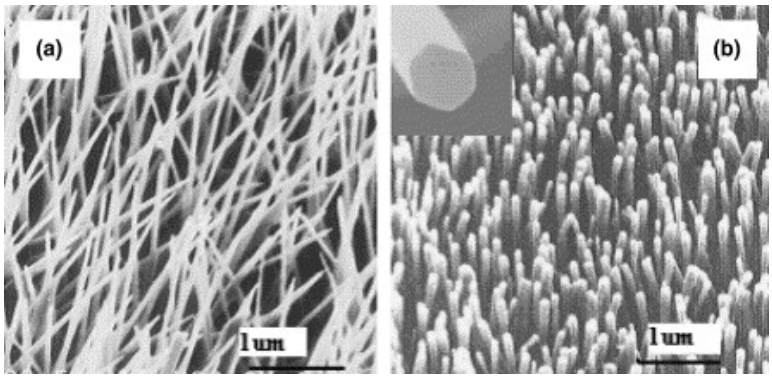

Figure 4: TEM image of highly ordered ZnO nanotubes (Zhang, 2005)

Synthesis methods and resulting morphologies

As any other crystal valued for its rich properties in industrial applications, growth control of ZnO plays a fundamental role in its synthesis. Particularly, much emphasis is placed on the ability to control the size, uniformity, selective growth and alignment of the structures. A variety of methods have been devised to induce one structure over another. Many of these focus in the control of thermodynamic variables. Park et al. have devised a method by which they can control the length to diameter ratio of the nanowires synthesized by the chemical vapor transport and condensation method, CVTC. To do so they stoicheometrically restrict the concentration of molecular oxygen in the reaction chamber. They refer to this method as the two-step gas-flow-controlled evaporation process. In this process, a stream of inert gas

purge is initially injected into the chamber, then the reacting gas, oxygen, is injected downstream of the chamber's entrance. The position of oxygen injection along the axial direction was controlled, since it had been found that undesired crystallization early on

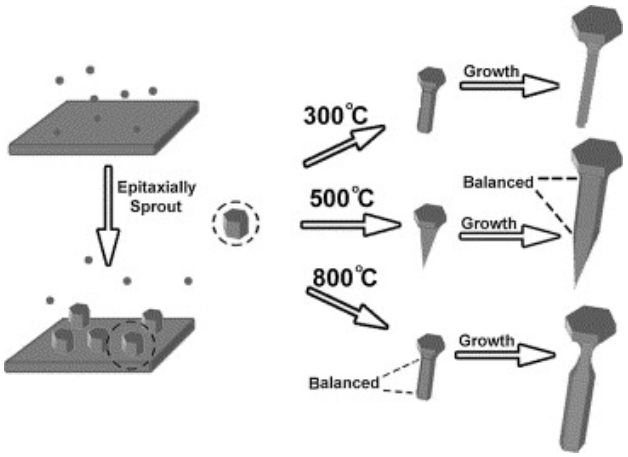

Figure 5: temperature dependent ZnO morphologies (Shen, 2006)

the chamber entrance resulted from Zn vapor back diffusion and its encounter with oxygen. A different approach to the synthesis was proposed by Zhang et al., by which synthesis is achieved without either a carrier gas or a metal catalyst by fine tuning the heating rates. In their work they report obtaining four distinct ZnO morphologies, e.g., nanobelts and nanorings, nanowires, polycrystalline ZnO nanowires and vertically-well-aligned nanoneedles, each of which occurs at a different regime of heating rates at different pressures.

Furthermore, in their work they venture to propose an explanation of the effect of heating rate in morphology. They argue that at heating rates less than 34°C/min, crystal growth rate along the solid liquid interface is kinetically limited. Diffusion is fast with respect to crystal growth thus giving rise to uniform concentration that in turn results in growth along the entire solid-liquid interface. This mechanism, they argue, gives rise to nanobelts and nanorings. The same thought process is used to explain the morphology at high heating rates. In this case growth increased with respect to diffusion rate, so that the concentration of atoms at the interface was depleted, hence growth becomes diffusion limited. Zhang found that in this regime ZnO nanowires form. The appearance of tetrapods at heating rates above 170 °C/min, is explained by proposing that at that rate the local vapor becomes supersaturated with Zn and ZnO precipitates. Since the vapor is supersaturated at the interface multiple nucleation sites arise hence resulting in the peculiar tetrapod morphology. Yet another study conducted by Wu et al.

identifies evaporation temperature and gas pressure as the key variables that influence different ZnO morphologies. Wu found that the diameter of the tetrapods increased and the ratio of length to diameter decreased with increasing temperature within a certain pressure range. Also the amount of Zn phase inside the nanowhiskers increased with increasing temperature. Moreover, Wu's group proposed a mechanism of zinc oxidation. In this mechanism zinc is first deposited on a graphite crucible, upon heating Zn vapor diffuses in an argon-oxygen atmosphere by a thermal buoyancy force. Since oxygen is lighter than argon, oxygen diffuses downward, hence the Zn vapor first comes into contact with molecular oxygen. Following the collision of the two species a diffusion convection process between Zn nuclei vapor and oxygen gives rise to the growth of the amorphous ZnO nanowhiskers.

Furthermore, Shen's group used a metal vapor deposition method, MVD, toward ZnO synthesis. In comparison to the methods discussed above, MVD is particularly attractive from an industrial standpoint given its lower temperature requirements and the use of Zn powder as a source. Interestingly, Shen associates the appearance of different structures to the concentration of indium in the In film used as a support for Zn powders. By keeping all variables constant throughout five experimental rounds and finding different morphologies, Shen et al. concluded that this phenomenon is directly related to the concentration of In, since In is consumed from round to round. In their growth model, complex nanostructures are nucleated by solid ZnO, i.e., Zn sub oxide and liquid Zn in metal droplets. They provide an explanation for this phenomenon by which the concentration of In has repercussions on the morphology since ZnO is nucleated by $In_2O_3(ZnO)_n$ complexes, where n is correlated with In concentration.

Regardless of the specific method of synthesis, formation of ZnO is comprised of two distinct steps, nucleation and growth (Zhou, 2005). In his work, Zhou claims that being able to control the rate of ZnO growth by restricting the injection of O_2 into the reaction chamber to slow down growth. The depleted oxygen concentration gives rise to effective contact at the interface which aids in ensuring a continuous reaction between oxygen and zinc. Indeed, they propose that the ideal ratio of oxygen to zinc is 35.791 mol of oxygen per mol of zinc. In the mechanism of ZnO synthesis, the authors suggest three distinct stages, namely Zn oxidation, nucleation and crystal growth. The first of these steps is adjusted by supplying inadequate

oxygen gas, so that oxygen becomes the determining reagent and zinc in turn becomes the excess reagent. Then the kinetic parameters can be deduced from O_2 consumption in the fist reaction stage. In their kinetic study, Zhou et al. have employed a modified form of the kinetic equation, Equation 1.

A plot of $\ln\left(\frac{[O_2]_0}{[O_2]_t}\right)$ vs. time has a sigmoidal shape. Since the slope of the curve corresponds to the kinetic rate constant, k, it can be deduced that in fact ZnO formation is comprised of two distinct kinetic states that are associated with nucleation and growth. In fact, Zhou's team found that the overall reaction is second order with respect to the oxygen concentration, but each individual kinetic step is first order with O_2 concentration. They report that the nucleation step is achieved within the first 0.5-1.5 minutes of reaction, where as the needle crystal growth encompasses the following 2.5 to 6 minutes of reaction. Moreover, they have found a kinetic rate constant for nucleation of 0.30 min^{-1} and a

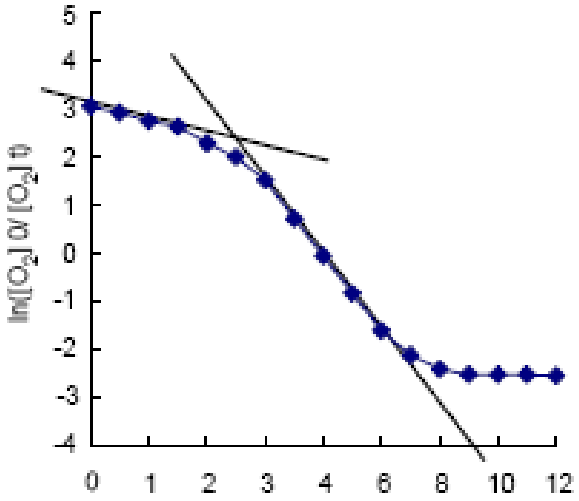

Figure 6: kinetic treatment of ZnO synthesis and growth (Zhou, 2005)

corresponding constant of 1.08 min^{-1} for crystal growth. In addition, they found that raising the temperature favors the second reaction stage following the equation

Evidence of the temperature dependence of the second stages was obtained experimentally. When the temperature was increased from 973 to 1153°C the length of the needle increased from 12 to 88 micrometers, while the basal diameter decreased from 2.6 to 1.8 micrometers. The axial length is associated directly to growth, while the basal diameter is closely related to

nucleation. The temperature dependence of the second stage can be understood via a parametric form of the Arrhenius expression modified to comply with Equation ---,

$$\ln(k) = -\frac{E}{RT} + B$$

Equation 1

Where $B = \ln\left(k_0\right)$

Modeling

Physical Vapor Transport

Although the number of publications treating the synthesis of ZnO is ample, rather few publications focus on the mass transport model. The principal method of ZnO synthesis is physical vapor transport, hereafter referred to simply as PVT. This method is favored over hydrothermal deposition methods such as sol-gel synthesis because it results in less surface defects, given that there are fewer impurities. Furthermore, PVT is favored because the diffusivities of gases are three orders of magnitude greater than those of liquids, thus favoring the kinetics of crystal growth. In spite of the good crystalline quality of the product, hydrothermal deposition is complicated since it introduces impurities of the solvent into the system. Intrinsic in vapor transport deposition is a study of the mass transfer at the vapor-solid interface. The difficulty of modeling PVT is that the complex interplay of momentum, heat and mass transfer must be considered in full and complemented by a study of the kinetics of crystal growth. Transport phenomena are complicated by the compressibility of the system, which must be accounted for in all equations in the model to obtain a realistic interpretation. The task of modeling PVT is monumental and the computational expense associated with it of equal magnitude. Hence most current models of PVT simplify the problem by making important assumptions.

Modeling Physical Vapor Transport

In realization of the complexity of the problem at hand, a large number of models adopt significant simplifications. These simplifications effectively circumvent many of the difficulties but result in an intrinsically inaccurate model.

In spite of the models' shortcomings, it is useful to review some of the models since they present a physical understanding of the process. In doing so, the simplifications will be identified along with the justifications for making them.

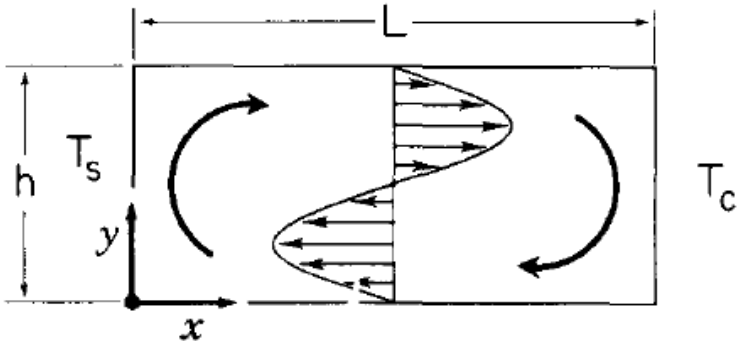

Figure 7: Schematic of recirculation in PVT (Markham, 1981)

A first attempt at modeling vapor transport was conducted by Klosse and Ullersma (KU) giving rise to the classical paper by these two authors. In their work Klosse et al. used numerical simulations to explain the formation of ZnO at different pressure conditions. KU provide an analytical solution to the problem of vapor transport in a horizontal cylindrical ampoule. The very nature of this work entails many important assumptions to allow the system to be solved analytically. For example, KU assumed that the temperature profile was linear, which leads to unrealistic physical properties, namely the vapor has infinite thermal diffusivity, which is reflected in a vanishing Prandtl number. Moreover, a fixed temperature gradient results in a fixed density gradient. Also, KU ignored solutal density gradients, thereby neglecting diffusive transport. A most important simplification was the choice of making the end walls temperature fixed values, which indeed determine the temperature profile artificially. The model was solved assuming a stream function for infinitely long horizontal channel with anti-parallel flow. The velocity profile was obtained from the stream function and the boundary conditions grafted onto it. The limitations introduced by the choice of a particular stream function is that the models is not flexible to account for higher flow velocities, which might lead to the development of boundary layer entrainment. Nevertheless, KU's integral solution allowed them to make predictions about

the enhancement of mass transport due to convection, which is in itself a significant contribution to the understanding of PVT.

Another study conducted by Tena-Zaera et al. used numerical simulation to determine the role of the carrier gas in PVT and the requirements needed to have effective transport at different total pressures. The flow was treated as two dimensional, a linear temperature profile in the axial direction was adopted and compressibility was not included in all equations. Their simulations showed that at equilibrium the interfacial growth can be attained only for certain pressure ranges; however, experiments have shown that in fact growth occurs at pressures outside the theoretical domain, which led the authors to propose that the partial pressures at the interface were actually higher than equilibrium partial pressures. This hypothesis necessitates a mechanism, and the authors provide one. According to Tena-Zaera, the thermal decomposition of ZnO accounts for the higher pressure; moreover, it is postulated that in fact thermal decomposition of ZnO is an activated process catalyzed by additional species that promote additional Zn pressure. The importance of this study relies on their use of the conservation equations to arrive at a comprehensive model to explain crystal growth at the interface. The generated model treated molecular oxygen and zinc vapor as two distinct species transported by a residual gas; oxygen and zinc then combine at the crystal interface to produce ZnO. Theirs is a two dimensional model that when integrated in the radial direction provides a comprehensive flow model. Although extensive, this model relies on a fragile simplification being that, in absence of experimental values for species partial pressures at the interface, they used the equilibrium values. The authors examined crystal growth as a function of different total pressures ranging from 10^{-5} to 10 atm. They found that at low pressures the dominant transport mode is diffusion. At pressures less than 10^{-3} atm, the authors found that flux through the sublimation interface was much less than mass flux through the crystallization interface. They concluded that this observation corresponded to a high diffusion regime, thereby violating mass conservation. To adjust conservation laws they found that it was necessary to reduce diffusion and increase total pressure. In fact, at total pressures greater than 10^{-3} atm mass flux through sublimation is higher than crystallization indicating that diffusion at the interface is very low. Diffusion

occurs when the partial pressure gradient at the interface is significant enough; however, at the crystallization interface the oxygen partial pressure was less than 10^{-6} atm. With respect to the flow, the authors found that it was laminar for all but very high pressures. At a pressure of 1 atm a single convective cell appears. Indeed at this pressure the superposition of buoyancy-driven convection and diffusive advective flow gives rise to a recirculation roll which is displaced toward the growing interface; moreover, the existence of a single convective cell at this pressure in indicative of uniform axial temperature gradient. They found that at pressures of 10 atm the residual gas flow disturbed the mass transport giving rise to little crystal growth. What makes this work comprehensive is that not only does it provide an overview or the mass transport processes that lead to crystal growth, but it also ventures to propose a mechanism that provides an explanation for the experimental observations. Before this study, L'vov et al. had proposed that thermal decomposition of Ag_2O with simultaneous silver condensation into nuclei at the surface of the reactor served as an autocatalytic system for particle growth. In this work it was shown that thermal decomposition is an activated process where the condensation of metals and the formation of metal oxides release the energy necessary to reduce the activation energy of thermal decomposition, such that the partial pressures of silver and oxygen are greater than those at equilibrium. Their findings were extrapolated to the ZnO system leading to the conclusion that zinc can have an autocatalytic role in ZnO decomposition by means of surface reactions. Their postulate is reinforced by the work done by Secco et al., in which the formation of unstable superficial sub-oxides such as Zn_2O and Zn_4O_3 is reported. To my knowledge there is no work that explains this speciation, but it was observed that the film became

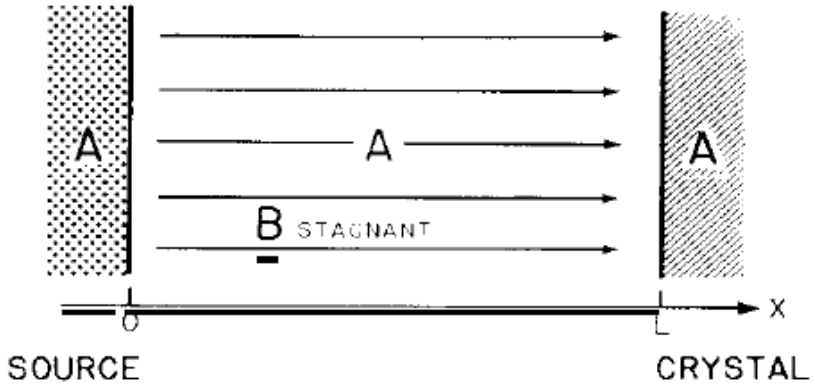

Figure 8: One-dimensional of diffusive PVT of crystal forming component A through inert component B (Greenwell et al., 1981)

grey which might serve as an indication of lower zinc oxide growth. In this work we propose an ab initio-based study of zinc speciation at the experimental thermodynamic conditions to examine the plausibility of lower oxide formation.

An extensive and exhaustive body of work on numerical modeling of physical vapor transport has been accomplished by D.W Greenwell, B.L. Markham and F. Rosenberger. Their volume of work demonstrates the evolution in the model's complexity. In a first paper, they addressed the problem of PVT in a cylindrical ampoule under two conditions. The first concentrated on the problem of the crystal formation of component A through inert component B, with zero net transport of B. In the context of ZnO synthesis this setting would be equivalent to modeling the flow of Zn vapor and oxygen (treated as a single species) in a nitrogen environment. The second case considered was that in which the partial pressure of A and B are equivalent, corresponding to binary diffusion. A third scenario involves the partial pressure of B which is small compared to the pressure of A, a scenario that corresponds to treating B as an impurity. Before this groundbreaking work, the transport in PVT was considered as merely diffusive-advective; furthermore, viscous effects were largely ignored, being lumped into friction factors, laminar flow factors or an overall lumped diffusivity. In previous models the temperature gradient from source to crystal was treated as linear; this assumption led naturally to the existence of a uniform horizontal density gradient, resulting from the thermal expansion of the vapor in free convection mode. Moreover, a constant temperature gradient leads the model to predict very low crystal growth (Greenwell, 1980). In addition, previous models ignored buoyancy and ignored the component of velocity arising from the net mass transport across the enclosure. Greenwell remarks that such assumption would only hold at very high convective flow rates, which is rarely the case in these early models. This first exercise modeled PVT as a one-dimensional problem, but incorporated viscous effects and addressed the problem of a linear temperature profile. Greenberg's team found that the inclusion of viscous terms lead to back-diffusion and recirculation of species B as depicted schematically in Figure 9. In particular, they found that B is practically blown down the tube in the axial center where the mass average velocity is highest. Also they found that component B tends to accumulate at the growing interface and back diffuses along the walls. However, there are little radial concentration gradients.

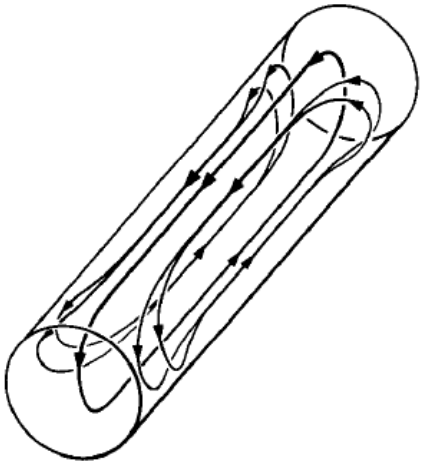

Figure 9: Schematic presentation of overall flow pattern in differentially heated horizontal cylinder (Markham et al 1984)

Most importantly, they found that increasing axial distance leads to a four-fold increase in the characteristic velocity and a decrease in the flow-driving pressure gradient. This work led to acknowledging the importance of accounting for the influence of aspect ratio, i.e., the ratio of length to radius in a cylinder, in the concentration field.

In a second model developed by the same group of Markham, Greenwell and Rosenberger at the University of Utah, a two-dimensional PVT was considered. This model is more comprehensive than the first and includes the effects of gravity on flow, since the previous model identified the existence of free convection. The authors modeled PVT under two conditions: unequal molecular weight of component A (I_2) and B (H_2) and equal molecular weights of A and B. In the first case they found that convective flow arises dominantly from the solute's density gradient; for the second case they found that convective flow arises mainly from thermal expansion. Prior to this work, crystal growth was usually modeled with diffusive transport at the interface and it was assumed that completely mixed convection governed the transport region, but this work would prove otherwise. One of the fundamental characteristics of PVT is that the nutrient density is three orders of magnitude lower than the crystal density. The crystal growth rate is usually associated with diffusive flow velocities normal to the crystal interface. These are not small compared to typical buoyancy-driven convection velocities, which is a key observation in modeling and in understanding the flow mechanisms that lead to crystal growth. Although many modelers choose to neglect the crystallization flow velocity, namely the crystal growth rate, this assumption is only valid at high convective velocities or at low growth rates (Markham, 1980). A fundamental parameter in modeling is the ratio of momentum and mass diffusivity (i.e., the Schmidt number, Sc)[1]. Previous models pose the convective to diffusive mass flux ratio assuming a single convective roll between interfaces. In addition, other models give a value of the Prandtl number as 0.7, indicating that the thermal diffusive rate is larger than the viscous diffusion rate. In view of the limitations of previous models, Markham et al. constructed a model that accounts for the effect of compositional and thermal contributions to convective flow in PVT. In their work they found that radial temperature gradients are due to thermal expansion arising from a variable thermal gradient. They also found that convective flow is axi-symmetric. In agreement with their previous work which included viscous wall-fluid

[1] For a list and description of dimensionless number, refer to Appendix B.

interactions, they attribute the appearance of recirculation to a sensitive dependence on the aspect ratio. Their most important results indicate that buoyancy-driven convective flow and diffusion-induced horizontal density gradients are superimposed on the diffusive-advective fluxes in such a manner that they cannot be ignored; also, they found that only when the whole vapor phase was filled by a convective recirculation roll, is the net transport rate enhanced.

A more sophisticated three dimensional model of PVT is offered by the same group. This work shows that a two dimensional model is inadequate to describe the system. In fact, in Rosenberger's simulations diffusion-advective transport with viscous wall to flow interactions results in recirculation, which is unaccounted for in earlier simplified models by other groups. This recirculation is associated with radial vapor concentration gradients, which is a feature of thermally- and compositionally-driven convection. Rosenberger's work identifies significant faults of previous models. For example, most models assume linear temperature profiles, but such profiles, argues Rosenberger, lead to unwanted crystal nucleation and growth at the cooler part of the vapor transport ampoule. To avoid this feature, his team applied a temperature hump between the source and the crystal and a steep temperature gradient at the growing surface. This temperature profile lowers the supersaturation along the transport path to a value below that of the interfacial value, which drives growth of the main crystal. Furthermore, gradients along the hump lead to more than one convective roll. In particular, Rosenberger's study reveals an important flaw in the two-dimensional models, i.e., transport rates are overestimated, since the model does not account adequately for viscous effects.

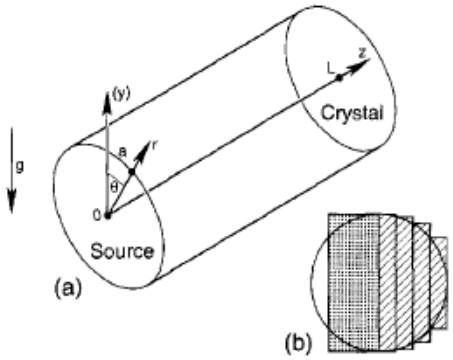

Figure 10: cylindrical ampoule for PVT and mesh configuration (Markham et al., 1984)

Rosenberger's team developed a three dimensional model of crystallization using a cylindrical horizontal ampoule. In this model cylindrical control volumes are employed and

seven boundary conditions are identified to satisfy the momentum, mass, energy and species conservation laws. A fourth-order correlation was used to model the temperature of the side walls of the cylinder, with the ends, corresponding to the source and the crystal, kept at a constant temperature and composition. The flow was analyzed with respect to the temperature and concentration profiles for different pressure regimes and the growth rate was plotted against the Grasshof number at each pressure and temperature value. Their results show that for total pressures, P_T, lower than 8.5 Torr the mode of transport is governed by diffusion as predicted by the 1-D model. However, the authors found that the velocity, concentration and temperature fields reveal a greater degree of complexity. In fact, simulation results suggest the existence of a convective roll that changes direction near both interfaces. However, they found that the velocity field is weak and uniform near the center of the cylinder, i.e., a good distance from the crystal. In the absence of strong interfacial convection, the radial concentration gradient can be readily suppressed by diffusion, which explains the reasonable results of the 1-D model at low pressures.

From their simulations at low pressures the authors found that the convective roll is driven by the compositional density gradient maintained by the source and that the low velocities at the crystal result from the counteractive effects of compositional and thermal gradients at the crystal. In fact, the convective roll disrupts the transport. More specifically, Rosenberger found that it deforms the temperature field to a greater extend than it does the compositional field, which is explained by the lower value of thermal diffusivity as compared to binary diffusivity. Since binary diffusivity, D_{AB}, is inversely proportional to total pressure, at low P_T D_{AB} attains high values, further explaining the diffusion-governed transport at low pressures. The scenario at high pressures, however, is quite different. For P_T greater than 100 Torr the 1-D model greatly underestimates the transport rate, whereas the 3-D model performs well. In this pressure regime, mass transport near the sources is compositionally driven. High mass average velocities develop near the crystal interface as a result of the steep interfacial temperature gradient. Interestingly, convection is very weak halfway between the source and the crystal, and yet diffusion is also limited since D_{AB} attains a much lower value at high total pressures when compared to the low pressure case. Thus, significant mass transport resistance is observed in the path which decreases the transport rate at high pressures to 40% of the middle pressure values. Nevertheless, there is a much more pronounced convective

effect near the crystal interface. Rosenberger's study is illustrative of the complexity of modeling physical vapor transport in connection with crystal growth. However, it also exemplifies the importance of incorporating transport phenomena when considering crystal growth, an approach the present author will pursue in a model of ZnO synthesis by PVT.

Computational Fluid Dynamics

Computational Fluid Dynamics (CFD) is a rapidly growing branch of fluid mechanics. In CFD numerical methods and algorithms are employed in solving and analyzing the equations that characterize fluid flow. Solving the discretized equations involves millions of calculations, since the equations are highly non-linear and describe complex interactions between fluids and surfaces of interests. In spite of the simplifications made in discretization and the speed of supercomputers, often only approximate solutions or qualitative behavior can be obtained from the current codes. Nevertheless, CFD is a vibrant field and codes are being developed that allow for more accurate solutions (CFD, Wikipedia, 2007).

Modeling with CFD

In this work the velocity, temperature and concentration fields will be developed to provide an enhanced understanding of the dynamics that lead to crystal growth via physical vapor transport. Computational fluid dynamics will be used to solve the conservation equations that govern fluid flow.

Computational fluid dynamics, CFD, is the simulation of fluid engineering systems using numerical methods. The use of CFD allows for the generation of a comprehensive model that aids in the analysis of a particular problem that involves fluidic systems. In the case of this paper, the fluid is a vapor mixture of Zn(v)g), and O_2(g); in addition, the case of a third inert gaseous component will also be analyzed. To obtain a flow field, it is necessary to solve the conservation equations in the entire domain of the system. The set of coupled partial differential equations are complex enough that an analytical solution is seldom available, if at all. Instead, a solution is obtained by discretizing the PDEs so that they are reduced to algebraic equations which can be solved in a finite grid, instead of a continuous domain. The variables that need to be solved for are often the velocity field, in the form of mass average

velocity, temperature profile, concentration gradients, density field and pressure field; depending on the number of dimensions of the model, the number of unknowns may vary. Nevertheless, it is often necessary to invoke thermodynamic equations of state for closure since in most cases the number of unknowns exceeds the number of equations. Modeling in CFD compromises a number of steps, e.g.,

1. Formulating the problem
2. Choosing a geometry and a domain for the solution
3. Choosing an appropriate set of an orthonormal coordinate system
4. Postulating the governing equations
    a. Conservation laws
    b. Equations of motion
    c. Thermodynamic principles
5. Determining flow conditions, i.e., the choice of total pressure or temperature of the system, initial concentrations of the reagents, and/or pressure gradient.
6. Selecting an appropriate model
7. Formulating initial and boundary conditions appropriate for the system at hand
8. Establishing a grid and grid spacing for the solution
9. Solving the discretized set of equation using a commercial CFD package

Boundary conditions

Boundary conditions are essential for obtaining a solution of any fluidic system. These arise in the context of temperature and concentration fields as required by the PDE's. There are three types of boundary conditions. The first is known as the Dirichlet boundary conditions, where the value of the variable at hand at one or more of the extremes is explicitly given. Another type of BC is the Neumann type, in which the value of the first derivative of the variable of interest is given. Robin boundary conditions, also known as mixed boundary conditions, are a combination of Neumann and Dirichlet BC. Only when the boundary conditions are well-defined, is a model complete. Moreover, ill-defined boundary conditions will inhibit convergence.

Selection of models

Due to the complexity of the full- blown fluid transport problem, significant simplifications are required. Before attempting to solve the problem at hand, it is necessary to choose a governing model. Xing and Stern (2003)[i] provide a table with the some of the commonly used models and the parameters used to identify them. This table is reproduced below

1. Viscous vs. inviscid (Re)
2. Turbulent vs. laminar (Re, turbulent models)
3. Incompressible vs. compressible (Mach number and equations of state)
4. Single vs. multi phase (Ca, cavitation model, two fluid model)
5. Thermal density effects and energy equation (Pr, y, Gr, Ec, conservation of energy)
6. Free surface flow (Fr) and surface tension (We)
7. Chemical reactions and combustion.

In order to solve the CFD problem, it is first necessary to determine the fluid's properties such as density, viscosity, thermal conductivity, binary diffusivity, etc. These variables are of a thermodynamic nature and as such are functions of temperature and pressure. Many preliminary models ignore this functionality and treat these variables as constants. For some regimes of fluid flow such simplification is adequate; however, if it is rashly made it can lead to significant error in the solution. To avoid the ennui of dealing with units and for ease of interpretation a change of coordinates for the variables is suitable. Most important variables are made dimensionless by appropriate scaling. For example, the distance, or rather position, of a fluid particle in a channel of length L here termed x can be made dimensionless by scaling by total distance L, i.e., x'=x/L $x' = \frac{x}{L}$.

Solution Procedure

The standard procedure for solving transport equations is based on making shell balances in an infinitesimal control volume. The infinitesimal volume is subject to the combined flux of momentum, heat and mass, or a subset of these. For each transported quantity the slab or shell will be perpendicular to the direction of the transport. There are two main modes of transport, bulk fluid or convective transport and transport by molecular mechanisms. The first

can be subdivided into free convection and forced convection. For the second the standard procedures and governing principles are given below as delineated in the classic book "Transport Phenomena" by Bird Stewart and Lightfoot.

Momentum Transfer

A momentum balance over the slab or shell will give rise to a first order differential equation giving the momentum flux distribution. For a viscous fluid, inserting Newton's law of viscosity for the expression for momentum flux will give rise to a first order ordinary differential equation for the fluid velocity as a function of position for a steady state system (if not at steady state an unsteady term for velocity-acceleration- must also be considered). The first order ODE can be solved be either an analytical or numerical scheme and the integration constants can be evaluated using the boundary conditions specifying velocity or momentum flux at the bounding surfaces.

Heat transfer

An analogous solution procedure is followed for solving heat transfer. First an energy balance is made over the thin slab or shell perpendicular to the direction of heat flux giving the heat flux distribution. Substituting Fourier's law of heat conduction for the heat flux gives rise to a first order ODE for temperature as a function of position. This ODE can be solved to give the temperature profile and the integration constants evaluated using boundary conditions that specify T or heat flux at the bounding surfaces.

Mass transfer

The methodology for mass transfer problems is no different. A mass balanced is made over a thin slab or shell perpendicular to the direction of mass flux, leading naturally to a first order ODE for concentration profile. Inserting a relationship between mass flux and concentration gradient such as Fick's Law gives rise to a second order ODE for concentration profile. The integration constants can be evaluated by use of boundary conditions that specify concentration and or mass flux at the bounding surfaces.

Generally the momentum equation is solved first, from which the velocity is obtained to be used in the convective terms of both the energy and mass conservation equations. Most often,

the energy equation follows, since it provides the concentration dependence on temperature; finally the mass conservation equation is solved for giving the concentration profile. Nevertheless, for many problems concentration, temperature and velocity interact dynamically, such that all equations must be solved simultaneously, in which case a computationally expensive iterative scheme with many sub-routines is necessary to solve the problem numerically.

Discretization Methods

The first issue that must be addressed when discretizing a system is to establish the stability of the solution; also to ensure that discretization handles discontinuous solutions elegantly. CFD methods often establish stability numerically, rather than analytically (CFD. Wikipedia, 2007).

The three most prominent discretization methods are:

Finite Volume Method

This method is the preferred method employed by most CFD packages. In FVM the governing equations are solved in a discrete control volume. FVM uses an integral approach, which allows it to preserve the physical meaning of the quantities. The basic equation used in this method is

$$\frac{\partial \iiint Q\,dV + \iint F\,dA}{\partial t} = 0$$

Equation 2

Q= vector of conserved quantity (momentum, energy, mass).
F= flux vector
V= cell volume
A = cell surface area

Finite Element Method

Use of FEM requires special care to ensure a conservative solution (CFD, Wikipedia, 2007). It uses a weighted residual equation, of the form

$$R_i = \int \int \int \left(W_i \, Q \, dV^e \right)$$

Equation 3

R_i= equation residual at an element vertex, i.

Q= conserved equation expressed on an element basis.

W_i= weight factor

V^e= volume element

Finite Difference Method

This is a modern method that uses an embedded boundary for handling complex geometries, thus achieving higher efficiencies and accuracy. Also, it uses overlapping grids in which a solution in interpolated across each grid. The governing equation for FDM is of the form:

$$\frac{\partial Q}{\partial t} + \frac{\partial F_x}{\partial x} + \frac{\partial F_y}{\partial y} + \frac{\partial F_z}{\partial z} = 0$$

Equation 4

Q= vector of conserved quantity

F_i = vector of flux in i-th direction. In Cartesian coordinates i:= x, y or z.

Solution Algorithms

Solving the linear set of linearized equations requires a solver algorithm from the principles of linear algebra. There are two main families of methods, stationary iterative methods and multigrid algorithms. The first comprises a number of techniques, of which the most prominent are symmetric Gauss-Seidel algorithm, successive over relaxation method and Krylean subspace. The main problem with these methods is that information travels slowly from one grid point to another. Multigrid methods solve this difficulty by changing to coarser grids and later interpolating back to the original fine grid.

Method

Acknowledging the intrinsic complexity of modeling PVT, the approach the present work was to part from a physically simple system and progress toward higher levels of complexity.

Inherent in all models, regardless of their degree of complexity, is the need to determine thermophysical parameters and transfer properties that are realistic for the choice of operating conditions. For this work the parameters of interest are:

Thermophysical parameters

1. The average density of the bulk gas at the steady state operating temperature and pressure.
2. The heat capacity of the bulk gas mixture at the operating temperature assuming that the value is independent of pressure.
3. Equilibrium partial pressures at interfaces, and the corresponding mass fractions.
4. Local vapor densities in the vicinity of the source and crystal interfaces.

Transfer Properties

1. The dynamic viscosity of the bulk fluid.
2. The thermal conductivity of the bulk fluid.
3. Binary diffusivities for the two species in the carrier gas.

Manipulated Variables

1. Total pressure[2].
2. Source and crystal temperatures.
3. Wall temperature profiles.
4. Dimensions and geometry of the system.

It should be noted that the wall temperature profiles are actually a result of solving the energy equation; however, it is here listed as a manipulated variable following the work of many groups that impose a known profile to the walls to simplify the system.

[2] Rosenberg et al. determine the total pressure based on mass conservation and using the ideal gas law to determine the number of moles in the bulk fluid at the time when the ampoule was filled.

In this work, the total pressure will be arbitrarily determined at a value of ranging from .01 to 1 atm, which ensures the validity of the one dimensional model (Rosenberger et al, 1997). Other groups, however, have derived the total pressure by using mass conservation and using the ideal gas law to determine the number of moles in the system at the system fill pressure and temperature (Rosenberger, 1997). In addition all models will be either one or two dimensional. In spite of the studies that indicate that 3-D models provide a more accurate understanding of PVT, the computational expense of three dimensional models (Rosenberger, 1997) is beyond the scope of this work.

One of the objectives of this work is to familiarize the author with one of the partial differential equations modeling environments available and to evaluate its effectiveness as dictate by the accuracy of the results and the relative ease of use. The software of choice was COMSOL Multiphysics, whose graphical modeling environment and, in particular, its chemical engineering module which targets transport phenomena in its many expressions, provides a comfortable base upon which to build complex systems. Before attempting to model the complex PVT system, we gained some practice using the software by developing simpler standard phenomena fully. The models were constructed using the parameters that describe these systems and they were fully analyzed in order to gain vision about how to interpret the results of the PVT system that were then modeled. Moreover, by modeling standard systems with well-established parameters we avoid the added uncertainty of whether the value of the parameters inhibits convergence of the solution.

The scheme by which the level of complexity increases gradually is two-fold: to familiarize the author with the operational details of the software application and its many features, and to gage the difficulty of solving the system of equations as the degree of complexity increases. A first model targeted the interactions of diffusion and convection in two component flows, which is an important variable in modeling PVT. A second set of models targeted multi-component flow in diffusive transport mode. This mode of transport is particularly relevant for low pressure reactors in which mass transfer resistance is often the limiting step in the reaction kinetics. Moreover, understanding multi-component interactions is of crucial importance for modeling PVT. A third model targets non-isothermal flow and its effects on reaction kinetics; the addition of the energy equation to the system results in a whole new level of complexity; however, the effects of temperature gradients on density and

concentration cannot be neglected when modeling PVT. Ultimately, it is desired to attain a two-dimensional model similar to that postulated by Tena-Zaera et al and Ramachandran et al.

Numerical Analysis

The scheme for solving the model at each step follows the methodological approach common to fluid dynamicists:

1. Characterize the system according to the governing physical principles.
2. Identify what results are desired from the simulations
3. Identify the unknowns.
4. List the complete form of the transport equations and, if necessary to provide closure, the appropriate equation of state.
5. Make assumptions to simplify the system whenever appropriate.
6. Modify the system of equations to comply with the simplified system.
7. Identify boundary and initial conditions according the degree of the differential equations (e.g. if a first order ODE in x state one boundary condition).
8. If appropriate, make a change of coordinates to dimensionless coordinates for the system of equations and boundary conditions.
9. Solve the system of equations in non-dimensional form.
10. Revert to original coordinates.

Procedure for Solving in CFD

Modeling in CFD compromises a number of steps.

1. Formulating the problem
2. Defining a geometry and a domain for the solution
3. Choosing an appropriate set of an orthonormal coordinate system.
4. Postulating the governing equations.
    a. Conservation laws
    b. Equations of motion
    c. Thermodynamic principles. E.g. chemical equilibrium.
5. Determining flow conditions

    a. E.g. choice of total pressure or temperature of the system, initial concentrations of the reagents, pressure gradient.
6. Selecting an appropriate model.
7. Formulating initial and boundary conditions appropriate for the system at hand.
8. Establishing a grid and grid spacing for the solution.
9. Choosing an appropriate solver methodology to handle the intricacies of the mathematical system.

Experimental

Experimental Set Up at Chulalongkorn University

ZnO synthesis at Chulalongkorn University, CU, is achieved via two methods: physical vapor transport and sol-gel synthesis. This work is concerned uniquely with PVT, however. The synthesis process is achieved in a non-isothermal quartz reactor. The dimensions of the reactor are given in Figure 11. Figure 11 is drawn to scale.

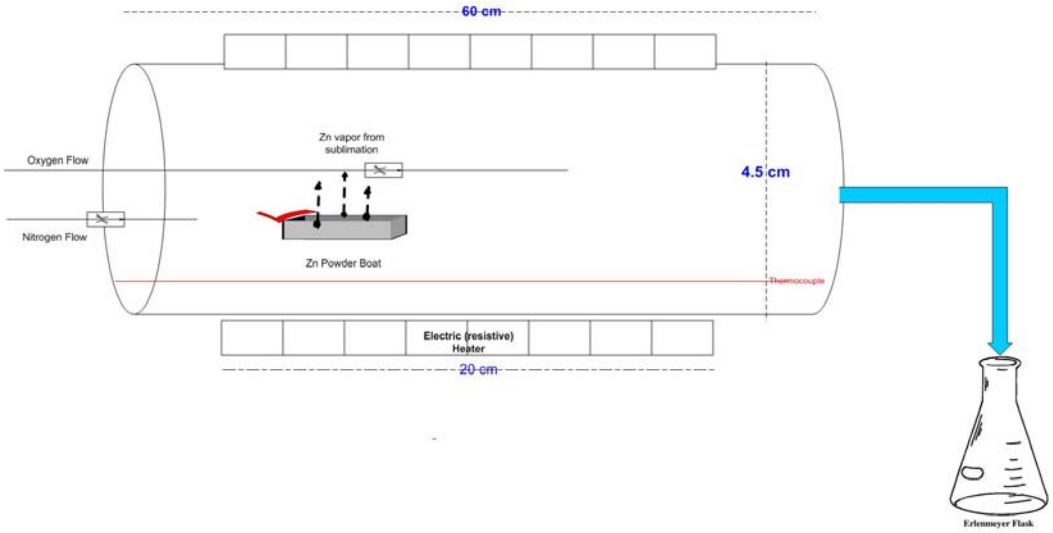

Figure 11: experimental setup for ZnO synthesis by PVT at Chulalongkorn University

In a usual experiment using the setup depicted by Figure 11 1.5 grams of Zn dust less than 10 μm in diameter (Sigma Aldrich 98 %+) are deposited on the boat reactor. The reactor chamber is allowed to rise to 700 °C from an initial temperature of 50 °C with a temperature ramp of 10 °C/min. At 700 °C Zn powder is expected to sublimate from the solid form to Zn vapor. The boat reactor is placed inside the tubular quartz reactor 8 cm along the entrance. Nitrogen gas is pumped at a flow rate of 1000 ml/min and is allowed to disperse in the reactor chamber until a total pressure of 1 atm is achieved. Oxygen gas is then injected downstream of the boat reactor at a variable flow rate of 20-40 ml/min. In this work, however, an oxygen flow rate of 20 ml/min was considered for all models. Oxygen concentration gradients resulting from the position of oxygen gas injection lead to back diffusion; this phenomenon, however, was neglected in all computations. Zn vapor and oxygen gas are

transported in the carrier gas where Zn is oxidized to form ZnO. Ideally ZnO will deposit only downstream of the reactor tube; however, it has been found experimentally that Zn does not deposit preferentially downstream, but rather ZnO is observed along the reactor walls. Although the reactor's dimensions in the axial direction give an effective length of 60 cm, the effective length is significantly less. In order to determine such a length approximately the temperature profile of the reactor in the axial direction was measured and plotted. The steepest decline in temperature between any two points was attributed to crystallization, and the distance of such point from the entrance was taken as the reactor's effective length. This length is of 32 cm. Figure 12 illustrates the experimental temperature profile from which the effective length was extracted; while Figure 13 provides an engineering schematic of the system design.

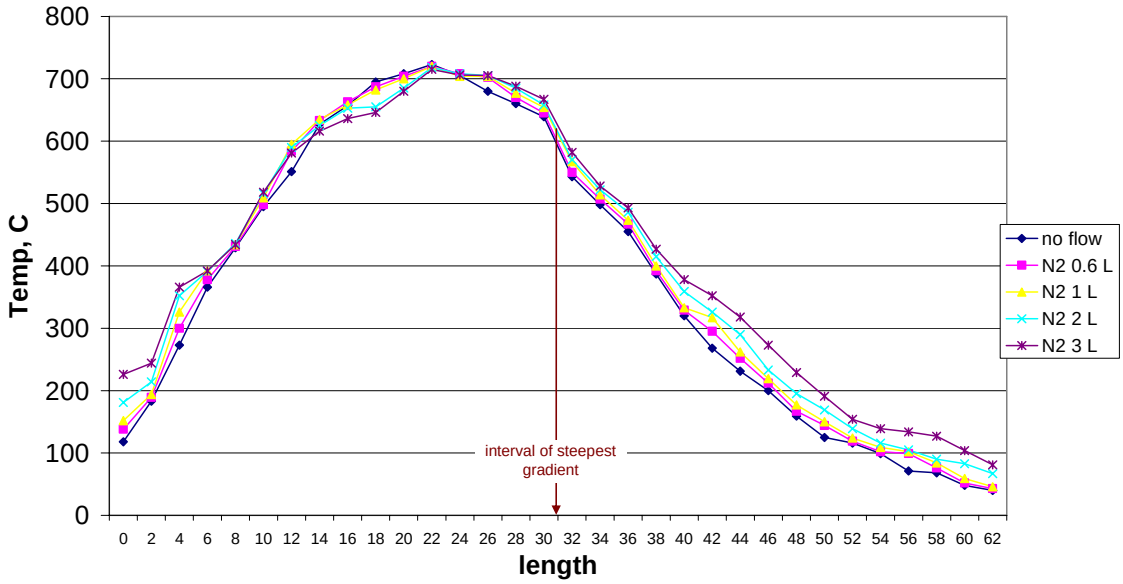

Figure 12: quartz reactor temperature profile (Tee, 2007)

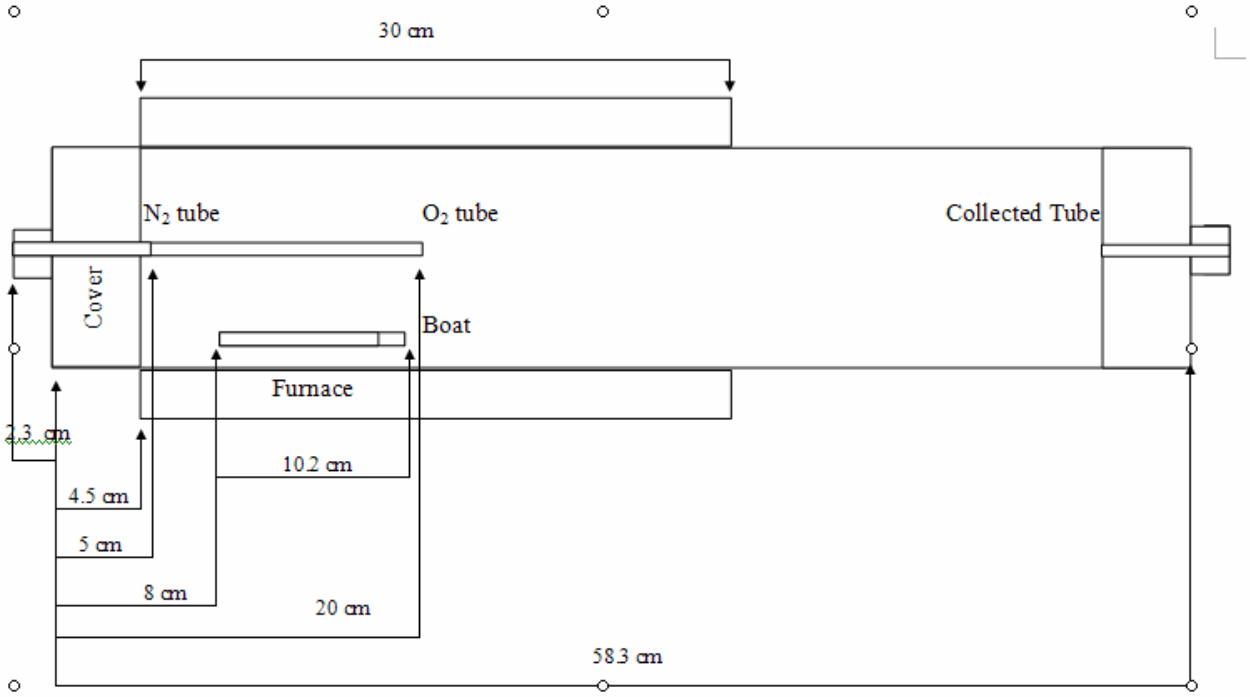

Figure 13: schematic and dimensions of cylindrical quartz reactor for ZnO synthesis at Chulalongkorn University (Tee, 2007)

At the moment, there is no pressure gauge to obtain a total pressure reading, however, since the reactor discharges to atmospheric pressure in the collector flask, ambient pressure is assumed throughout the reactor.

Model 1: Convection and Diffusion of O_2 in N_2

One of the principle issues of debate among scholars of PVT is whether the flow is purely advective-diffusive or if viscous interactions with the wall lead to recirculation of the inert carrier gas and thus possibly back-transport of the solute carried by bulk flow. These set of models, in addition to the multicomponent models, can help finalize this discussion, at least as it applies to the experimental conditions.

The systems modeled in this first set comprise isothermal, incompressible systems in a simple Cartesian geometry. A reaction term was not included explicitly. The flow is inherently a multiphase flow due to the two components that make it up; however, since the solute is very dilute, transport properties are taken as those of the carrier gas, and thus

effectively the flow is treated as a monophase flow. The model is geometrically two-dimensional, but effectively one-dimensional in profile since velocity has only an axial component.

Leaching of a solute in laminar flow

Two models were developed to analyze the effect of convection and diffusion. The first of these two models considers the relative force of convection and diffusion in a setting where the solute concentration varies due both to convection and to diffusion at the lower boundary. It is desired to understand whether diffusion or convection has a greater effect in the concentration gradient.

The physical situation corresponds to one diffusing species dissolved in water at room temperature. The geometry is a simple Cartesian rectangle of dimension 6 mm x 20 mm. The physical characteristics can be seen in the figure below and correspond to the following: the fluid inlet is at the leftmost vertical boundary and the solute enters this boundary by convection; the plate at which leaching takes place is the lower horizontal boundary. The upper horizontal boundary is a symmetry boundary and at the rightmost vertical boundary the solute leaves the system primarily by convection. The objective of this exercise is to evaluate the Schmidt number for the system, that is, the ratio between

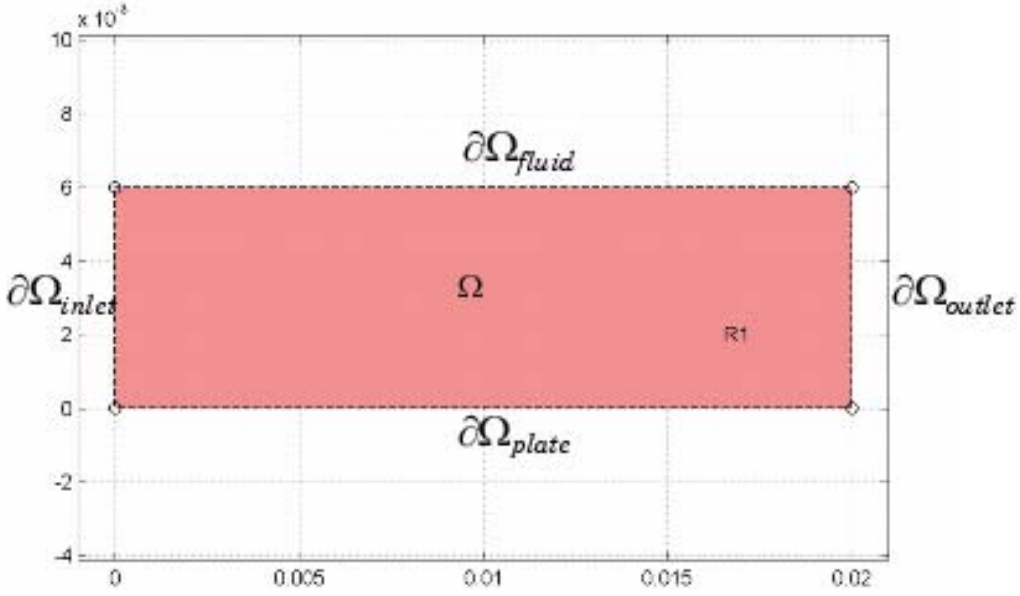

Figure 14: geometry and subdomain for leaching model

the viscous and the diffusion boundary layers. The simplified geometry and subdomains for this firs model are illustrated in Figure 14.

COMSOL's Chemical Engineering module was used. Specifically, the momentum balance and mass balance modes were employed. The momentum balance was accounted for by the Navier-Stokes equations for incompressible flow; the mass balance was completed assuming the coexistence of convective and diffusive transport. The equations are coupled by the velocity term.

Assumptions

1. Mass transfer occurs through diffusion and convection.
2. Production of diffusing species does not influence the viscosity or density of the fluid.
3. Symmetry is assumed along the boundary toward the free fluid.
4. Laminar flow is fully developed at outlet.
5. The solute concentration at the inlet is known.
6. The solute concentration in the symmetry boundary is known.
7. The production rate of the diffusing species (the rate of mass transfer by leaching) is known.
8. The dominating transport process is in the direction of the flow.
9. The dominating transport process at the outlet is convection.

Vapor transport in diffusion and convection

Model Definition

This model considers the mono-phase transport of a gaseous solute in an inert solvent. Such a simplified physical model is useful for understanding the distribution of oxygen gas in the reactor and evaluating the relative force of diffusive and convective transport. In accordance to the hypothesis presented by Park et al., the oxygen distribution will aid

in understanding why ZnO precipitates throughout the reactor chamber. The solute in this model is oxygen gas and nitrogen gas is the corresponding solvent. The numerical model was set up in a two-dimensional cylindrical geometry. Radial symmetry was used to construct an axi-symmetrical model. Oxygen transport was achieved via two principal transport mechanisms: convection and diffusion. The specific geometry corresponds to a boat reactor for physical vapor transport, as used in the synthesis of high purity Silicon in the microprocessor industry. The choice of such geometry was dictated by the physical relevance and similarity to the system of interest. Furthermore, this geometry is engrained in a functional model of COMSOL Multiphysics. Figure 15 depicts the simplified geometrical settings and the subdomains for the solution.

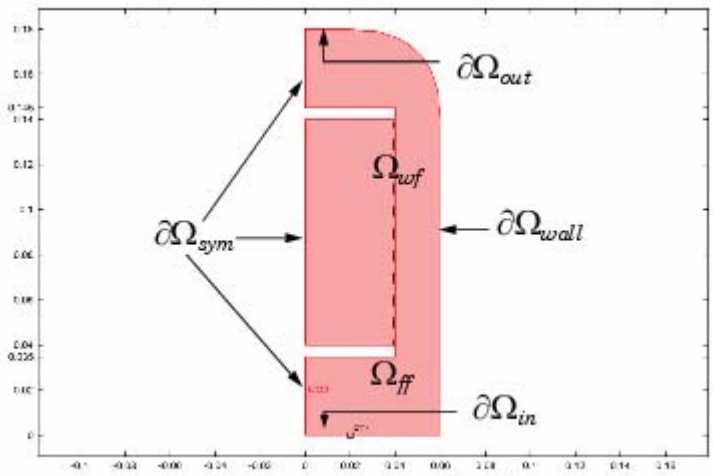

Figure 15: schematic depicting the model geometry and the subdomains

The model is based upon a steady state, isothermal environment. The physical situation corresponds to oxygen gas transported in nitrogen at a concentration of 20 ml of oxygen per 1000 ml of nitrogen. The fluid inlet at the lower boundary is assumed to be fully mixed and the superficial velocity is assumed uniform across the cross-section at z=0. This model is so proposed to simulate the convective flow of the bulk gas through the quartz reactor and the diffusive flux in the radial direction that leads to crystallization.

Although the experimental set-up at Chulalongkorn University does not include a heterogeneous catalyst, a subdomain representing a heterogeneous catalyst was included

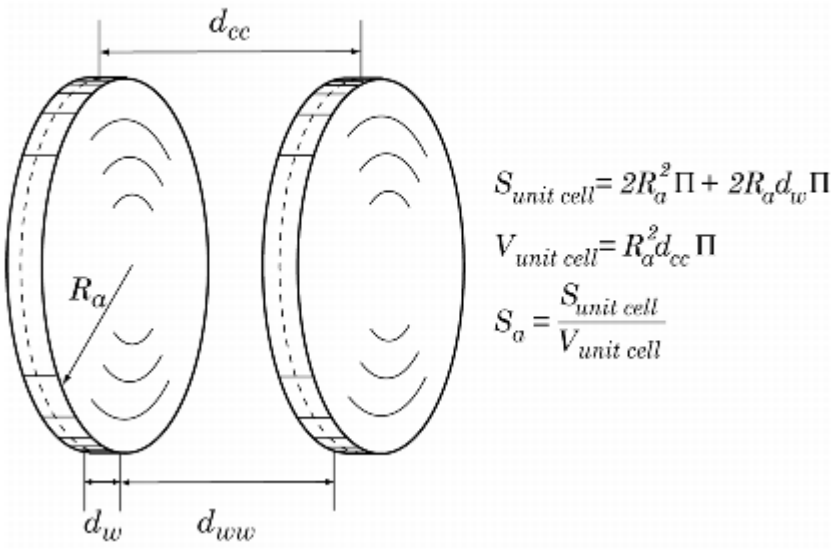

Figure 16: depiction of the catalyst bundle disks

in the model. Such addition was validated by the work of other groups that use Indium or Nickel catalysts in the synthesis of ZnO. Reaction is assumed to take place in the subdomain corresponding to the heterogeneous catalyst. The effective catalyst area is maximized by implementing consecutive identical catalyst disks as illustrate in Figure 16.

The variables of interest (unknowns) are

1. Velocity profile
2. Species partial pressure profile (concentration) for each solute species.

For this isothermal system, the temperature is assumed uniform at a value corresponding to the arithmetic mean of the source and crystal temperatures at Chulalongkorn University and hence the temperature profile needs not be solved for.

Equations

The governing equations are continuity, the equations of motion in two dimensions and the specie conservation equation.

$$r\left(\frac{\partial u}{\partial x}+\frac{\partial v}{\partial r}\right)+v=0$$

Equation 5

$$\frac{\partial}{\partial x}\left(-\eta r\frac{\partial u}{\partial x}\right)+\frac{\partial}{\partial r}\left(-\eta r\frac{\partial u}{\partial r}\right)+\rho r u\frac{\partial u}{\partial x}+\rho r v\frac{\partial u}{\partial r}+\frac{\partial p}{\partial x}=0$$
$$\frac{\partial}{\partial x}\left(-\eta r\frac{\partial v}{\partial x}\right)+\frac{\partial}{\partial r}\left(-\eta r\frac{\partial v}{\partial r}\right)+\frac{\eta}{r}v+\rho r u\frac{\partial v}{\partial x}+\rho r v\frac{\partial v}{\partial r}+\frac{\partial p}{\partial r}=0$$

Equation 6

$$\vec{\nabla}\left(\rho\hat{H}\vec{v}\right)+\vec{\nabla}\vec{q}+p\left(\vec{\nabla}\vec{v}\right)+\vec{\nabla}\left(\hat{H}\vec{J}_i\right)+\overleftrightarrow{\tau}:\cdot\vec{\nabla}\vec{v}=S_h$$

Equation 7

$$\vec{\nabla}\left(\rho\,\vec{v}\,C_i\right)=\vec{\nabla}\vec{J}_i$$

Equation 8

The continuity equation is immediately satisfied by assuming the fluid to be incompressible. For the isothermal system, the energy equation is unnecessary and is thus dropped.

The computational package COMSOL Multiphysics ® was used in developing the numerical model. In particular, the convection and diffusion application mode was employed. In this mode the complete equation for convection and diffusion is applied:

$$\frac{\partial c_i}{\partial t}+\vec{\nabla}\cdot\left(-D_i\nabla c_i+c_i\vec{u}\right)=R_i$$

Equation 9

In Equation 9 the term in parenthesis represents the complete flux N_i. For the simulation, however, the diffusion and convection terms were decoupled so that the divergence operator operates only on the diffusion term, thereby implying that the system is only slightly compressible; this modification allows for enhanced numerical stability, as it allows us to decouple the momentum and mass balance equations; in addition, the time dependent term was dropped. With these simplifications the mass balance in the domain is reduced to

$$\vec{\nabla}\cdot\left(-D\nabla c + c\,\vec{u}\right) = 0$$

Equation 10

Moreover, the steady state, incompressible Navier-Stokes equation becomes

$$c_i\,\vec{u} + \vec{\nabla}\cdot\left(-D_i\nabla c_i\right) = R_i$$

Equation 11

Parameters of the system

The numerical simulations require us to determine certain parameters that define the system at the operating conditions.

The dimensions of the system were adopted from the experimental set up at Chulalongkorn University, but the geometrical details correspond to a boat reactor for silicon synthesis. The length and diameter dimensions from Chulalongkorn were, however, preserved. The temperature of the source and crystal were also were used in defining an average temperature

$$T_{avg} = \frac{T_s + T_c}{2}$$

Equation 12

The system operating pressure is chosen as 1.01325 x 10^4 Pa corresponding to one of the experimental runs by Tena-Zaera. This parameter is allowed to vary and its effect on the system evaluated.

Kinetic Parameters

Once the total pressure is established the density of the bulk fluid is computed from a weighted average of the species density assuming the applicability of the ideal gas law.

$$\rho = \frac{p\,M_N}{RT\left[1 + \sum_{i=1}^{n-1}\left(\frac{M_N}{M_i} - 1\right)c_i\right]}$$

Equation 13

Local partial pressures for O_2 at the source, in this model the inlet to the reactor, and crystal interfaces (the outlet) with the vapor are computed assuming equilibrium partial pressures following congruent sublimation and crystallization at each respective surface. This assumption allows us to compute the O_2 partial pressures from the equilibrium constant for the reaction at the corresponding temperatures. It is widely accepted that ZnO synthesis occurs via molecular oxygen and hence follows:

$$Zn\,(v) + O_2\,(g) \leftrightarrow ZnO\,(s)$$

Equation 14

The equilibrium constant for the reaction is given by

$$K_{eq} = \exp\left(-\frac{\Delta G}{RT}\right)$$

Equation 15

Since $K_{eq} = \frac{1}{P_{O_2} P_{Zn}}$ and it is assumed that $P_{Zn} = 2P_{O2}$ then the equilibrium partial pressure for each specie at the crystallization interface can be readily calculated.

The kinetic rate constant for the reaction is obtained by manipulating the data of Tena-Zaera at a pressure of 1.01325 x 10^4 Pa. In this work the reaction rate is given in terms of kg of ZnO per second. Mass action kinetics were assumed for the reaction and the equilibrium condition $P_{O2} = P_{Zn}$ was employed to obtain a reaction rate constant for the reaction, k_1. The reaction rate was then expressed as

$$R = -k_1 C_{O_2}^2$$

Equation 16

Indeed, the reaction is postulated as being second order in oxygen concentration.

For the first model comprising nitrogen and oxygen only, kinetic parameters are readily available for a range of temperatures; these values were used for the computations. However, in the absence of such data, these parameters can be easily computed using the Chapman Enskog theory for low density gas mixtures. The expression for a gas at low density from the Chapman-Enskog theory for is:

$$\mu = 2.6693 \times 10^{-26} \times \left[\frac{(MT)^{\frac{1}{2}}}{\sigma^2 \times \Omega_\mu} \right]$$

Equation 17

The parameters for Equation 17 are given in Table 1. The temperature, T, in all the parameters derived from the kinetic theory of gases is taken as the average temperature in the reaction chamber.

Similarly the thermal conductivity was computed based on the kinetic theory of gases:

$$k = \left(\frac{25}{32} \right) \frac{\sqrt{\pi m \kappa T}}{\pi \sigma^2 \Omega_k} \hat{C}_v$$

Equation 18

The binary diffusivity for oxygen in nitrogen has been tabulated amply and the tabulated value will be used in the model. When the value cannot be found directly, the kinetic theory of gases provides a formulation

$$D_{AB} = \left(\frac{3}{16} \right) \sqrt{2 \frac{(RT)^3}{\pi} \left(\frac{1}{M_A} + \frac{1}{M_B} \right)} \frac{1}{\widetilde{N}\, p \sigma^2 \Omega_{D_{AB}}}$$

Equation 19

In Equation 19 $\widetilde{N}$ represent Avogadro's Number.

Table 1 provides a comprehensive list of the kinetic parameters employed in the model as defined in COMSOL.

Table 1: kinetic constant values for use in COMSOL

constants in CVD model		
symbol	**OTALVARO-1**	**interpretation**
dcc	N/A	I don't know
Dn	1.81E-05	binary diffusivity
dw		disk thickness
k1	1.35E+03	reaction rate constant
mu	4.30E-05	dynamic viscosity
Mn2	2.80E-02	Molecular weight carrier gas, nitrogen
MO2	3.20E-02	Molecular weight of reacting gas
Pt	10132.5	total pressure
Ra	0.0225	radius of catalyst disk
Rg	8.314	universal gas constant
Te	916.65	average temperature
vo	1.07E-02	inlet velocity
co	0.026590901	inlet concentration
D	1.81E-04	corrected diffusivity
Deff		effective diffusivity
ro	3.73E-02	gas density
ros		
Re	2.09E-01	Reynolds number
Sa	3.125	specific area m2/m3

Subdomain settings and boundary Conditions

For this model two distinct subdomains were specified. The first corresponds to the free fluid subdomain, where transport occurs via pressure induced convection. The second subdomain corresponds to the heterogeneous catalyst bundle. In this subdomain transport is dominated by diffusion. Accordingly, the kinetic parameters should be defined for each subdomain. For the free fluid subdomain, the diffusivity used corresponds to the binary diffusivity of oxygen in nitrogen at STP corrected for pressure. The velocity components u and v were allowed to vary; the transport properties density and viscosity were defined in this domain as detailed in the methodology section. For the bundle subdomain the convective contribution to transport was neglected. Consequently, only the anisotropic diffusion coefficient was defined; moreover, the velocity components were set to zero.

Boundary Conditions

At each bounding surface the following need to be specified:

1. Velocities or shear stresses to satisfy the momentum equation.
2. Concentration or specie fluxes to completely define the species equation.

The boundary conditions are obtained by assuming uniform superficial velocity at the inlet and an isotropic diffusion coefficient at the outlet. Furthermore, the model assumes that laminar flow is fully developed at the outlet so that all velocity components are normal to the surface. Coupling reaction and transport in the bulk fluid inherently brings stiffness to the system and often results in the solution not converging. To avoid such complication, reaction terms can be introduced as special boundary conditions. This approach has been adopted in the current model. Special care was placed in defining these boundary conditions to ensure that the mass balance in the system is respected. In particular, crystallization at the catalyst subdomain must be matched in such a ways as to ensure that steady state prevails. An ingenious methodology was presented in the work by Tena-Zaera and also the work of Ramachandran et al. The present model will adopt such methodology.

The reaction term can be mimicked by introducing it as a flux perpendicular to the interface where reaction occurs. The complete specie flux comprises both diffusive and convective transport. The reaction term can be embedded in the diffusive term by carefully specifying the diffusion coefficient in the radial direction. For this model, an anisotropic effective diffusivity was defined which includes the reaction term. The complete settings for the diffusion subdomain are given in Table 2.

Table 2: diffusion subdomain settings

Diffusion subdomain settings		
symbol	**expression**	**description**
D	1 0 0 1	Anisotropic diffusion coefficient (m2/s)
R	(-k1*Sa)*c^2	reaction rate constant kg/mol-m3
u	0	radial velocity
v	0	axial velocity

The complete specie flux is given by Equation 20 and Equation 21 at the interface is

$$J_{O_2} = \rho u C_{O_2} - \rho D_{O_2} \nabla_{axial} C_{O_2}$$

Equation 20

$$J_{N_2} = \rho u C_{N_2} - \rho D_{N_2} \nabla_{axial} C_{N_2} = 0$$

Equation 21

Equation 20 expresses that the flux of oxygen at the interface with the catalyst is finite, while Equation 21 defines the impermeability of the interface to N_2 flux, effectively the inertness of this gas.

The boundaries and subdomains for the model are given in Figure 17 as used in COMSOL.

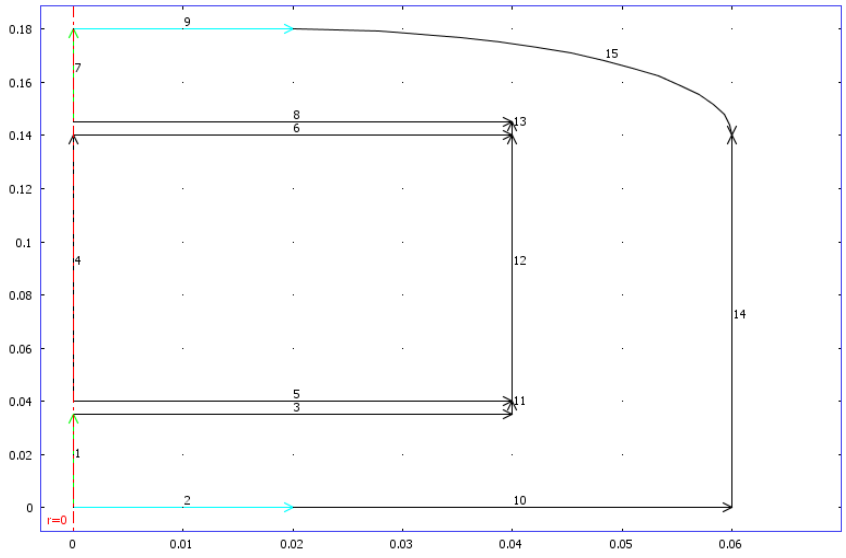

Figure 17: boundary setting definitions

r=0 corresponds to the axis of symmetry for the cylindrical domain. At this boundary the velocity and concentration are given by symmetry. At the wall no-slip is applied; this boundary is an impermeable boundary to both species. Slip is applied to the flow at the

crystal interface; at this boundary diffusion dominates and diffusive flux is specified as a function of local oxygen concentration. At the inlet to the reactor the velocity is assumed uniform at a value of vo and the oxygen concentration is known at a value of co. The outlet is pressure dominated, where the outlet pressure is set to zero; also, at this boundary convective flux dominates.

A non-uniform mesh was constructed for the domain of the solution. The mesh was refined at the interface boundary and the outlet boundary to give more detailed information about the flow behavior at these relevant boundaries. In addition, after acknowledging the stiffness of the system, a consequence of coupling momentum with reaction, a nonlinear parametric solver was chosen. The parameter for the solver was the inlet velocity, vo. The UMFAC method was chosen for the solution. A schematic of the mesh is given in Figure 18.

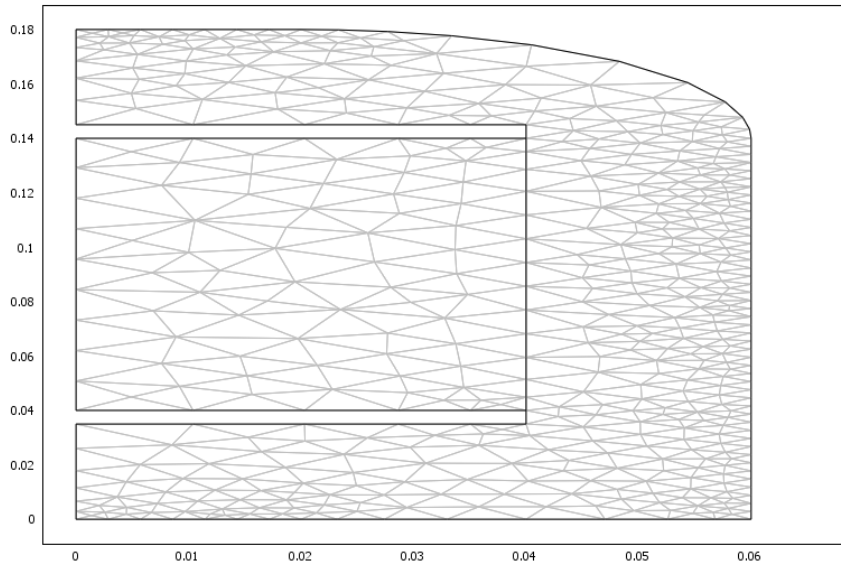

Figure 18: Mesh configuration in the solution domain

Model 2: 2-D multi-component diffusive flux

In order to model the three component diffusive transport of Zn, O_2 and N_2 in a cylindrical ampoule, which is the conventional system on which ZnO synthesis takes place, we proposed modeling the flow as Maxwell-Stefan flow. In this work we will model two distinct systems in Maxwell-Stefan diffusion mode. The two systems differ in geometry and in the manner by which reaction is accounted for. The particular geometry of the first system is taken from transport in a Proton Exchange Membrane, which is an example case in COMSOL. The second geometry corresponds to the simplified geometrical setting for PVT modeling.

Model Definition

Both models in this mode depict a system in which two reactive gases, Zn and O_2 diffuse in an inert carrier gas. The composition of the reactant gases in the container is affected by a reaction term, which is stoicheometrically determined. A single reactive boundary acts on the system, which corresponds to a growing crystal in ZnO synthesis by PVT. The system is isothermal and compressibility effects are neglected throughout.

In Maxwell-Stefan mode diffusive transport dominates; moreover, the diffusivities are postulated as being compositionally dependent. To account realistically for the three component mixture, the diffusivities in this model account for solute-solvent and solute-solute interactions. The species conservation equation is then given by Equation 22

$$\frac{\partial \rho \omega_i}{\partial t} + \nabla \cdot \left(\rho \omega_i \mathbf{u} - \rho \omega_i \sum_{j=1}^{n} \tilde{D}_{ij} \left(\nabla x_j + (x_j - \omega_j) \frac{\nabla p}{p} \right) - D_i^T \frac{\nabla T}{T} \right) = R_i$$

Equation 22: species conservation equation in Maxwell-Stefan flow mode

In Equation 22 D_{ij} represents the binary diffusivity tensor; ω_i is the species mass fraction, x the mole fraction and R_i the reaction term. In a closed cylindrical ampoule in isothermal flow

and with the reactants very diluted in the solvent convection is negligible. This assumption is validated since the pressure driving force for convection would be a function of the density changes in the cylinder, which would only be significant if the reactants were not sufficiently diluted. For the current model, a conservative form of Equation 22 was employed, which allowed us to apply the divergence operator only on the diffusive term, allowing for more numerical stability, as no sub-routine was necessary in order to satisfy continuity on each iteration.

Binary diffusion coefficients were computed from the Fuller, Schnetter & Gillings expression based on diffusive volumes of each species. This expression was chosen over the Chapman-Enskog equation since the parameters for zinc for the Fuller Schnetter & Gillings expression were readily tabulated in the literature. The expression for the binary diffusivities is given by Equation 23

$$\hat{D}_{ij} = k\frac{T^{1.75}}{p(v_i^{1/3} + v_j^{1/3})^2}\left[\frac{1}{M_i} + \frac{1}{M_j}\right]^{1/2}$$

Equation 23

The diffusion volumes for each species were taken from tabulated data and are shown in Table 3

Table 3: Diffusion Volumes

Species	Diffusion Volume (m^3/mol)
O_2	16.6 e -6
Zn	9.16e-6
N_2	17.9e-6

For the three component mixture, only three binary diffusivity values are necessary, since the diffusivities are symmetric. Hence the diffusivity tensor is defined by the upper triangular matrix

$$\begin{bmatrix} DO_2\,Zn & DO_2\,N_2 \\ 0 & DZn\,N_2 \end{bmatrix}$$

Equation 24: Diffusivity Tensor for Maxwell-Stefan flow

The dependent variables for the system were the mass fractions of each of the components. Note that the diffusivities are strong functions of the local concentration, adding an important non-linearity to the system of equations. To account for the reaction term the density was also allowed to be compositionally dependent. The molar mass of the system is a function of the dependent variables, being defined as

$$M = \sum_{i=1}^{3} M_i w_i$$

Equation 25

Consequently, the density is a dependent variable defined as

$$\rho = \frac{MP_T}{RT}$$

Equation 26

The constant for the system are listed in Table 4.

Table 4: constant for Maxwell-Stefan flow model

constant	Expression	description
Length, L (m)	9.00E-02	ampoule length
Diameter, D (m)	1.50E-02	ampoule height
k	3.16E-08	Boltzmann constant
vN2 (m3/mol)	1.79E-05	nitrogen diffusive volume
vO2 (m3/mol)	1.66E-05	oxygen diffusive volume
vZn (m3/mol)	9.16E-06	Zinc diffusive volume
MO2 (kg/mol)	3.20E-02	oxygen molecular mass
MZn (kg/mol)	3.00E-02	Zinc molecular mass
MN2 (kg/mol)	2.80E-02	nitrogen molecular mass
wO2_0	3.01E-04	oxygen mass fraction at inlet
wZn_0	5.62E-04	Zinc mass fraction at inlet
T0 (K)	1258.15	reactor average temperature
p0 (Pa)	1.01E+05	reactor total pressure
rho0	9.69	density from ideal gas law
R (m3-Pa/K-mol)	8.314	universal gas constant
DO2_N2 (m2/s)	2.54E-04	oxygen diffusivity in nitrogen
DZn_N2 (m2/s)	1.36E-04	Zinc diffusivity in nitrogen
DO2_Zn (m2/s)	1.38E-04	oxygen diffusivity in Zinc
R_O2 (kg/m2-s)	4.59E-07	oxygen reactive flux at crystal interface

R_Zn (kg/m2-s)	8.60E-07	Zinc reactive flux at crystal interface

The geometry chosen was a two dimensional rectangle, the dimensions of which were guided by the work of Tena-Zaera et al. Boundary conditions were also dictated by the work of the former authors. Figure 19 provides a schematic representation of the geometry and boundary settings employed.

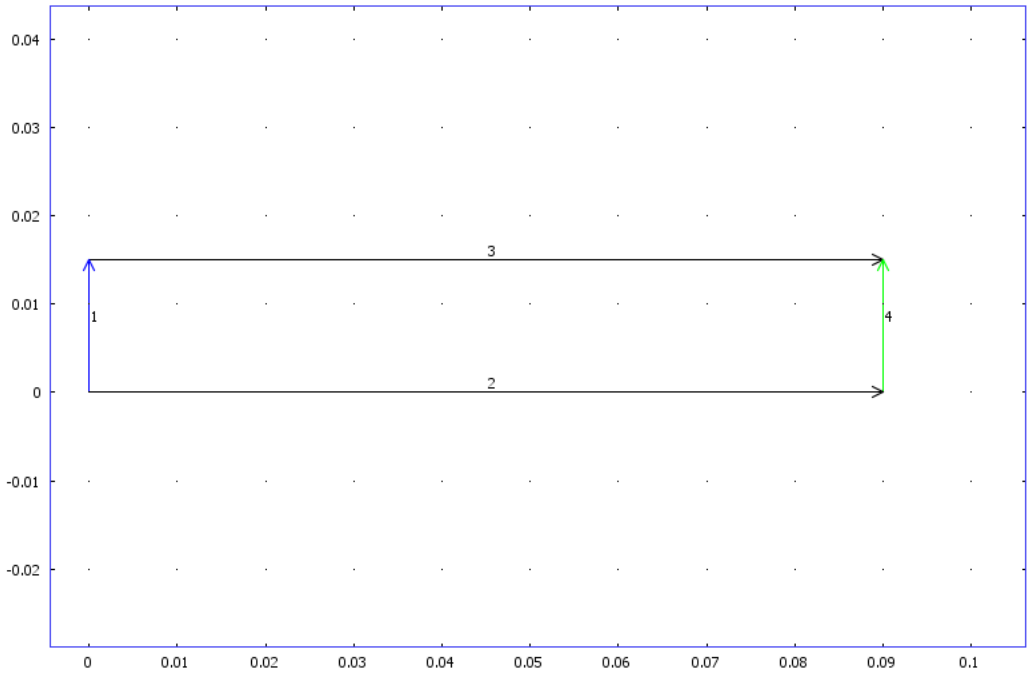

Figure 19: geometry and boundary settings for Maxwell-Stefan Flow Model

Similarly the geometry and boundary setting for the second Maxwell Stefan Flow model are given in Figure 20.

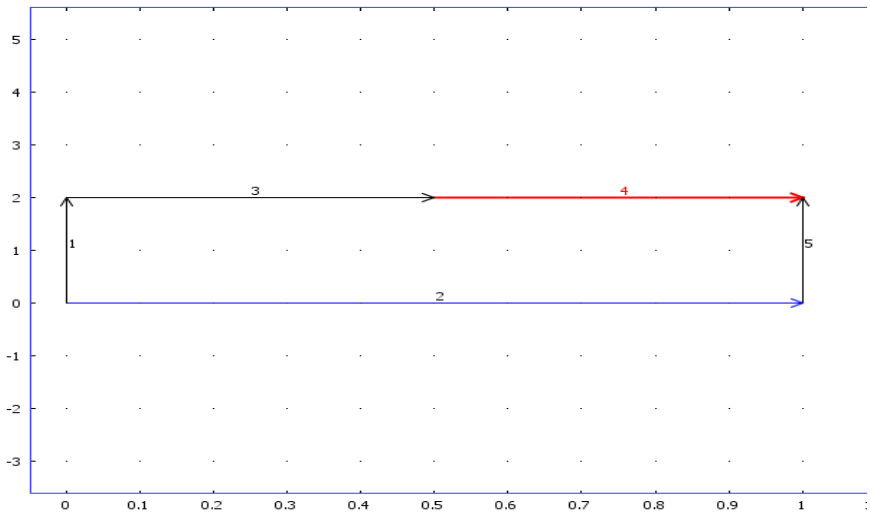

Figure 20: geometry and boundary setting for second M-S model

Subdomain and Boundary Settings

The domain of the solution comprises the entire rectangular enclosure. Diffusive flux is the dominant transport mode in this domain. For this isothermal system, the temperature and pressure in the container are constants as given in Table 4. The velocity components in the free fluid subdomain are congruently given by diffusive flux expressions. In particular

$$u = -\frac{D_{ij}}{wN_2\,\rho}\frac{\partial w_{N_2}}{\partial x}$$

Equation 27

$$v = -\frac{D_{ij}}{wN_2\,\rho}\frac{\partial w_{N_2}}{\partial y}$$

Equation 28

Species boundary conditions are necessary at each of the four boundaries depicted in Figure 19. At boundary 1 the species mass fraction is stated as given by the equilibrium-governed sublimation partial pressures for Zn and O_2 in the work of Tena-Zaera.

Boundaries 2 and 3 are insulation boundaries, namely the governing equation at these boundaries is

$$\vec{n} \cdot \left(- D \bigtriangledown c \right) = 0$$

Equation 29

Boundary 4 is the boundary that defines the system. In the work of Tena-Zaera on PVT growth of ZnO, this boundary is termed the crystal interface and is modeled as a flat boundary on which the reaction term is mimicked by a flux. In the present model, however, we have accounted for the reaction term fully by postulating mass action kinetics. The mass reactive flux is then given by

$$J = \left(k_1 \, w_{O_2}^2 \right) \rho$$

Equation 30

The value of the reaction rate constant was obtained by extrapolating the values for ZnO production rate at the model's conditions from the modeling work of Tena-Zaera et al. as in the previous model.

In contrast, the reaction term in the second model in this mode, hereafter referred to as the MS mode, was accounted for by means of a diffusive flux at that boundary in accordance with the work of Rosenberg et al and Ramachandran et al; namely, the condition governing boundary 2 in Figure 20 is

$$J_{O_2} = - \rho \, \frac{D}{1 - wO_{2,0}} \frac{\partial wO_2}{\partial x}$$

Equation 31

For the first model the domain of the solution comprised a total of 2802 degrees of freedom. A uniform triangular mesh was adopted for the solution as shown in Figure 21.

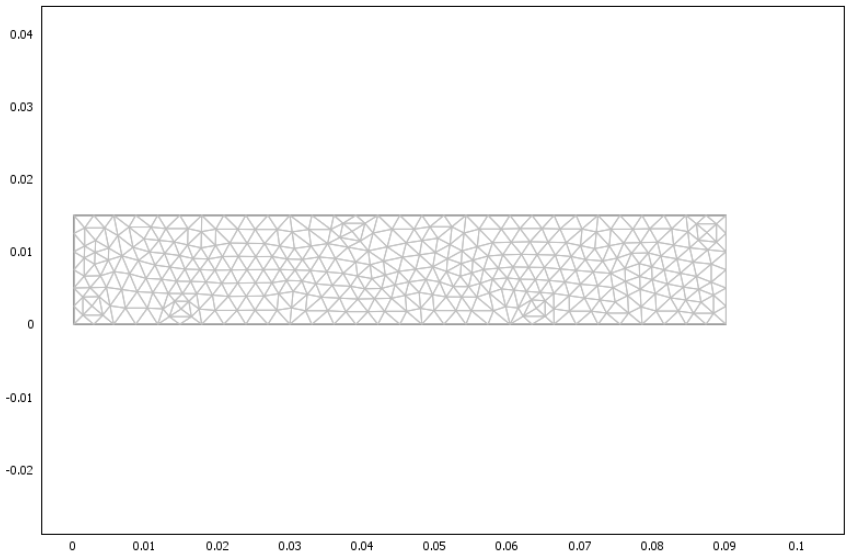

Figure 21: mesh configuration for Maxwell-Stefan Diffusion Model

A parametric non-linear solver was employed in computing the solution in both models. The parameter of choice was the system total pressure. Variations of this parameter are in accordance to what in an experimental set-up would be deemed the manipulated variable.

Model 3: non-isothermal transport

In order to model PVT more accurately, it is desired to incorporate thermal variations and their effect on the flow and ultimately on the ZnO growth rate. In the experimental set-up at CU, thermal variations occur as a consequence of heat conduction through the quartz reactor walls, which is induced by radiation from a resistive heater, and also as a consequence of the convective heat transfer in the free fluid. Indeed, it can be seen from the experimental temperature profile depicted in Figure 12 that the temperature shows important variations along the axial cylindrical direction. Moreover, most published works on PVT introduce wall temperature gradients and account for energy transport in the solution domain. Introducing thermal variations results in a comprehensive model of transport phenomena, which includes momentum, mass and energy transport through different modes; coupling of the highly non-linear transport equations for these quantities results in an intricate numerical system that, in its complete form, resists analytical

solutions. In spite of the power of a computational approach, it is necessary to make important simplifications in order to model the system.

The models in this mode seek to illustrate the interactions of temperature, concentration and velocity in PVT synthesis of ZnO. The systems will be defined, the unknowns identified, a corresponding number of equations postulated, boundary and subdomain conditions specified and finally simplifying assumptions stated.

Thermal fluid interactions

Model Definition

Based upon an axi-symmetrical cylindrical domain resembling that at CU, this model is a first attempt to study the effects of non-isothermal flow in critical variables such as temperature and velocity. The numerical model comprises laminar fluid flow in a quartz cylinder, the dimensions of which mimic the experimental set-up at CU. The fluid's composition is 20 ml O_2 per liter of N_2. At the entrance the fluid is fully mixed and has already developed a laminar profile. The maximum axial velocity is taken as the superficial velocity of the fluid at the inlet. The driving force for convective flow is the pressure differences along the axial direction; at the outlet the fluid encounters ambient pressure. The fluid properties correspond to a weighted average of the components' properties at STP, while those of the reactor walls are those of quartz.

Governing Equations

Momentum, mass and energy balances in cylindrical coordinates over a differential shell give rise to the dominant equations for the system. The non-isothermal equations for the fluid in general form are given in Equation 32 and Equation 33

$$\rho\frac{\partial \mathbf{u}}{\partial t} + \rho\mathbf{u}\cdot\nabla\mathbf{u} = \nabla\cdot[-p\mathbf{I} + \eta(\nabla\mathbf{u} + (\nabla\mathbf{u})^T) - (2\eta/3 - \kappa)(\nabla\cdot\mathbf{u})\mathbf{I}] + \mathbf{F}$$

Equation 32

$$\frac{\partial \rho}{\partial t} + \nabla \cdot (\rho \mathbf{u}) = 0$$

Equation 33

Equation 32, in particular, is worth expatiating upon. The term

$$\cdot [-p\mathbf{I} + \eta(\nabla \mathbf{u} + (\nabla \mathbf{u})^T) - (2\eta/3 - \kappa)(\nabla \cdot \mathbf{u})\mathbf{I}]$$

Is the total stress tensor, the third term of which account for the viscous contribution. For non-incompressible problems the viscous contribution is neglected since the divergence of the velocity vanishes. With regards to nomenclature the term η is the kinematic viscosity and κ is the dilatational viscosity.

The temperature profile is obtained from an energy balance in an interior differential volume. The general equation is

$$\rho C_p \frac{\partial T}{\partial t} + \bigtriangledown \cdot \left(- k \bigtriangledown T + \rho C_p T \vec{u} \right) = Q$$

However, assuming steady state the first term vanishes. The heat source term is also neglected, which implies that the radiation heat source from the furnace was neglected. Thus the simplified equation becomes

$$\bigtriangledown \cdot \left(- k \bigtriangledown T + \rho C_p T \vec{u} \right) = 0$$

Equation 34

Boundary and subdomain settings

The geometry showing the symmetry axis for r=0 and the two subdomains for the problem is shown in Figure 22. It should be noted that the axes and grid space are not equal in both dimensions.

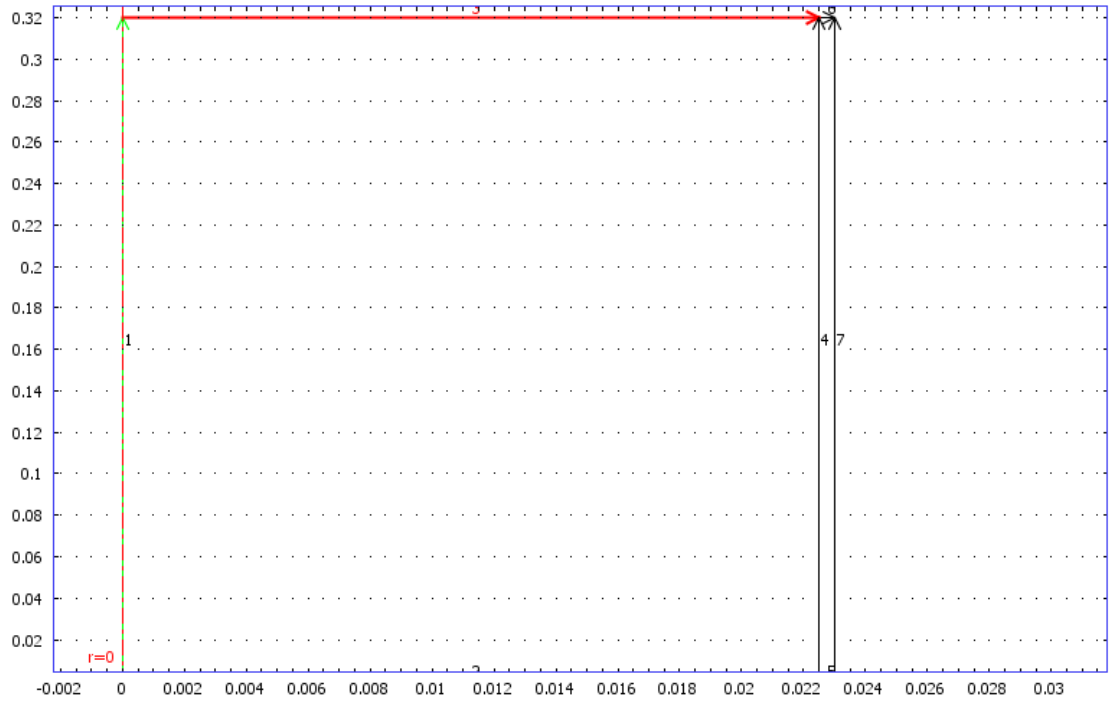

Figure 22: geometry and subdomains for non-isothermal flow

The first boundary in Figure 22 is the axis of symmetry, the second is the fluid inlet, the third the pressure governed outflow. The remaining boundaries correspond to solid boundaries and momentum balances here are hence disregarded.

Boundary conditions

No slip boundary conditions were applied to all solid boundaries. A superficial velocity of known value was given at the inlet and at the outlet a pressure flow condition was applied. The heat transfer boundaries were the following:

1. Axis of symmetry for boundary 1
2. A known inlet temperature to boundary 2
3. Convective heat flux at boundary 3
4. Insulation at the boundaries 5 and 7
5. Known inlet temperature at r=0 of the solid.

A triangular non-uniform mesh was chosen to compute the solution. A finer mesh size was applied to the solid fluid interface to better discern the effects of conductive heat transfer. The mesh details are shown in Figure 23.

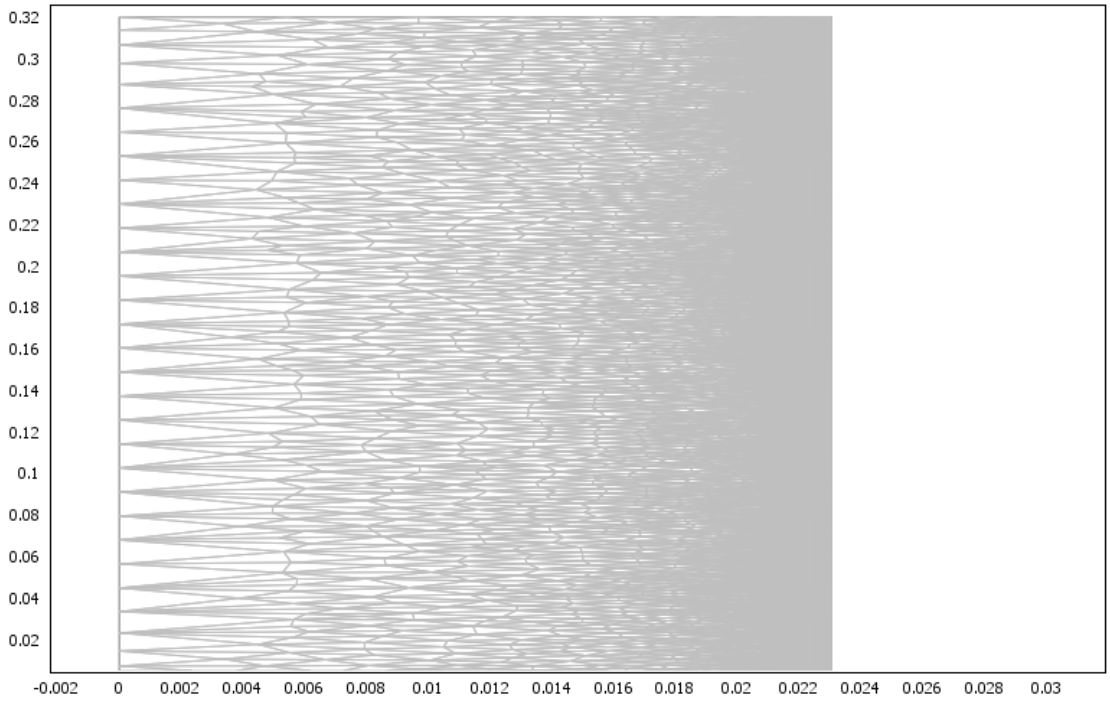

Figure 23: mesh layout for non-isothermal flow

Results and Discussion

Model 1: Diffusive and Convective Transport

Before engaging in a thorough analysis of the numerical results, it is instructive to revise convection and diffusion from an analytical standpoint. The relative effects of convection and diffusion can be gauged by proposing a simplified 1-D system. In allusion to the PVT system of interest, the simplified system will comprise the flow of crystal forming component A in carrier gas B. The closed ampoule, modeled by a Cartesian rectangle, has a sublimation source at the leftmost boundary and a crystallization interface at the rightmost boundary. Component B is quantitatively rejected at the crystallization boundary. For this model, complete incompressibility is assumed such that the density is not a function of the thermal component. A mass balance on an interior differential slab at steady state conditions gives rise to a second order ODE in concentration, namely

$$-D_i \frac{\mathrm{d}c_i^{\,2}}{\mathrm{d}x^2} + c_i \vec{u} = 0$$

Equation 35

Gives the results of a constant total flux at the interior. This second order linear ODE in concentration can be readily solved analytically with the following by expressing two boundary conditions. The concentration at the inlet is known and the total fluxes at the two extremes are equal in magnitude. With these, Equation 35 can be solved by a variation of parameters technique that accounts for the dependence of velocity on position. The solution to Equation 35 is then

$$c(x) = (co - \_C2)\, \mathrm{e}^{\left(\frac{\sqrt{u}\, x}{\sqrt{\mathrm{D}}}\right)} + \_C2\, \mathrm{e}^{\left(-\frac{\sqrt{u}\, x}{\sqrt{\mathrm{D}}}\right)}$$

Equation 36

Inserting the boundary conditions to evaluate the constant of integration C2 we obtain:

$$c(x) = C - (C - co)\exp\left(\frac{Pex}{L}\right)$$

Equation 37

In Equation 37 C denotes the total concentration as given by the ideal gas law.

The argument of the exponential term, that is uL/D_{AB}, is effectively the ratio of advective to diffusive transport, which we identify as the Peclet number. Thus we can conduct a parametric analysis by varying the magnitude of the Peclet number. Clearly the higher Pe the higher the convective domination and the reverse is also true. Greenwell et al. found that at a small Pe the inert species B can counter-diffuse, following the no-pass boundary condition of B at the crystal interface. At higher Pe, however, the convective transport of A effectively overrides the counter-diffusion of B. Since B cannot counter-diffuse, it accumulates at the crystal growing boundary, which results in the formation of a diffusion boundary layer.

Having obtained an analytical interpretation based on dimensionless analysis, we now proceed to discuss the numerical results.

Leaching of a solute in laminar flow

Inherent to any numerical modeling, is that the results are often displayed in the form of plots rather than concrete numerical values. In this case, we choose as a visualization method a three dimensional surface plot the height of which is given by the concentration and the colors correspond to the velocity profile. The plot is seen in Figure 24

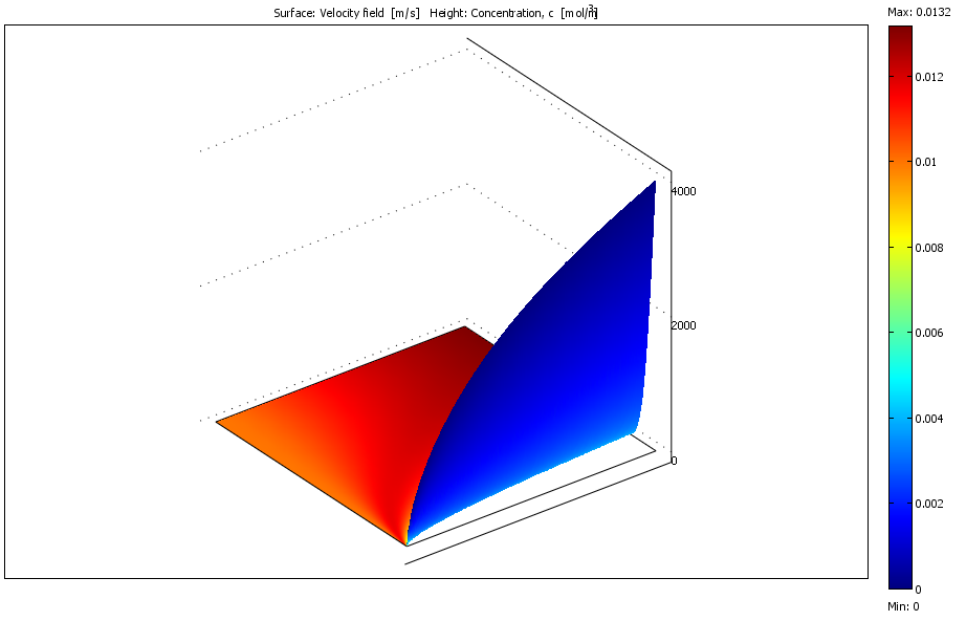

Figure 24: velocity- concentration plot for diffusion and convection

This kind of surface plot is useful to visualize the extension of the viscous and diffusion boundary layers into the bulk fluid. It can be seen that the viscous boundary layer extends further than the diffusion boundary layer, indicating the dominance of convective transport. We can also reverse the plot and get the same information, perhaps easier to interpret.

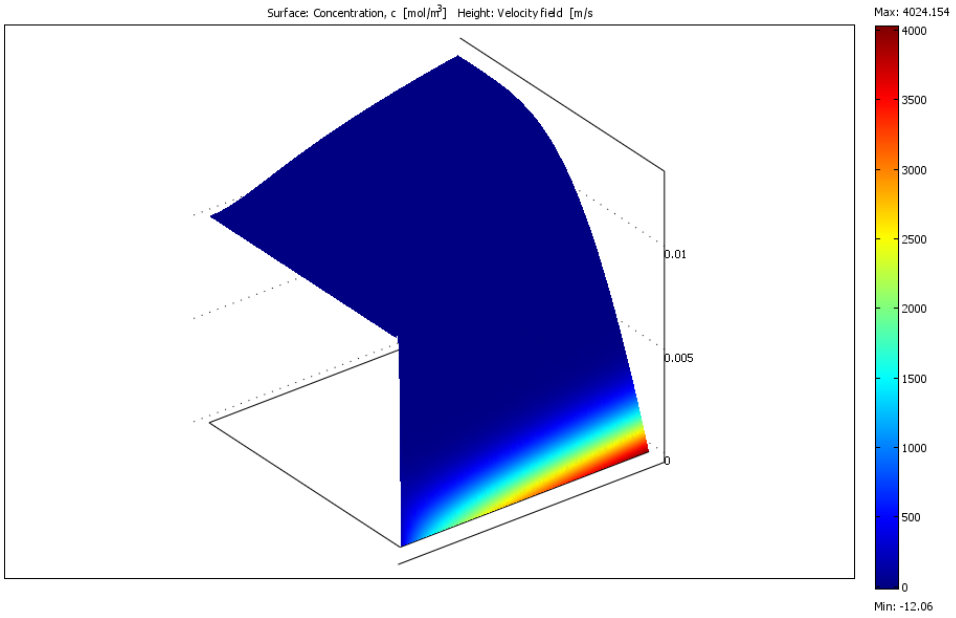

Figure 25: concentration-velocity plot for diffusion and convection

This exercise allowed us to gain perspective on how to represent the dominance of one transport mode over another. As can be seen in Figure 24 and Figure 25 for this leaching process, solute diffusion predominates only at the entrance; further downstream of the entrance pressure driven convection overrides diffusion. Alternatively, we can interpret the results in terms of the extent of reaction based on position. If we consider leaching a chemical reaction, then the extent of reaction is higher at the entrance, when significant concentration gradients are observed and falls with axial distance. For open cylindrical PVT settings such phenomena might also be observed. If mass transport is the rate governing step in crystal forming reactions in this set up, then the pressure drop across the reactor should be monitored to ensure that convective transport does not inhibit diffusive transport in the radial direction.

Vapor Transport in Diffusion and Convection

The final results of the this model were produced after numerous attempts at defining a system that would realistically represent the experimental conditions and would be, simultaneously, sufficiently numerically stable to achieve convergence. A compromise between fidelity with the experimental set up at Chulalongkorn University and ease of convergence was finally achieved and the results of such set up are presented in this section. Nevertheless, it is useful to identify some of the previous attempts and the possible reasons for their failure.

The most problematic aspect of this model was contained in accounting for the reaction term. Although COMSOL offers the possibility of including reaction in the bulk phase, the convergence criteria for such a model is perhaps too stiff to allow us to flexibly include the many intricacies of PVT; moreover, for the ZnO system reaction is thought to occur selectively at the growing crystal. Although experiments at CU show that ZnO deposits throughout the reactor, which may validate the hypothesis that reaction occurs in the bulk phase, the models will be built upon the assumption that the crystal grows selectively at a single boundary. To circumvent the difficulty of accounting for reaction dynamically in the fluid, it is possible to account for reaction by defining it as a boundary condition. Many modelers have devised very ingenious methodologies to this end. In particular, the reaction term has been mimicked by introducing a “reaction velocity” which plays the role of the velocity term in the convective contribution to total flux. Such approach, though theoretically

appealing is difficult to implement since the reaction term must be counteracted by an inlet velocity to ensure that steady state is respected. Moreover, the "reaction velocity" is intrinsically a function of the local concentration, which implies that the boundary condition takes the form of a partial differential equation on oxygen concentration. Since oxygen concentration is one of the dependent variables, an iteration scheme is required to asymptotically approach a solution. Such procedure is technically feasible but although many attempts were made to do so, none were successful. Other authors have adopted a similar approach with the significant difference that the reaction term is accounted for by the diffusive contribution to total flux at the boundary. The present model has adopted a form of this approach by introducing an effective, anisotropic diffusion coefficient which is concentration dependent. Nevertheless, the present model differs from that of Ramachandran et al in that the geometrical setting contains a convective subdomain, which is in accordance with the experimental conditions at CU, whereas the former authors have modeled a closed ampoule with dominant diffusive transport throughout. The boundary conditions imposed on their model include a velocity term which is dependent on the axial concentration profile. A crucial quantity for the model formulation is the reaction rate constant k_1. This quantity is dependent upon the global thermodynamic variables, pressure and temperature, and further there may be some dependence on the geometry of the system; there is some evidence that the aspect ratio, the ratio of length to diameter, may be particularly important. Nevertheless, for this model this quantity was considered to be constant. The value was calculated using the experimental data from Tena-Zaera at each pressure. According to the stoicheometry of the reaction and assuming mass action kinetics, the dependence of the reaction rate on oxygen concentration should be of the order of one half. Assuming this dependence, and acknowledging that the work of Tena-Zaera provides us with concentration values for both Zn and O_2 at the interface, a lumped kinetic rate constant was computed which accounted for the zinc concentration and the kinetic rate constant. Doing so allowed us to effectively postulate a reaction term based on the solute in our model exclusively. Nevertheless, when this value was used in conjunction with the ½ order of the reaction with respect to oxygen concentration the system became very unstable and it never converged. Hence an alternative approach was needed. It was assumed that the concentrations at the interface of oxygen and zinc were given by the stoicheometric requirements for the reaction; that is $P_{O2} = P_{Zn}$ doing so allowed us to establish the reaction order as being second order in oxygen concentration.

The kinetic rate constant was consequently computed from the modified expression coupled with the experimental value for reaction rate at the given conditions. This approach proved successful.

The convergence of the model is depicted in Figure 26. It can be seen from the plot that the convergence in monotonic until the fifth iteration after which the convergence value spikes rapidly to decline to a minimum from the seventh to the eight iteration. We should have expected uniform, monotonic convergence; instead this convergence behavior suggests that one of the parameters makes the system slightly unstable. A parametric investigation was conducted to determine the nature of this parameter, and it was found that the kinetic rate constant has the strongest effect on the convergence behavior. This result may suggest that the order of the reaction is ill defined, though more conclusive evidence would be needed to assert this.

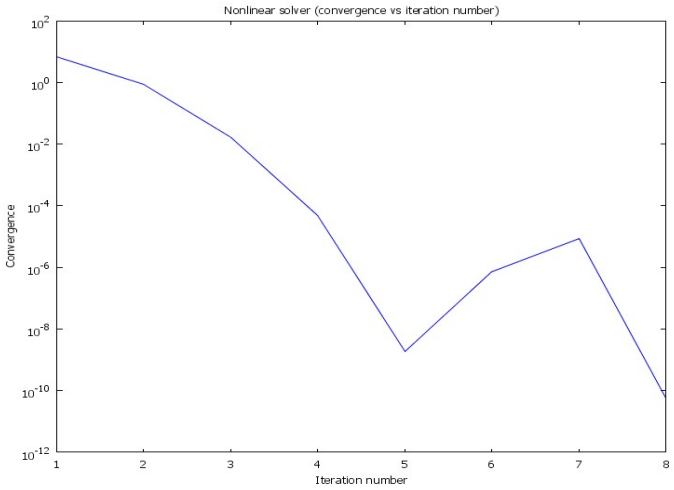

Figure 26: convergence of the solution

In spite of the particular behavior of the solution with regards to convergence, the model converged to a reasonable solution in only eight iterations. The subdomain of the solution comprised a total of 3110 degrees of freedom.

The discussion of the results for the model will be limited to the two quantities of interest: the extent of reaction as a function of the flow characteristics and the velocity distribution.

The oxygen concentration profile at different total pressures is captured in Figure 27. It can be seen in this figure that the oxygen concentration distribution varies strongly as a function of total pressure. Indeed, the concentration profile in the convective subdomain suggests that at low pressures, diffusive mass transport poses an important mass transfer resistance inhibiting the distribution of oxygen, which in turn can affect the reaction rate. On the other hand, however, at high pressures, the bulk flow velocity might be such that diffusion in the radial direction is hampered, thereby leading to low extents of reaction. In this open system set-up the most favorable pressure regime might of the order of 1 atm, where oxygen transport downstream is considerable and yet oxygen concentration is not displaced to a large extent toward the outlet.

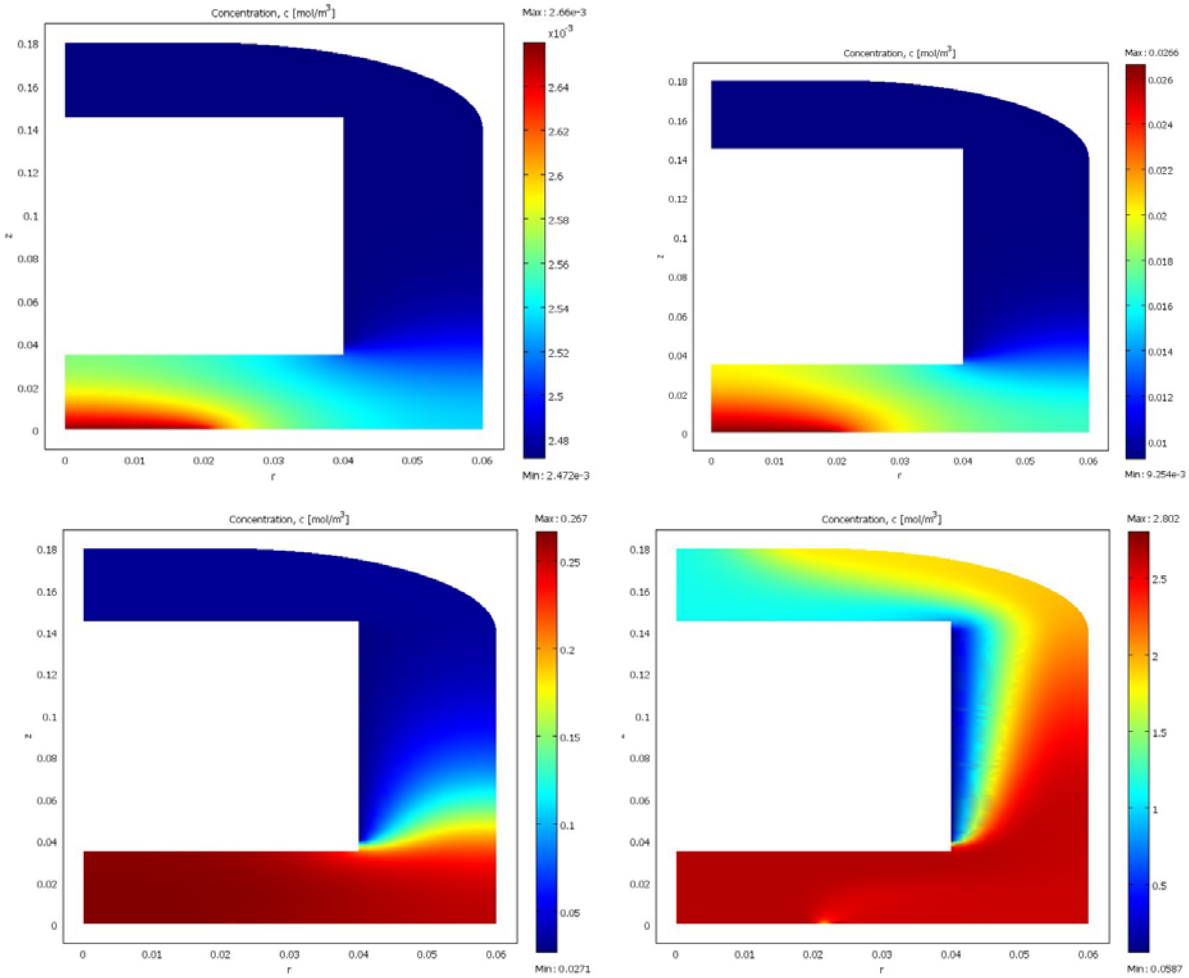

Figure 27: oxygen concentration profile in the reactor at different total pressures. Top right: 0.01 atm-Top left: 0.1 atm. Bottom right: 1 atm. Bottom left: 10 atm

It is also of interest to discern the nature of the flow; that is the distribution of convective and diffusive flux. Figure 28 displays the cell display number, effectively the ratio of convective to diffusive transport, as a function of system total pressure. It is clear from this figure that convective flux dominates in the free fluid subdomain, which is not surprise since this domain was defined in such a way as to ensure that such phenomenon would occur.

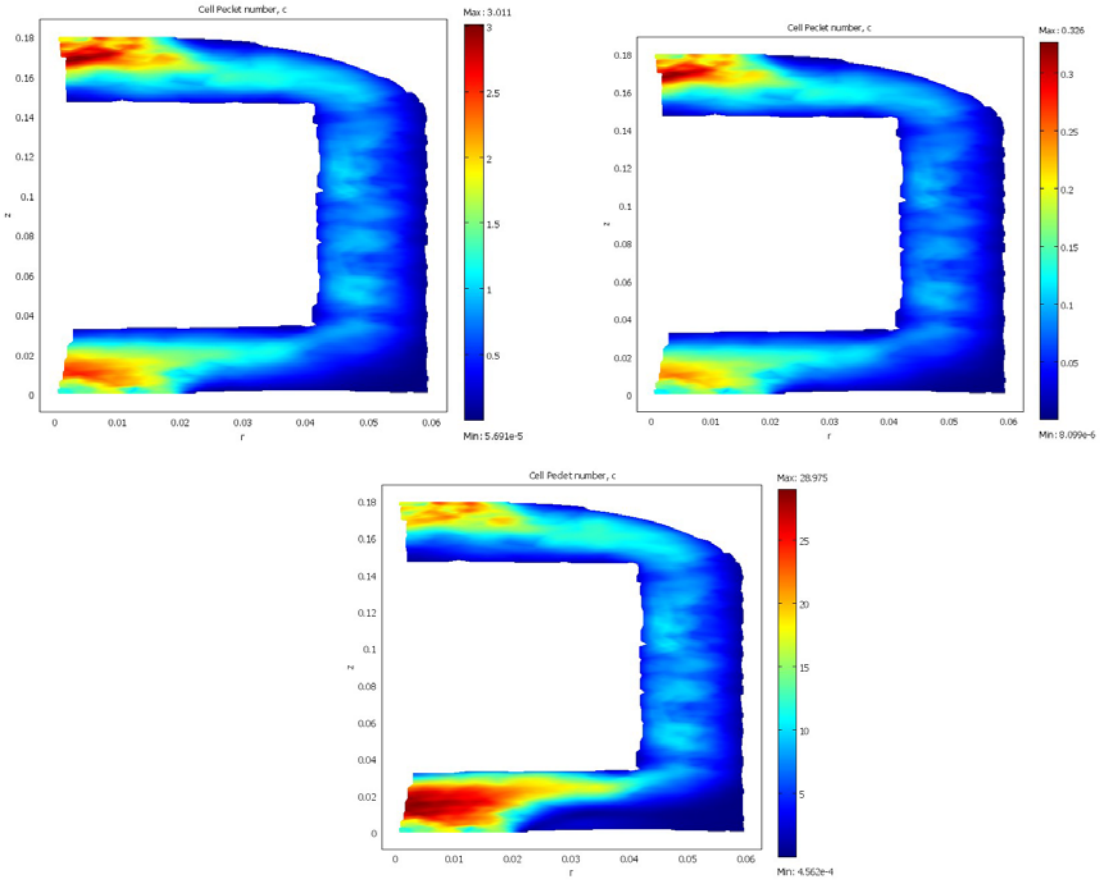

Figure 28: Cell Peclet Number at different pressures. Top right: 0.1 atm. Top left: 1 atm. Bottom: 10 atm

It can be seen from Figure 28 that little change in transport mode occurs in going form 0.1 to 1 atm. The same does not apply to higher pressures. Indeed, when total pressure was increased from 1 to 10 atm, convective flux dominance is well established in the convective subdomain even in the vicinity of the interface between the free fluid and the catalyst bundle. The Peclet number is of great importance, since there is an exponential dependence of concentration on it; hence small variation in the Peclet number, which can

result from changes in the aspect ration (ratio of length to diameter) can have a significant effect on concentration distribution.

The flow distribution in the reactor is well illustrated by Figure 29. We can see that at both inlet and outlet to the reactor, the velocity attains its highest magnitude, which we can attribute to convection dominance. The fact that the maximum velocity is attained at the outlet is evidence of the dominance of pressure induced convection, since the greatest pressure gradient occurs at this boundary. Congruent with mass transfer resistance postulate, slow flux at the free fluid – catalyst bundle interface is observed, this is in accordance with the results obtained by Tena-Zaera et al.

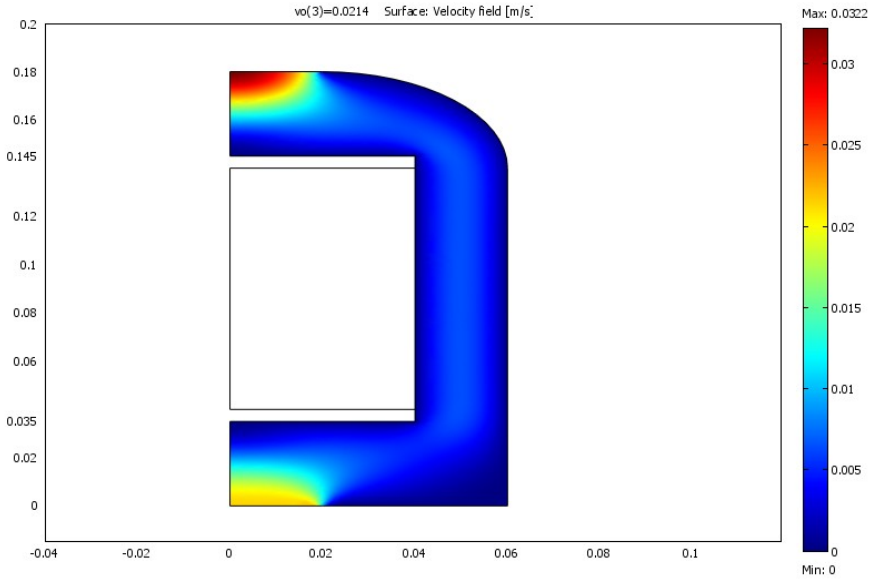

Figure 29: velocity distribution

A vector field plot is useful for illustrating more clearly the velocity behavior. One such plot is offered below

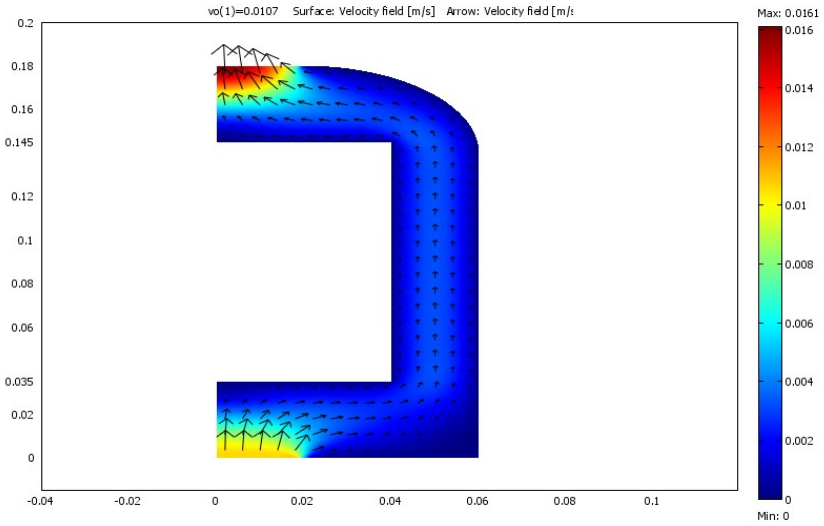

Figure 30: vector field velocity plot

The impact of the velocity distribution on reaction was investigated by using the inlet velocity as a parameter. Values for inlet velocity were chosen as multiples of the original value of vo at 1.07 x 10^2 m/s. The chosen values were vo, 1.5vo, 2vo.

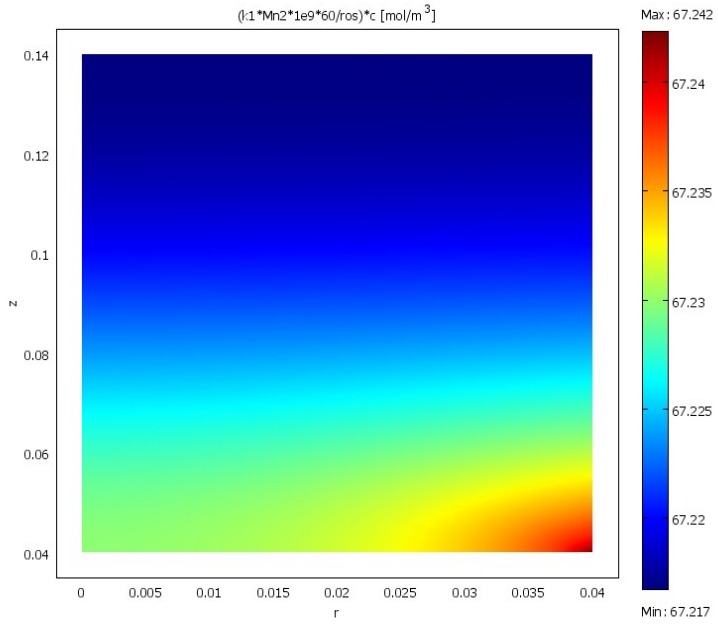

Figure 31: concentration distribution as a function of inlet velocity, vo

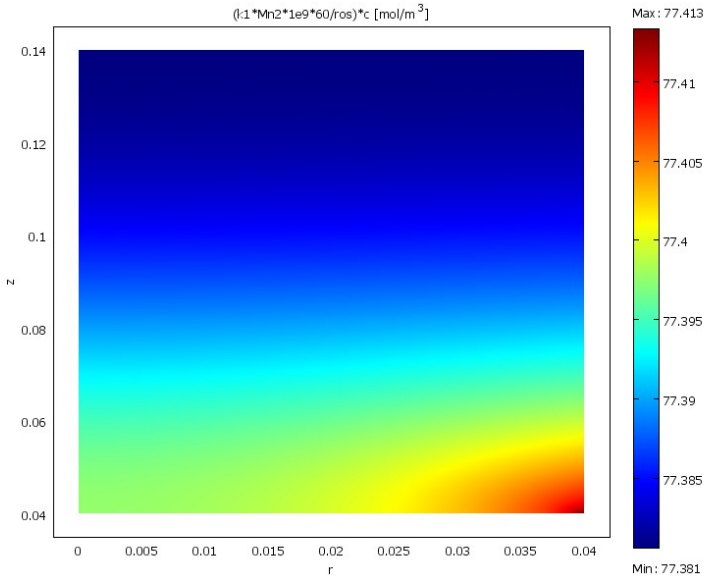

Figure 32: concentration distribution as a function of inlet velocity, 2vo

It can be seen from Figure 31 and Figure 32 that the inlet velocity has little effect on the oxygen distribution. Such behavior may be expected if reaction was diffusion dominated, which strongly appears to be the case.

Finally, the mesh independence of the model was evaluated by computing the solution at a finer mesh refinement. The results were invariant.

Model 2: 2-D multi-component diffusive flux

The results of these set of models is of significant relevance since the definition of the modeling environment closely resembles the progressive work of other authors on the PVT ZnO system. In fact, many authors have neglected the convective contribution to transport altogether in their treatment of PVT in closed cylindrical ampoules, arguing that the low pressure and dilute conditions characterizing these systems warrant the prevalence of diffusive transport (Markham, 1981). The major difference between the models of these authors and the model presented in this work is that in the present work isothermal conditions are assumed throughout, which affect the density and hence concentration gradients. Alternative works account for a linear wall temperature profile and make use of the energy equation in their system; this treatment implies a dependence of density and concentration upon temperature; moreover, such inclusion makes the incompressible flow assumption

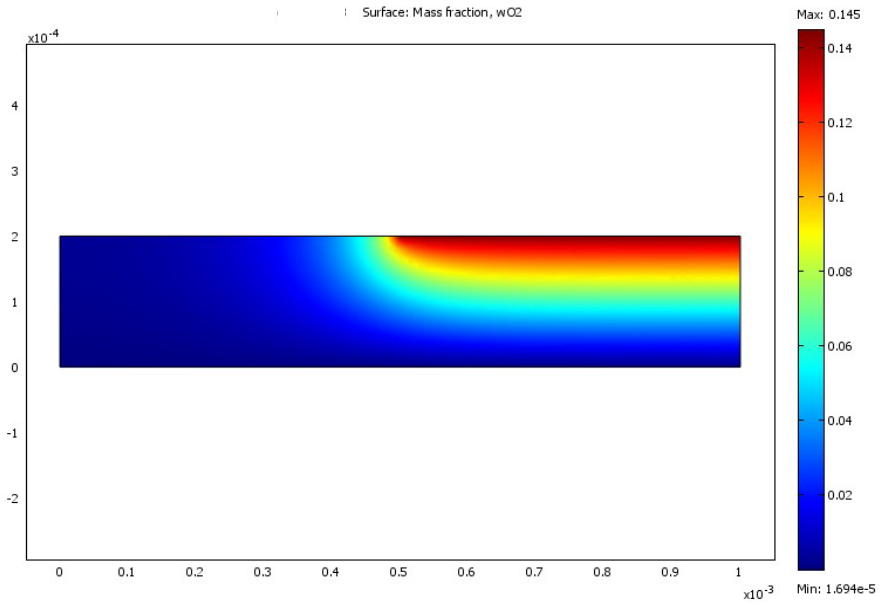

Figure 33: oxygen mass fraction distribution in MS mode from Model 2

invalid. Given the simplifications adopted in this work and the dominating boundary conditions the concentration profile for both species should follow a uniform gradient, being highest at the entrance and lowest at the crystal interface. Not surprisingly these were the observed results for both models in this mode.

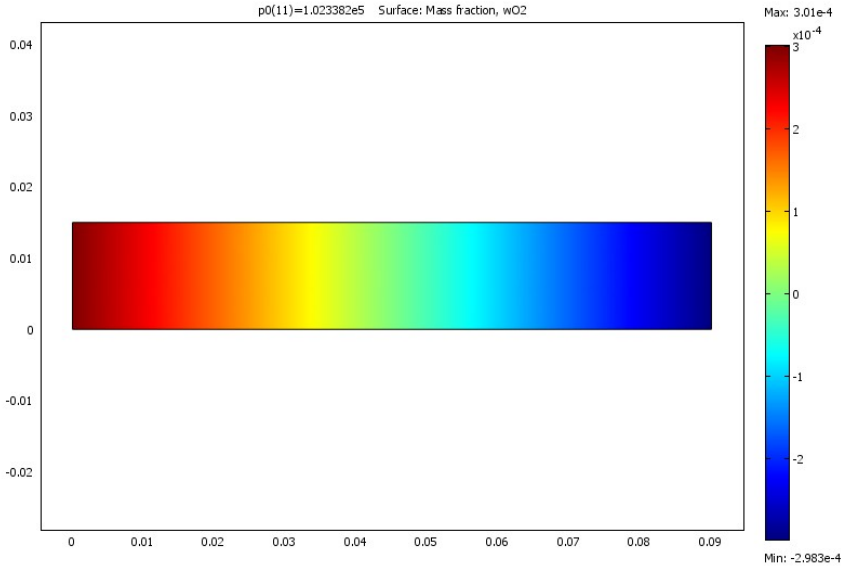

Figure 34: oxygen mass fraction distribution in MS mode, Model 1

The concentration profiles for oxygen, shown in Figure 33 and Figure 34 and the analogous data for Zn, in all respects identical in nature to that of oxygen, are evidence that the diffusive transport is governed by the concentration gradients in the reactor. The lowest reactant concentration is found in both models, without surprise, in the vicinity of the reacting surface. Since diffusive flux dominates both at the reacting surface and in the free fluid subdomain, no abrupt variations in concentration should be expected, and none are found. In fact, for the second model, where reaction is modeled as a diffusive flux, the boundary condition complies with the model almost in continuous fashion; that is, the partial differential equation for concentration might apply even at the boundary. The same is not true for the first model, where the flux at the interface is dominated by reaction.

More interestingly, however, is the surface flux for both species. Although the streamlines are linear as shown in Figure 35, congruent with a flow governed by a concentration gradient, the species flux presents many variations along both the axial and radial directions.

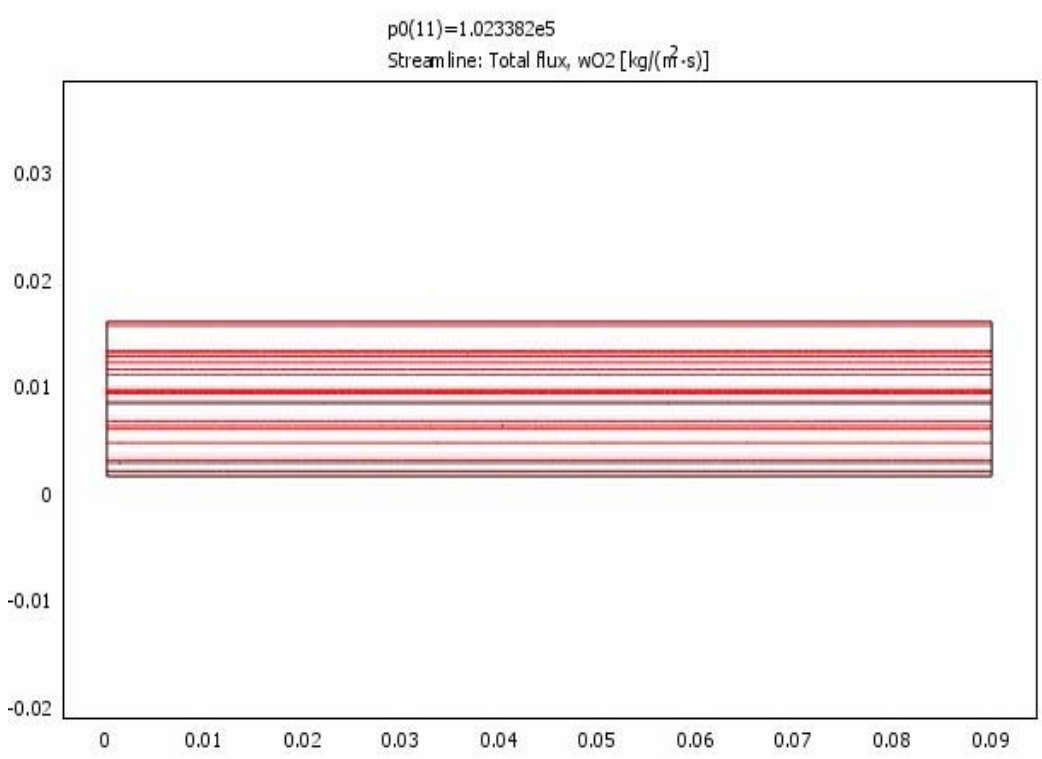

Figure 35: streamlines for flow in MS mode, Model 1

Nevertheless, a dominant axial component to the Zn flux, shown in yellow in Figure 36, prevails, so that the net transport of Zn is indeed occurring in the axial direction. Although the nature of the plot is similar, the magnitude of the axial oxygen flux in the axial direction in the free fluid domain is strikingly lower than that of Zn, as shown in Figure 37. One of the reasons for this disparity of fluxes may be related to the stoicheometry of the reaction since only one mol of O_2 is required for every reacting mole of Zn. Differences due to mass transport resistance associated with molecular weight should be negligible as the molar mass of both species is very similar.

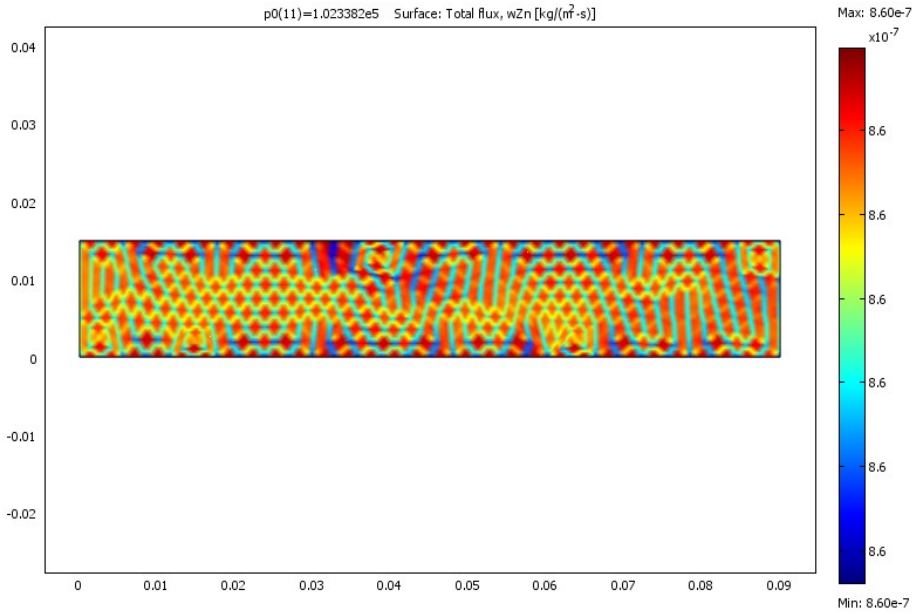

Figure 36: Zn total flux in MS mode, Model 1

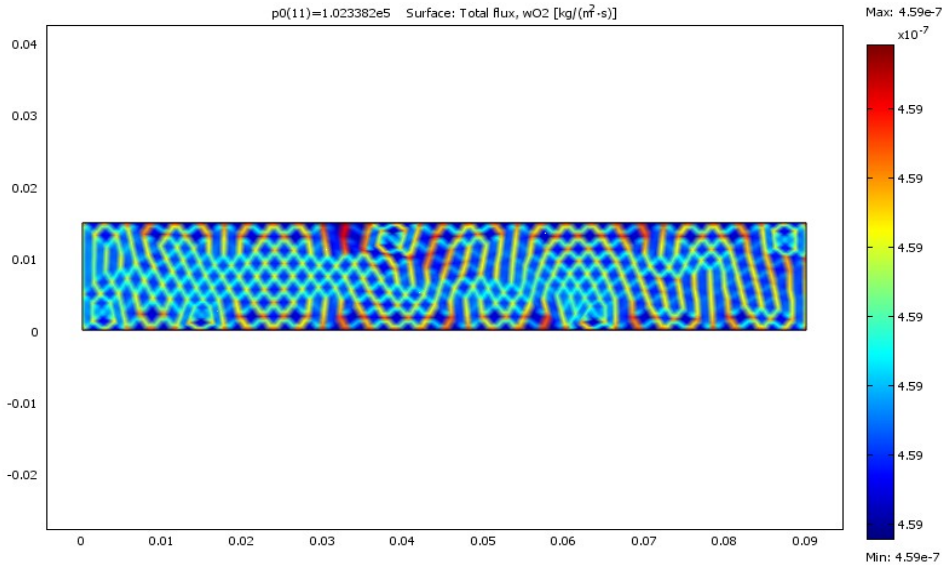

Figure 37: total oxygen mass flux in MS mode, Model 1

Lastly, we choose to depict the total magnitude of the velocity as shown in Figure 38.

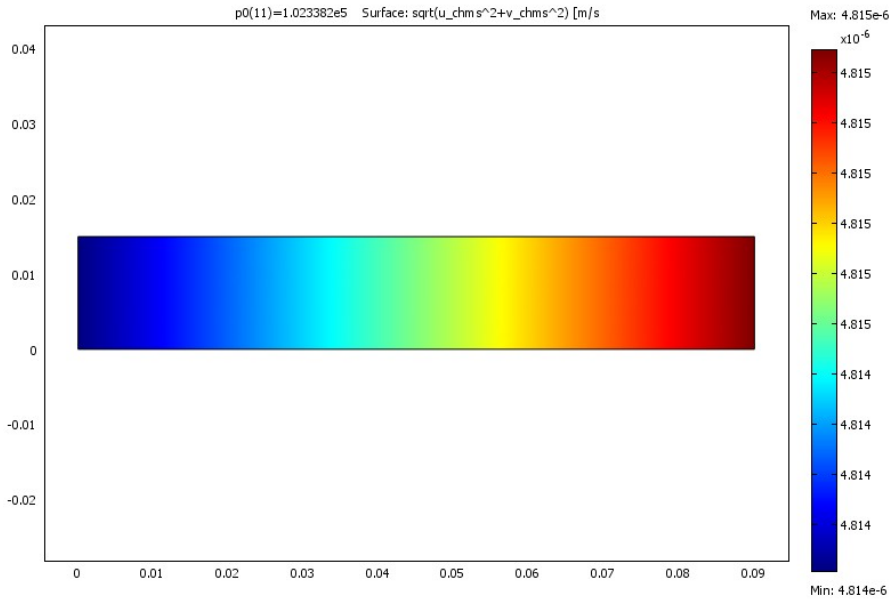

Figure 38: total velocity profile in MS mode, Model 1

Figure 38 is effectively the mirror image of the reactants' concentration profile. Defined with respect to nitrogen diffusive flux the velocity achieves its highest value in the vicinity of the reactive surface. This velocity distribution is explained by the species boundary condition at the interface; that is, the no flux condition for nitrogen. At this surface there is flow recirculation as nitrogen gas is rejected. Indeed counter-diffusion due to nitrogen concentration gradients in the vicinity of the interface may exist. Since the velocity in this expression is taken as the absolute value of the velocity vector field, it is not surprising to find the highest value at this surface for the reasons delineated above. The results of this simulation are encouragingly in accordance with the work of Greenwell et al. who used the Peclet number and a simplified model to arrive at the conclusion that in diffusive PVT there is counter-diffusion of inert component B at the crystal interface.

Model 3: Non-isothermal flow

Fluid-thermal interactions

To characterize the flow in PVT and obtain more accurate result it is important to determine whether free convection may be prevalent in the system. Much effort has been deposited in accounting for the gravitational effects in vertically oriented cylindrical ampoules inside which PVT takes place. These results are not pertinent for the experimental work on ZnO synthesis; although their academic allure cannot be denied. Nevertheless, considering the non-isothermal conditions under which ZnO synthesis takes place, it is important to investigate whether free convection resulting from fluid thermal expansions can affect the flow and, ultimately, the crystal growth rate. It should noted that buoyant forces in free convection determine the flow patterns of fluid and that in this mode of convection the Nusselt number is a function of the Grashoff and Prandtl number as opposed to being a function of the Reynolds and Prandtl number as in forced convection. Computational problems involving free convection are complicated by the fact that the velocity and thermal fields interact dynamically, so iterative subroutines are required in the calculations.

This model investigates the effects of fluid-thermal interactions and quantifies the thermal expansion of the fluid. Moreover, the model is of realistic importance, since the dimensions, materials and conditions simulated correspond to the experimental set-up at CU. In addition, the validity of the temperature profile obtained from the numerical solution can be assessed with experimental data.

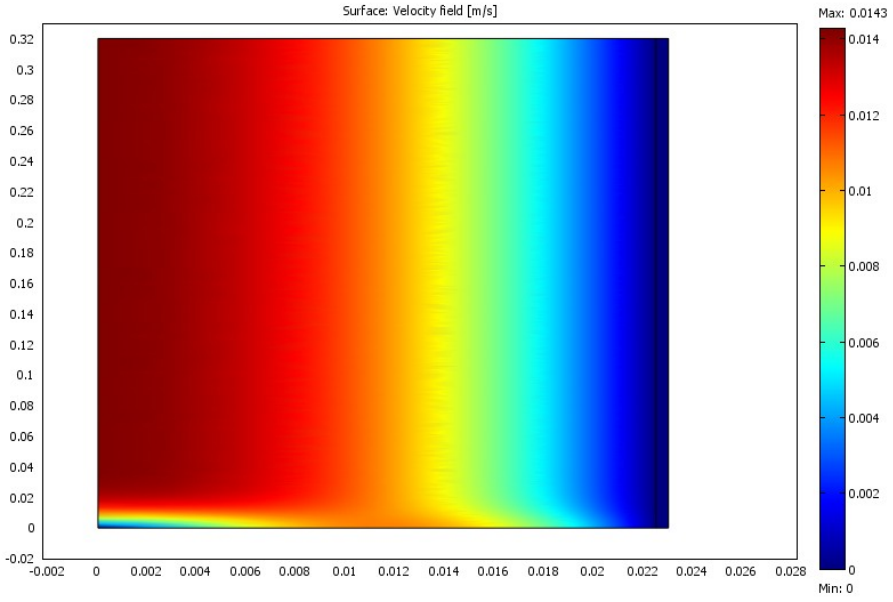

Figure 39: velocity profile for non-isothermal flow

Figure 39 is important in illustrating the parabolic profile that develops in the open cylindrical setting in CU. It can be seen in such figure that at the fluid outlet laminar flow is fully developed, which validates some of the assumptions made in earlier models. A clear picture of the laminar profile can be seen in Figure 40.

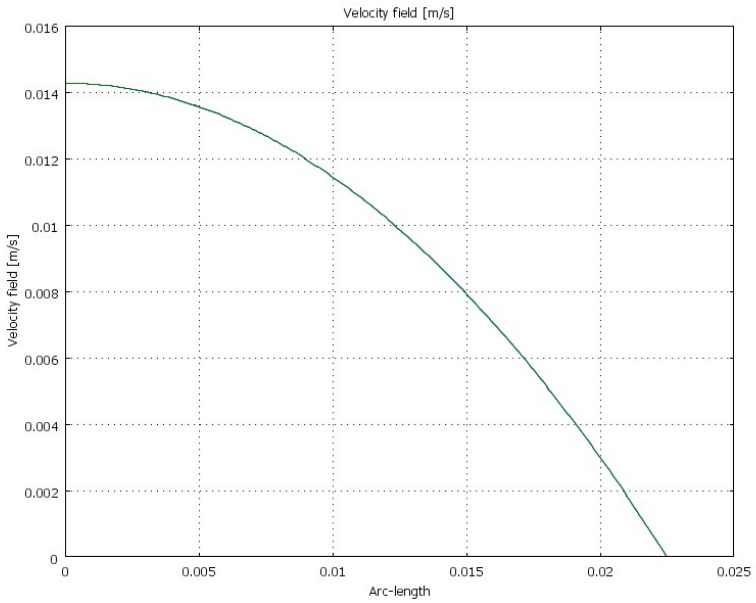

Figure 40: axial velocity profile in non-isothermal flow

In their most recent publication on the subject of PVT, Rosenberger et al. noted that the constant gradient temperature profile that has been traditionally employed on the ampoule side wall for numerical simulations gave rise to erroneous results. In fact, they argued, it under-predicted growth rates, as it resulted in vapor supersaturation throughout the cylinder. Figure 41, however, exemplifies how the assumption of a constant temperature gradient in the axial direction is validated for the set-up at CU.

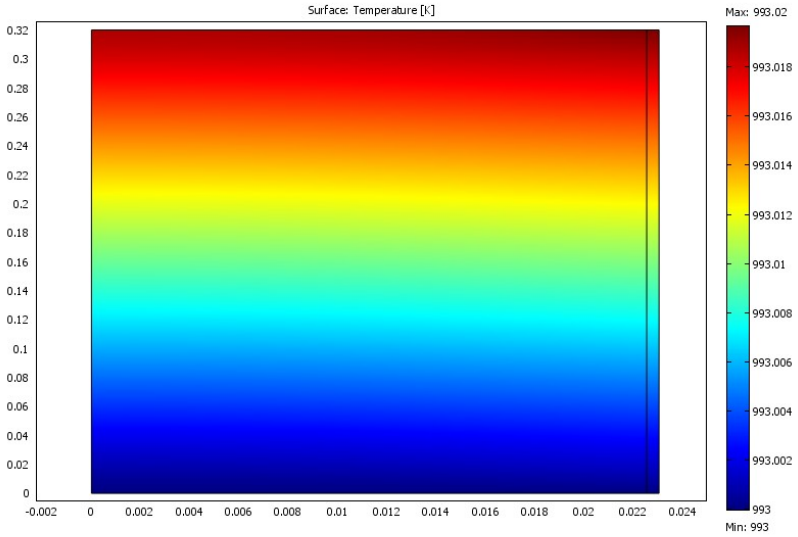

Figure 41: axial temperature profile in non-isothermal flow

In addition the temperature profile plot in Figure 12 provides a graphical validation of the numerical results as the experimental temperature profile also suggests a linear temperature profile along the axial direction.

Finally, the magnitude of the fluid thermal expansion was assessed by taking the ratio of the outlet average velocity to the average inlet velocity. The average velocity was obtained by a surface integration of the velocity field at the end boundaries. The thermal expansion is a negligible 0.0035%, which implies that even in non-isothermal mode, the assumption of an incompressible fluid is valid.

Conclusion

Upon completion of this major qualifying project a set of numerical models directly targeting PVT synthesis of ZnO were developed. These models incorporate many of the intricacies characteristic of physical vapor transport and offer a strong theoretical background by which to interpret the results of both numerical and experimental results. With these models and their results at hand, experimental conditions can be adopted that will favor crystal formation. Moreover, these models flexibly allow us to conduct further parametric studies to investigate the effect of changing one variable on the rate of crystal formation. Such a parametric analysis would be complicated in an experimental set-up due to the multitude of confounding interactions between variables, the time commitment of the experiments and last but not least the cost of such procedure.

In this work we have studied the relative dominance of diffusive and convective transport in a reactive environment; moreover, we have explored how interactions that arise in multi-component mixtures can affect the species' distribution in the reactor. Lastly, we have explored the effect of thermal-fluid interactions on the density and velocity fields, which in turn influence the species concentration and, in so doing, also have an important effect on crystal growth rate.

A theoretical exploration of physical vapor transport that encompasses a significant amount of the complexities inherent in this process is an exercise in understanding the nature of transport phenomena and its effect on experimental results. Such understanding allows us to better design the equipment and conditions for experimental setups and provides us with a theoretical background to interpret results.

Bibliography

1) Zhang, Jun et al. "Shape controlled synthesis of ZnO nano and microstructures." Journal of Crystal Growth 280 (2005) 508-515.

2) Wu, Run. "Formation of tetrapod ZnO nanowhiskers and its optical properties." Materials Research Bulletin vol. 39 637-645, 2004

3) Shen, Guozhen et al. "Morphology Controlled Synthesis of ZnO Nanostructures by a Simple round to Round Metal Vapor Deposition Route. J. Phys. Chem. B 2006, 110, 3973-3978

4) Zhou, Zuowan et al. "Studies on the kinetics process of tetra-needle-like ZnO whisker growth." Journal of Crystal Growth 276 (2005) 317-320

5) Park, Joodong et al. "Two-step evaporation process form formation of aligned zinc oxide nanowires." Journal of Crystal Growth 258 (2003) 342-348

6) Gen, Tien- Chien et al "Numerical investigation on cold gas dynamic spray process with nano- and microsize particles." International Journal of Heat and Mass transfer 48 (2005) 4384-4396

7) Xing, Tal and Stern, Fred. "Introduction to Computational Fluid Dynamics." Mechanics of Fluids & Transport Processes, University of Iowa, 2003.

8) Computational Fluid Dynamics. Wikipedia, Wikipedia Foundation Inc. Jan. 24 2007. Accessed Jan. 25 2007. http://en.wikipedia.org/wiki/Computational_fluid_dynamics

9) Transport Phenomena 2nd Edition. Bird, Byron, Steward, Warren & Lightfoot, Edwin. John Wiley & Sons, Inc, 2002.

10) Klosse, K & Ullersma, P. "Convection in a chemical vapor transport process." Journal of Crystal Growth 18 (1973) 167-174

11) Greenwell, D.W, Markham, B.L & Rosenberger, F. "Numerical Modeling of diffusive physical vapor transport in cylindrical ampoules." Journal of Crystal Growth 51 (1981) 413-425

12) Markham, B.L. et al. "Numerical Modeling of diffusive-convective physical transport in cylindrical vertical ampoules." Journal of Crystal Growth 51 (1981) 426-437.

13) Markham, B.L & Rosenberger, F. "Diffusive-Convective vapor transport across horizontal and inclined rectangular enclosures." Journal of Crystal Growth 67 (1984) 241-254

14) P. Bontoux, Markham, B.L, Rosenberger, F et al. "Convection in the vertical midplane of a horizontal cylinder. Comparison of two-dimensional approximations with three-dimensional results." International Journal of Heat Mass Transfer 29 (1086) 227-240.

15) Rosenberger, F et al. "Physical vapor transport revisited." Journal of Crystal Growth 171 (1997) 270-287

16) Tena-Zaera, R et al. "Study of the ZnO crystal growth by vapor transport methods". Journal of Crystal Growth 270 (2004) 711-721

17) Ramachandran, N, Su, Ching-Hua et al. "Modeling studies of PVT growth of ZnSe: current status and future course." Journal of Crystal Growth 208 (200) 269-281

18) Zuo, Ran & Wang, Wenkui. "Theoretical Study on chemical vapor transport of $ZnS-I_2$ system. Part I. Kinetic process and one-dimensional model. Journal of Crystal growth 236 (2002) 687-694

19) Zuo, Ran & Wang, Wenkui. "Theoretical Study on chemical vapor transport of ZnS-I_2 system. Part II: numerical modeling. Journal of Crystal growth 236 (2002) 695-710
20) Saeys, Mark. "Ab Initio Reaction Path Analysis of Benzene Hydrogenation to Cyclohexane on Pt (111)." J. Phys. Chem. B 109, 2005, 2064-2073

APPENDIX A

Dimensionless numbers

Peclet Number, Pe

Ratio of advection to thermal diffusion

$$Pe = \frac{lv}{\alpha}$$

Prandtl Number, Pr

Ratio of momentum boundary layer thickness to thermal boundary layer thickness. Effectively, the ratio of viscous diffusion rate to thermal diffusion rate.

$$Pr = \frac{\nu}{\alpha}$$

Nusselt Number, Nu

Ratio of convective heat transfer vs. conductive heat transfer

$$Nu = \frac{hL}{k}$$

Brinkham number, Br

Ratio of viscous thermal dissipation to conduction

$$Br = \mu \frac{v_b^2}{k} \left(T_b - T_0 \right)$$

Schmidt Number, Sc

Ratio of momentum diffusivity to mass diffusivity

$$Sc = \frac{\nu}{D_{AB}}$$

Sherwood Number, Sh

Ratio of length-scale to the diffusive boundary layer thickness

$$Sh = \frac{K_c L}{D}$$

Where K_c represents the overall mass transfer coefficient

Reynolds Number, Re

Ratio of inertial forces to viscous forces

$$Re = \frac{\rho v_s L}{\mu} = \frac{v_s L}{\nu}$$

Grashof Number, Gr

Ratio of buoyancy force to viscous force

$$Gr = \frac{g\beta \left(T_s - T_\infty\right) L^3}{\nu^2}$$

Rayleigh number, Ra

The product of the Grashof number and the Prandtl number. Effectively, ratio of buoyancy force to thermal diffusion.

$$Ra = Gr \times Pr = \frac{g\beta \left(T_s - T_\infty\right) x^3}{\nu\alpha}$$

Appendix B: Computational details of the simulations

Leaching of a solute in laminar flow

Geom1

Space dimensions: 2D

Independent variables: x, y, z

5.1. Mesh

5.1.1. Mesh Statistics

Number of degrees of freedom	17857
Number of mesh points	1429
Number of elements	2619
Triangular	2619
Quadrilateral	0
Number of boundary elements	237
Number of vertex elements	4
Minimum element quality	0.713
Element area ratio	0.002

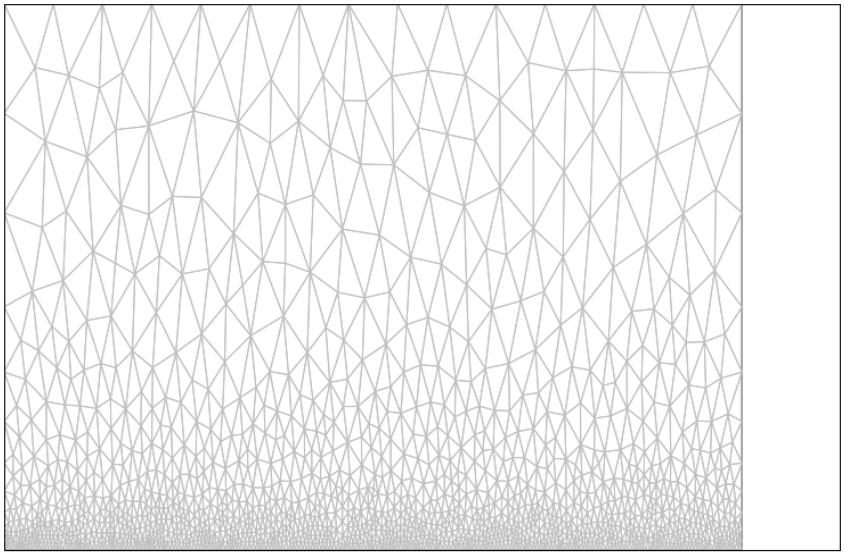

5.2. Application Mode: Incompressible Navier-Stokes (chns)

Application mode type: Incompressible Navier-Stokes (Chemical Engineering Module)

Application mode name: chns

5.2.1. Application Mode Properties

Property	**Value**
Default element type	Lagrange - P_2 P_1
Analysis type	Stationary
Stress tensor	Total
Corner smoothing	Off
Non-isothermal flow	Off
Turbulence model	None
Non-Newtonian flow	Off
Brinkman on by default	Off
Frame	Frame (ref)
Weak constraints	Off

5.2.2. Variables

Dependent variables: u, v, p, logk, logd, nxw, nyw

Shape functions: shlag(2,'u'), shlag(2,'v'), shlag(1,'p')

Interior boundaries not active

5.2.3. Boundary Settings

Boundary		2	1
Type		No slip	Inflow/Outflow velocity
x-velocity (u0)	m/s	0	**v0**

Boundary	3	4
Type	Slip/Symmetry	Normal flow/Pressure
x-velocity (u0)	0	0

5.2.4. Subdomain Settings

Subdomain		1
Integration order (gporder)		**4 4 2**
Constraint order (cporder)		**2 2 1**
Density (rho)	kg/m^3	**rho**
Dynamic viscosity (eta)	$Pa \cdot s$	**mu**

5.3. Application Mode: Convection and Diffusion (chcd)

Application mode type: Convection and Diffusion (Chemical Engineering Module)

Application mode name: chcd

5.3.1. Application Mode Properties

Property	**Value**
Default element type	Lagrange - Quadratic
Analysis type	Stationary
Equation form	Non-conservative
Equilibrium assumption	Off
Frame	Frame (ref)
Weak constraints	Off

5.3.2. Variables

Dependent variables: c

Shape functions: shlag(2,'c')

Interior boundaries not active

5.3.3. Boundary Settings

Boundary		4	1, 3
Type		Convective flux	Concentration
Inward flux (N)	$mol/(m^2 \cdot s)$	0	0

Boundary	2
Type	Flux
Inward flux (N)	**flux**

5.3.4. Subdomain Settings

Subdomain		1
Diffusion coefficient (D)	m^2/s	**D**
x-velocity (u)	m/s	**u**
y-velocity (v)	m/s	**v**

6. Solver Settings

Solve using a script: off

Analysis type	Stationary
Auto select solver	On
Solver	Stationary
Solution form	Automatic
Symmetric	Off
Adaption	Off

6.1. Direct (UMFPACK)

Solver type: Linear system solver

Parameter	**Value**
Pivot threshold	0.1
Memory allocation factor	0.7

6.2. Advanced

Parameter	**Value**
Constraint handling method	Elimination

Null-space function	Automatic
Assembly block size	5000
Use Hermitian transpose of constraint matrix and in symmetry detection	Off
Use complex functions with real input	Off
Stop if error due to undefined operation	On
Type of scaling	Automatic
Manual scaling	
Row equilibration	On
Manual control of reassembly	Off
Load constant	On
Constraint constant	On
Mass constant	On
Damping (mass) constant	On
Jacobian constant	On
Constraint Jacobian constant	On

7. Postprocessing

8. Variables

8.1. Boundary

Name	Description	Expression
K_x_chns	Viscous force per area, x component	2 * nx_chns * eta_chns * ux+ny_chns * eta_chns * (uy+vx)
T_x_chns	Total force per area, x component	-nx_chns * p+2 * nx_chns * eta_chns * ux+ny_chns * eta_chns * (uy+vx)
K_y_chns	Viscous force per area, y component	nx_chns * eta_chns * (vx+uy)+2 * ny_chns * eta_chns * vy
T_y_chns	Total force per area, y component	-ny_chns * p+nx_chns * eta_chns * (vx+uy)+2 * ny_chns * eta_chns * vy
ndflux_c_chcd	Normal diffusive flux, c	nx_chcd * dflux_c_x_chcd+ny_chcd * dflux_c_y_chcd
ncflux_c_chcd	Normal convective flux, c	nx_chcd * cflux_c_x_chcd+ny_chcd * cflux_c_y_chcd
ntflux_c_chcd	Normal total flux, c	nx_chcd * tflux_c_x_chcd+ny_chcd * tflux_c_y_chcd

8.2. Subdomain

Name	Description	Expression

U_chns	Velocity field	sqrt(u^2+v^2)
V_chns	Vorticity	vx-uy
divU_chns	Divergence of velocity field	ux+vy
cellRe_chns	Cell Reynolds number	rho_chns * U_chns * h/eta_chns
res_u_chns	Equation residual for u	rho_chns * (u * ux+v * uy)+px-F_x_chns-eta_chns * (2 * uxx+uyy+vxy)
res_tst_u_chns	Variational equation residual for u	nojac(rho_chns) * (nojac(u) * ux+nojac(v) * uy)+px-nojac(eta_chns) * (2 * uxx+uyy+vxy)
res_sc_u_chns	Shock capturing residual for u	rho_chns * (u * ux+v * uy)+px-F_x_chns
res_v_chns	Equation residual for v	rho_chns * (u * vx+v * vy)+py-F_y_chns-eta_chns * (vxx+uyx+2 * vyy)
res_tst_v_chns	Variational equation residual for v	nojac(rho_chns) * (nojac(u) * vx+nojac(v) * vy)+py-nojac(eta_chns) * (vxx+uyx+2 * vyy)
res_sc_v_chns	Shock capturing residual for v	rho_chns * (u * vx+v * vy)+py-F_y_chns
beta_x_chns	Convective field, x component	rho_chns * u
beta_y_chns	Convective field, y component	rho_chns * v
Dm_chns	Mean diffusion coefficient	eta_chns
da_chns	Total time scale factor	rho_chns
grad_c_x_chcd	Concentration gradient, c, x component	cx
dflux_c_x_chcd	Diffusive flux, c, x component	-Dxx_c_chcd * cx-Dxy_c_chcd * cy
cflux_c_x_chcd	Convective flux, c, x	c * u_c_chcd

	component	
tflux_c_x_chcd	Total flux, c, x component	dflux_c_x_chcd+cflux_c_x_chcd
grad_c_y_chcd	Concentration gradient, c, y component	cy
dflux_c_y_chcd	Diffusive flux, c, y component	-Dyx_c_chcd * cx-Dyy_c_chcd * cy
cflux_c_y_chcd	Convective flux, c, y component	c * v_c_chcd
tflux_c_y_chcd	Total flux, c, y component	dflux_c_y_chcd+cflux_c_y_chcd
beta_c_x_chcd	Convective field, c, x component	u_c_chcd
beta_c_y_chcd	Convective field, c, y component	v_c_chcd
grad_c_chcd	Concentration gradient, c	sqrt(grad_c_x_chcd^2+grad_c_y_chcd^2)
dflux_c_chcd	Diffusive flux, c	sqrt(dflux_c_x_chcd^2+dflux_c_y_chcd^2)
cflux_c_chcd	Convective flux, c	sqrt(cflux_c_x_chcd^2+cflux_c_y_chcd^2)
tflux_c_chcd	Total flux, c	sqrt(tflux_c_x_chcd^2+tflux_c_y_chcd^2)
cellPe_c_chcd	Cell Peclet number, c	h * sqrt(beta_c_x_chcd^2+beta_c_y_chcd^2)/Dm_c_chcd
Dm_c_chcd	Mean diffusion coefficient, c	(Dxx_c_chcd * u_c_chcd^2+Dxy_c_chcd * u_c_chcd * v_c_chcd+Dyx_c_chcd * v_c_chcd * u_c_chcd+Dyy_c_chcd * v_c_chcd^2)/(u_c_chcd^2+v_c_chcd^2+eps)
res_c_chcd	Equation residual for c	-Dxx_c_chcd * cxx-Dxy_c_chcd * cxy+cx * u_c_chcd-Dyx_c_chcd * cyx-Dyy_c_chcd * cyy+cy * v_c_chcd-R_c_chcd
res_sc_c_chcd	Shock capturing residual for c	cx * u_c_chcd+cy * v_c_chcd-R_c_chcd
da_c_chcd	Total time scale factor, c	Dts_c_chcd

Vapor transport in diffusion and convection

2. Model Properties

Property	Value
Model name	
Author	
Company	
Department	
Reference	
URL	
Saved date	Feb 19, 2007 6:40:02 PM
Creation date	Feb 6, 2007 4:44:28 PM
COMSOL version	COMSOL 3.3.0.405

File name: C:\Documents and Settings\atclogin\My Documents\MQP\COMSOL\OTALVARO\FUNCTIONAL-1\CVD otalvaro functional.mph

Application modes and modules used in this model:

- Geom1 (Axial symmetry (2D))
  - Incompressible Navier-Stokes (Chemical Engineering Module)
  - Convection and Diffusion (Chemical Engineering Module)

3. Constants

Name	Expression	Value	Description
dcc	2.5e-3		separation betwen two consecutive catalyst bundles
Dn	1.81e-5		bidnary diffusivity of O2 in N2 STP
dw	5e-4		catalyst bundle thickness
k1	7.63e-3		kinetic rate constant
mu	4.3e-5		dynamic viscosity at STP
Mn2	28e-3		nitrogen molecular mass
MO2	32e-3		oygen molecular mass
Pr	1.01325e4		total pressure in reaction chamber

Ra	0.00125		catalyst bundle radius
Rg	8.314		universal gas constant
Te	643.5		average temperature
vo	1.07e-2		superficial velocity at inlet
co	0.02*Pr/Rg/(Te+273)		oxygen concetration at inlet
D	Dn*1.013e5/Pr		corrected diffusivity
Deff	D*(dcc-dw)/dcc		effecitive diffusiviyt accounting for geometry
ro	Pr*(0.02*MO2+0.98*Mn2)/Rg/(Te+273)		overall gas density
ros	2e3		
Re	Ra*vo*ro/mu		reynolds number
Sa	2*(Ra^2+Ra*dw)/Ra^2/dcc		specific area

4. Geometry

Number of geometries: 1

4.1.3. Subdomain mode

5. Geom1

Space dimensions: Axial symmetry (2D)

Independent variables: r, phi, z

5.1. Mesh
5.1.1. Mesh Statistics

Number of degrees of freedom	5500
Number of mesh points	505
Number of elements	886
Triangular	886
Quadrilateral	0
Number of boundary elements	135
Number of vertex elements	14
Minimum element quality	0.754
Element area ratio	0.023

5.2. Application Mode: Incompressible Navier-Stokes (chns)

Application mode type: Incompressible Navier-Stokes (Chemical Engineering Module)

Application mode name: chns

5.2.1. Application Mode Properties

Property	Value
Default element type	Lagrange - P_2 P_1
Analysis type	Stationary
Stress tensor	Total
Corner smoothing	Off
Non-isothermal flow	Off
Turbulence model	None
Non-Newtonian flow	Off
Brinkman on by default	Off
Swirl velocity	Off
Frame	Frame (ref)
Weak constraints	Off

5.2.2. Variables

Dependent variables: u, v, w, p, logk, logd, nrw, nzw

Shape functions: shlag(2,'u'), shlag(2,'v'), shlag(1,'p')

Interior boundaries not active

5.2.3. Boundary Settings

Boundary		3, 8, 10-15	1, 7
Type		No slip	Slip/Symmetry
z-velocity (v0)	m/s	0	0

Boundary	2	9
Type	Inflow/Outflow velocity	Normal flow/Pressure
z-velocity (v0)	**vo**	0

5.2.4. Subdomain Settings

Subdomain		1
Integration order (gporder)		**4 4 2**
Constraint order (cporder)		**2 2 1**
Density (rho)	kg/m^3	**ro**
Dynamic viscosity (eta)	$Pa \cdot s$	**mu**

5.3. Application Mode: Convection and Diffusion (chcd)

Application mode type: Convection and Diffusion (Chemical Engineering Module)

Application mode name: chcd

5.3.1. Application Mode Properties

Property	**Value**
Default element type	Lagrange - Quadratic
Analysis type	Stationary
Equation form	Non-conservative
Equilibrium assumption	Off
Frame	Frame (ref)
Weak constraints	Off

5.3.2. Variables

Dependent variables: c

Shape functions: shlag(2,'c')

Interior boundaries not active

5.3.3. Boundary Settings

Boundary		1, 3-8, 10-11, 13-15	2
Type		Insulation/Symmetry	Concentration
Concentration (c0)	mol/m^3	0	**co**

Boundary	9
Type	Convective flux
Concentration (c0)	**co**

5.3.4. Subdomain Settings

Subdomain		1	2

Diffusion coefficient (D)	m^2/s	**D**	1
dtype	m^2/s	iso	**aniso**
Reaction rate (R)	$mol/(m^3 \cdot s)$	0	**-(k1*Sa)*c^2**
r-velocity (u)	m/s	**u**	0
z-velocity (v)	m/s	**v**	0

6. Solver Settings

Solve using a script: off

Analysis type	Stationary
Auto select solver	Off
Solver	Parametric
Solution form	Automatic
Symmetric	auto
Adaption	Off

6.1. Direct (UMFPACK)

Solver type: Linear system solver

Parameter	**Value**
Pivot threshold	0.1
Memory allocation factor	0.7

6.2. Advanced

Parameter	**Value**
Constraint handling method	Elimination
Null-space function	Automatic
Assembly block size	5000
Use Hermitian transpose of constraint matrix and in symmetry detection	Off
Use complex functions with real input	Off
Stop if error due to undefined operation	On
Type of scaling	Automatic
Manual scaling	
Row equilibration	On
Manual control of reassembly	Off
Load constant	On

Constraint constant	On
Mass constant	On
Damping (mass) constant	On
Jacobian constant	On
Constraint Jacobian constant	On

7. Postprocessing

8. Variables

8.1. Boundary

8.1.1. Boundary 1-3, 7-15

Name	Description	Expression
K_r_chns	Viscous force per area, r component	2 * nr_chns * eta_chns * ur+nz_chns * eta_chns * (uz+vr)
T_r_chns	Total force per area, r component	-nr_chns * p+2 * nr_chns * eta_chns * ur+nz_chns * eta_chns * (uz+vr)
K_z_chns	Viscous force per area, z component	nr_chns * eta_chns * (vr+uz)+2 * nz_chns * eta_chns * vz
T_z_chns	Total force per area, z component	-nz_chns * p+nr_chns * eta_chns * (vr+uz)+2 * nz_chns * eta_chns * vz
ndflux_c_chcd	Normal diffusive flux, c	nr_chcd * dflux_c_r_chcd+nz_chcd * dflux_c_z_chcd
ncflux_c_chcd	Normal convective flux, c	nr_chcd * cflux_c_r_chcd+nz_chcd * cflux_c_z_chcd
ntflux_c_chcd	Normal total flux, c	nr_chcd * tflux_c_r_chcd+nz_chcd * tflux_c_z_chcd

8.1.2. Boundary 4-6

Name	Description	Expression
K_r_chns	Viscous force per area, r component	
T_r_chns	Total force per area, r component	
K_z_chns	Viscous force per area, z component	
T_z_chns	Total force per area, z component	
ndflux_c_chcd	Normal diffusive flux, c	nr_chcd * dflux_c_r_chcd+nz_chcd * dflux_c_z_chcd

ncflux_c_chcd	Normal convective flux, c	nr_chcd * cflux_c_r_chcd+nz_chcd * cflux_c_z_chcd
ntflux_c_chcd	Normal total flux, c	nr_chcd * tflux_c_r_chcd+nz_chcd * tflux_c_z_chcd

8.2. Subdomain

8.2.1. Subdomain 1

Name	Description	Expression
U_chns	Velocity field	sqrt(u^2+v^2)
V_chns	Vorticity	uz-vr
divU_chns	Divergence of velocity field	ur+vz+u/r
cellRe_chns	Cell Reynolds number	rho_chns * U_chns * h/eta_chns
res_u_chns	Equation residual for u	r * (rho_chns * (u * ur+v * uz)+pr-F_r_chns)+2 * eta_chns * (u/r-ur)-eta_chns * (2 * r * urr+r * (uzz+vrz))
res_tst_u_chns	Variational equation residual for u	r * (nojac(rho_chns) * (nojac(u) * ur+nojac(v) * uz)+pr)+2 * nojac(eta_chns) * (u/r-ur)-nojac(eta_chns) * (2 * r * urr+r * (uzz+vrz))
res_sc_u_chns	Shock capturing residual for u	r * (rho_chns * (u * ur+v * uz)+pr-F_r_chns)+2 * eta_chns * (u/r-ur)
res_v_chns	Equation residual for v	r * (rho_chns * (u * vr+v * vz)+pz-F_z_chns)-eta_chns * (r * (vrr+uzr)+2 * r * vzz+uz+vr)
res_tst_v_chns	Variational equation residual for v	r * (nojac(rho_chns) * (nojac(u) * vr+nojac(v) * vz)+pz)-nojac(eta_chns) * (r * (vrr+uzr)+2 * r * vzz+uz+vr)
res_sc_v_chns	Shock capturing residual for v	r * (rho_chns * (u * vr+v * vz)+pz-F_z_chns)
beta_r_chns	Convective field, r component	r * rho_chns * u
beta_z_chns	Convective field, z component	r * rho_chns * v
Dm_chns	Mean diffusion coefficient	r * eta_chns
da_chns	Total time scale factor	r * rho_chns

grad_c_r_chcd	Concentration gradient, c, r component	cr
dflux_c_r_chcd	Diffusive flux, c, r component	-Drr_c_chcd * cr-Drz_c_chcd * cz
cflux_c_r_chcd	Convective flux, c, r component	c * u_c_chcd
tflux_c_r_chcd	Total flux, c, r component	dflux_c_r_chcd+cflux_c_r_chcd
grad_c_z_chcd	Concentration gradient, c, z component	cz
dflux_c_z_chcd	Diffusive flux, c, z component	-Dzr_c_chcd * cr-Dzz_c_chcd * cz
cflux_c_z_chcd	Convective flux, c, z component	c * v_c_chcd
tflux_c_z_chcd	Total flux, c, z component	dflux_c_z_chcd+cflux_c_z_chcd
beta_c_r_chcd	Convective field, c, r component	r * u_c_chcd
beta_c_z_chcd	Convective field, c, z component	r * v_c_chcd
grad_c_chcd	Concentration gradient, c	sqrt(grad_c_r_chcd^2+grad_c_z_chcd^2)
dflux_c_chcd	Diffusive flux, c	sqrt(dflux_c_r_chcd^2+dflux_c_z_chcd^2)
cflux_c_chcd	Convective flux, c	sqrt(cflux_c_r_chcd^2+cflux_c_z_chcd^2)
tflux_c_chcd	Total flux, c	sqrt(tflux_c_r_chcd^2+tflux_c_z_chcd^2)
cellPe_c_chcd	Cell Peclet number, c	h * sqrt(beta_c_r_chcd^2+beta_c_z_chcd^2)/Dm_c_chcd
Dm_c_chcd	Mean diffusion coefficient, c	r * (Drr_c_chcd * u_c_chcd^2+Drz_c_chcd * u_c_chcd * v_c_chcd+Dzr_c_chcd * v_c_chcd * u_c_chcd+Dzz_c_chcd * v_c_chcd^2)/(u_c_chcd^2+v_c_chcd^2+eps)
res_c_chcd	Equation	r * (-Drr_c_chcd * crr-Drz_c_chcd * crz+cr * u_c_chcd-

	residual for c	Dzr_c_chcd * czr-Dzz_c_chcd * czz+cz * v_c_chcd-R_c_chcd)
res_sc_c_chcd	Shock capturing residual for c	r * (cr * u_c_chcd+cz * v_c_chcd-R_c_chcd)
da_c_chcd	Total time scale factor, c	r * Dts_c_chcd

8.2.2. Subdomain 2

Name	Description	Expression
U_chns	Velocity field	
V_chns	Vorticity	
divU_chns	Divergence of velocity field	
cellRe_chns	Cell Reynolds number	
res_u_chns	Equation residual for u	
res_tst_u_chns	Variational equation residual for u	
res_sc_u_chns	Shock capturing residual for u	
res_v_chns	Equation residual for v	
res_tst_v_chns	Variational equation residual for v	
res_sc_v_chns	Shock capturing residual for v	
beta_r_chns	Convective field, r component	
beta_z_chns	Convective field, z component	
Dm_chns	Mean diffusion coefficient	

da_chns	Total time scale factor	
grad_c_r_chcd	Concentration gradient, c, r component	Cr
dflux_c_r_chcd	Diffusive flux, c, r component	-Drr_c_chcd * cr-Drz_c_chcd * cz
cflux_c_r_chcd	Convective flux, c, r component	c * u_c_chcd
tflux_c_r_chcd	Total flux, c, r component	dflux_c_r_chcd+cflux_c_r_chcd
grad_c_z_chcd	Concentration gradient, c, z component	Cz
dflux_c_z_chcd	Diffusive flux, c, z component	-Dzr_c_chcd * cr-Dzz_c_chcd * cz
cflux_c_z_chcd	Convective flux, c, z component	c * v_c_chcd
tflux_c_z_chcd	Total flux, c, z component	dflux_c_z_chcd+cflux_c_z_chcd
beta_c_r_chcd	Convective field, c, r component	r * u_c_chcd
beta_c_z_chcd	Convective field, c, z component	r * v_c_chcd
grad_c_chcd	Concentration gradient, c	sqrt(grad_c_r_chcd^2+grad_c_z_chcd^2)
dflux_c_chcd	Diffusive flux, c	sqrt(dflux_c_r_chcd^2+dflux_c_z_chcd^2)
cflux_c_chcd	Convective flux, c	sqrt(cflux_c_r_chcd^2+cflux_c_z_chcd^2)
tflux_c_chcd	Total flux, c	sqrt(tflux_c_r_chcd^2+tflux_c_z_chcd^2)
cellPe_c_chcd	Cell Peclet number, c	h * sqrt(beta_c_r_chcd^2+beta_c_z_chcd^2)/Dm_c_chcd
Dm_c_chcd	Mean diffusion coefficient, c	r * (Drr_c_chcd * u_c_chcd^2+Drz_c_chcd * u_c_chcd * v_c_chcd+Dzr_c_chcd * v_c_chcd * u_c_chcd+Dzz_c_chcd *

		v_c_chcd^2)/(u_c_chcd^2+v_c_chcd^2+eps)
res_c_chcd	Equation residual for c	r * (-Drr_c_chcd * crr-Drz_c_chcd * crz+cr * u_c_chcd-Dzr_c_chcd * czr-Dzz_c_chcd * czz+cz * v_c_chcd-R_c_chcd)
res_sc_c_chcd	Shock capturing residual for c	r * (cr * u_c_chcd+cz * v_c_chcd-R_c_chcd)
da_c_chcd	Total time scale factor, c	r * Dts_c_chcd

2-D Multi-component Diffusive Flux

2. Model Properties

Property	Value
Model name	
Author	
Company	
Department	
Reference	
URL	
Saved date	Feb 21, 2007 1:16:20 PM
Creation date	Feb 21, 2007 11:37:18 AM
COMSOL version	COMSOL 3.3.0.405

File name: C:\Documents and Settings\atclogin\My Documents\MQP\COMSOL\OTALVARO\TRIAL\TenaZaera\Maxwell-Zaera-feb21.mph

Application modes and modules used in this model:

- Geom1 (2D)
    - Maxwell-Stefan Diffusion and Convection (Chemical Engineering Module)

3. Constants

Name	Expression	Value	Description
k	3.16e-8		
R	8.314		

vN2	1.79e-5		
vO2	1.66e-5		
vZn	9.16e-5		
MO2	3.20e-2		
MN2	28e-3		
MZn	30e-3		
wO2_0	3.01e-4		
wZn_0	5.62e-4		
T0	1258		
p0	1.01325e5		
rho0	p0/R/T0		
DO2_N2	k*T0^1.75/(p0*(vO2^(1/3)+vN2^(1/3))^2)*(1/MO2+1/MN2)^0.5		
DZn_N2	k*T0^1.75/(p0*(vZn^(1/3)+vN2^(1/3))^2)*(1/MZn+1/MN2)^.5		
DO2_Zn	k*T0^1.75/(p0*(vZn^(1/3)+vO2^(1/3))^2)*(1/MZn+1/MN2)^0.5		
R_O2	4.59e-7		
R_Zn	8.6e-7		

4. Geometry

Number of geometries: 1

4.1. Geom1

Space dimensions: 2D

Independent variables: x, y, z

5.1. Scalar Expressions

Name	Expression
M	MO2*x_wO2_chms+MZn*x_wZn_chms+MN2*x_wN2_chms

5.2. Mesh

5.2.1. Mesh Statistics

Number of degrees of freedom	2802
Number of mesh points	369

Number of elements	664
Triangular	664
Quadrilateral	0
Number of boundary elements	72
Number of vertex elements	4
Minimum element quality	0.692
Element area ratio	0.304

5.3. Application Mode: Maxwell-Stefan Diffusion and Convection (chms)

Application mode type: Maxwell-Stefan Diffusion and Convection (Chemical Engineering Module)

Application mode name: chms

5.3.1. Application Mode Properties

Property	**Value**
Default element type	Lagrange - Quadratic
Analysis type	Stationary
Equation form	Conservative
Frame	Frame (ref)
Weak constraints	Off

5.3.2. Variables

Dependent variables: wO2, wZn, wN2

Shape functions: shlag(2,'wO2'), shlag(2,'wZn')

Interior boundaries not active

5.3.3. Boundary Settings

Boundary		2-3	1
Type		Insulation/Symmetry	Mass fraction
Mass fraction (w0)	1	{0;0}	**{'wO2_0';'wZn_0'}**
Inward mass flux (N)	Pa·s/m	{0;0}	{0;0}

Boundary	4

Type	Flux
Mass fraction (w0)	{0;0}
Inward mass flux (N)	**{'-R_O2';'-R_Zn'}**

5.3.4. Subdomain Settings

Subdomain		1
Maxwell-Stefan diffusion coefficient (Dij)	m^2/s	**{1,'DO2_Zn','DO2_N2';1,1,'DZn_N2';1,1,1}**
Molecular weight (M)	kg/mol	**{'MO2';'MZn';'MN2'}**
Temperature (T)	K	**T0**
Density (rho)	kg/m^3	**M*p0/R/T0**
Pressure (P)	Pa	**p0**
#-velocity (u)	m/s	**-dflux_wN2_x_chms/(wN2*rho_chms)**
#-velocity (v)	m/s	**-dflux_wN2_y_chms/(wN2*rho_chms)**

Subdomain initial value		1
Mass fraction, wO2 (wO2)		wO2_0
Mass fraction, wZn (wZn)		wZn_0

6. Solver Settings

Solve using a script: off

Analysis type	Stationary
Auto select solver	On
Solver	Parametric
Solution form	Automatic
Symmetric	auto
Adaption	Off

6.1. Direct (UMFPACK)

Solver type: Linear system solver

Parameter	**Value**
Pivot threshold	0.1
Memory allocation factor	0.7

6.2. Advanced

Parameter	**Value**

Constraint handling method	Elimination
Null-space function	Automatic
Assembly block size	5000
Use Hermitian transpose of constraint matrix and in symmetry detection	Off
Use complex functions with real input	Off
Stop if error due to undefined operation	On
Type of scaling	Automatic
Manual scaling	
Row equilibration	On
Manual control of reassembly	Off
Load constant	On
Constraint constant	On
Mass constant	On
Damping (mass) constant	On
Jacobian constant	On
Constraint Jacobian constant	On

7. Postprocessing

8. Variables

8.1. Boundary

Name	Description	Expression
wN2x	Mass fraction, wN2, x derivative	-wO2x-wZnx
wN2y	Mass fraction, wN2, y derivative	-wO2y-wZny
ndflux_wO2_chms	Normal diffusive flux, wO2	nx_chms * dflux_wO2_x_chms+ny_chms * dflux_wO2_y_chms
ncflux_wO2_chms	Normal convective flux, wO2	nx_chms * cflux_wO2_x_chms+ny_chms * cflux_wO2_y_chms
ntflux_wO2_chms	Normal total flux, wO2	nx_chms * tflux_wO2_x_chms+ny_chms * tflux_wO2_y_chms
ndflux_wZn_chms	Normal diffusive flux, wZn	nx_chms * dflux_wZn_x_chms+ny_chms * dflux_wZn_y_chms
ncflux_wZn_chms	Normal convective flux, wZn	nx_chms * cflux_wZn_x_chms+ny_chms * cflux_wZn_y_chms
ntflux_wZn_chms	Normal total flux,	nx_chms * tflux_wZn_x_chms+ny_chms *

	wZn	tflux_wZn_y_chms
ndflux_wN2_chms	Normal diffusive flux, wN2	nx_chms * dflux_wN2_x_chms+ny_chms * dflux_wN2_y_chms
ncflux_wN2_chms	Normal convective flux, wN2	nx_chms * cflux_wN2_x_chms+ny_chms * cflux_wN2_y_chms
ntflux_wN2_chms	Normal total flux, wN2	nx_chms * tflux_wN2_x_chms+ny_chms * tflux_wN2_y_chms

8.2. Subdomain

Name	Description	Expression
wN2x	Mass fraction, wN2, x derivative	-wO2x-wZnx
wN2y	Mass fraction, wN2, y derivative	-wO2y-wZny
x_wO2_chms	Mole fraction, wO2	wO2/(M_wO2_chms * (wO2/M_wO2_chms+wZn/M_wZn_chms+(1-wO2-wZn)/M_wN2_chms))
x_wZn_chms	Mole fraction, wZn	wZn/(M_wZn_chms * (wO2/M_wO2_chms+wZn/M_wZn_chms+(1-wO2-wZn)/M_wN2_chms))
x_wN2_chms	Mole fraction, wN2	(1-wO2-wZn)/(M_wN2_chms * (wO2/M_wO2_chms+wZn/M_wZn_chms+(1-wO2-wZn)/M_wN2_chms))
DE11_chms	Diffusivity	(wN2^2 * x_wO2_chms * x_wZn_chms/D12_chms+wZn^2 * x_wO2_chms * x_wN2_chms/D13_chms+(wZn+wN2)^2 * x_wZn_chms * x_wN2_chms/D23_chms)/(x_wZn_chms * x_wO2_chms^2 * x_wN2_chms/(D12_chms * D13_chms)+x_wO2_chms * x_wZn_chms^2 * x_wN2_chms/(D12_chms * D23_chms)+x_wO2_chms * x_wZn_chms * x_wN2_chms^2/(D13_chms * D23_chms))
DE12_chms	Diffusivity	(wN2^2 * x_wO2_chms * x_wZn_chms/D12_chms-wZn * (wO2+wN2) * x_wO2_chms * x_wN2_chms/D13_chms-wO2 * (wZn+wN2) * x_wZn_chms * x_wN2_chms/D23_chms)/(x_wZn_chms * x_wO2_chms^2 * x_wN2_chms/(D12_chms *

		D13_chms)+x_wO2_chms * x_wZn_chms^2 * x_wN2_chms/(D12_chms * D23_chms)+x_wO2_chms * x_wZn_chms * x_wN2_chms^2/(D13_chms * D23_chms))
DE13_chms	Diffusivity	(wZn^2 * x_wO2_chms * x_wN2_chms/D13_chms-wN2 * (wO2+wZn) * x_wO2_chms * x_wZn_chms/D12_chms-wO2 * (wN2+wZn) * x_wZn_chms * x_wN2_chms/D23_chms)/(x_wZn_chms * x_wO2_chms^2 * x_wN2_chms/(D12_chms * D13_chms)+x_wO2_chms * x_wZn_chms^2 * x_wN2_chms/(D12_chms * D23_chms)+x_wO2_chms * x_wZn_chms * x_wN2_chms^2/(D13_chms * D23_chms))
DE21_chms	Diffusivity	(wN2^2 * x_wO2_chms * x_wZn_chms/D12_chms-wZn * (wO2+wN2) * x_wO2_chms * x_wN2_chms/D13_chms-wO2 * (wZn+wN2) * x_wZn_chms * x_wN2_chms/D23_chms)/(x_wZn_chms * x_wO2_chms^2 * x_wN2_chms/(D12_chms * D13_chms)+x_wO2_chms * x_wZn_chms^2 * x_wN2_chms/(D12_chms * D23_chms)+x_wO2_chms * x_wZn_chms * x_wN2_chms^2/(D13_chms * D23_chms))
DE22_chms	Diffusivity	(wN2^2 * x_wO2_chms * x_wZn_chms/D12_chms+wO2^2 * x_wZn_chms * x_wN2_chms/D23_chms+(wO2+wN2)^2 * x_wO2_chms * x_wN2_chms/D13_chms)/(x_wZn_chms * x_wO2_chms^2 * x_wN2_chms/(D12_chms * D13_chms)+x_wO2_chms * x_wZn_chms^2 * x_wN2_chms/(D12_chms * D23_chms)+x_wO2_chms * x_wZn_chms * x_wN2_chms^2/(D13_chms * D23_chms))
DE23_chms	Diffusivity	(wO2^2 * x_wZn_chms * x_wN2_chms/D23_chms-wN2 * (wZn+wO2) * x_wO2_chms * x_wZn_chms/D12_chms-wZn * (wN2+wO2) * x_wO2_chms * x_wN2_chms/D13_chms)/(x_wZn_chms * x_wO2_chms^2 * x_wN2_chms/(D12_chms * D13_chms)+x_wO2_chms * x_wZn_chms^2 * x_wN2_chms/(D12_chms * D23_chms)+x_wO2_chms * x_wZn_chms * x_wN2_chms^2/(D13_chms * D23_chms))

DE31_chms	Diffusivity	(wZn^2 * x_wO2_chms * x_wN2_chms/D13_chms-wN2 * (wO2+wZn) * x_wO2_chms * x_wZn_chms/D12_chms-wO2 * (wN2+wZn) * x_wZn_chms * x_wN2_chms/D23_chms)/(x_wZn_chms * x_wO2_chms^2 * x_wN2_chms/(D12_chms * D13_chms)+x_wO2_chms * x_wZn_chms^2 * x_wN2_chms/(D12_chms * D23_chms)+x_wO2_chms * x_wZn_chms * x_wN2_chms^2/(D13_chms * D23_chms))
DE32_chms	Diffusivity	(wO2^2 * x_wZn_chms * x_wN2_chms/D23_chms-wN2 * (wZn+wO2) * x_wO2_chms * x_wZn_chms/D12_chms-wZn * (wN2+wO2) * x_wO2_chms * x_wN2_chms/D13_chms)/(x_wZn_chms * x_wO2_chms^2 * x_wN2_chms/(D12_chms * D13_chms)+x_wO2_chms * x_wZn_chms^2 * x_wN2_chms/(D12_chms * D23_chms)+x_wO2_chms * x_wZn_chms * x_wN2_chms^2/(D13_chms * D23_chms))
DE33_chms	Diffusivity	(wZn^2 * x_wO2_chms * x_wN2_chms/D13_chms+wO2^2 * x_wZn_chms * x_wN2_chms/D23_chms+(wO2+wZn)^2 * x_wO2_chms * x_wZn_chms/D12_chms)/(x_wZn_chms * x_wO2_chms^2 * x_wN2_chms/(D12_chms * D13_chms)+x_wO2_chms * x_wZn_chms^2 * x_wN2_chms/(D12_chms * D23_chms)+x_wO2_chms * x_wZn_chms * x_wN2_chms^2/(D13_chms * D23_chms))
grad_wO2_x_chms	Mass fraction gradient, wO2, x	wO2x
dflux_wO2_x_chms	Diffusive flux, wO2, x component	-rho_chms * wO2 * (DE11_chms * diff(wO2/(M_wO2_chms * (wO2/M_wO2_chms+wZn/M_wZn_chms+(1-wO2-wZn)/M_wN2_chms)),x)+DE12_chms * diff(wZn/(M_wZn_chms * (wO2/M_wO2_chms+wZn/M_wZn_chms+(1-wO2-wZn)/M_wN2_chms)),x)+DE13_chms * diff((1-wO2-wZn)/(M_wN2_chms * (wO2/M_wO2_chms+wZn/M_wZn_chms+(1-wO2-wZn)/M_wN2_chms)),x)+DE11_chms * (x_wO2_chms-wO2) *

		diff(P_chms,x)/P_chms+DE12_chms * (x_wZn_chms-wZn) * diff(P_chms,x)/P_chms+DE13_chms * (x_wN2_chms-wN2) * diff(P_chms,x)/P_chms)-DiT_wO2_chms * diff(T_chms,x)/T_chms
cflux_wO2_x_chms	Convective flux, wO2, x component	rho_chms * wO2 * u_chms
tflux_wO2_x_chms	Total flux, wO2, x component	dflux_wO2_x_chms+cflux_wO2_x_chms
grad_wO2_y_chms	Mass fraction gradient, wO2, y	wO2y
dflux_wO2_y_chms	Diffusive flux, wO2, y component	-rho_chms * wO2 * (DE11_chms * diff(wO2/(M_wO2_chms * (wO2/M_wO2_chms+wZn/M_wZn_chms+(1-wO2-wZn)/M_wN2_chms)),y)+DE12_chms * diff(wZn/(M_wZn_chms * (wO2/M_wO2_chms+wZn/M_wZn_chms+(1-wO2-wZn)/M_wN2_chms)),y)+DE13_chms * diff((1-wO2-wZn)/(M_wN2_chms * (wO2/M_wO2_chms+wZn/M_wZn_chms+(1-wO2-wZn)/M_wN2_chms)),y)+DE11_chms * (x_wO2_chms-wO2) * diff(P_chms,y)/P_chms+DE12_chms * (x_wZn_chms-wZn) * diff(P_chms,y)/P_chms+DE13_chms * (x_wN2_chms-wN2) * diff(P_chms,y)/P_chms)-DiT_wO2_chms * diff(T_chms,y)/T_chms
cflux_wO2_y_chms	Convective flux, wO2, y component	rho_chms * wO2 * v_chms
tflux_wO2_y_chms	Total flux, wO2, y component	dflux_wO2_y_chms+cflux_wO2_y_chms
grad_wO2_chms	Mass fraction gradient, wO2	sqrt(grad_wO2_x_chms^2+grad_wO2_y_chms^2)

dflux_wO2_chms	Diffusive flux, wO2	sqrt(dflux_wO2_x_chms^2+dflux_wO2_y_chms^2)
cflux_wO2_chms	Convective flux, wO2	sqrt(cflux_wO2_x_chms^2+cflux_wO2_y_chms^2)
tflux_wO2_chms	Total flux, wO2	sqrt(tflux_wO2_x_chms^2+tflux_wO2_y_chms^2)
grad_wZn_x_chms	Mass fraction gradient, wZn, x	wZnx
dflux_wZn_x_chms	Diffusive flux, wZn, x component	-rho_chms * wZn * (DE21_chms * diff(wO2/(M_wO2_chms * (wO2/M_wO2_chms+wZn/M_wZn_chms+(1-wO2-wZn)/M_wN2_chms)),x)+DE22_chms * diff(wZn/(M_wZn_chms * (wO2/M_wO2_chms+wZn/M_wZn_chms+(1-wO2-wZn)/M_wN2_chms)),x)+DE23_chms * diff((1-wO2-wZn)/(M_wN2_chms * (wO2/M_wO2_chms+wZn/M_wZn_chms+(1-wO2-wZn)/M_wN2_chms)),x)+DE21_chms * (x_wO2_chms-wO2) * diff(P_chms,x)/P_chms+DE22_chms * (x_wZn_chms-wZn) * diff(P_chms,x)/P_chms+DE23_chms * (x_wN2_chms-wN2) * diff(P_chms,x)/P_chms)-DiT_wZn_chms * diff(T_chms,x)/T_chms
cflux_wZn_x_chms	Convective flux, wZn, x component	rho_chms * wZn * u_chms
tflux_wZn_x_chms	Total flux, wZn, x component	dflux_wZn_x_chms+cflux_wZn_x_chms
grad_wZn_y_chms	Mass fraction gradient, wZn, y	wZny
dflux_wZn_y_chms	Diffusive flux, wZn, y component	-rho_chms * wZn * (DE21_chms * diff(wO2/(M_wO2_chms * (wO2/M_wO2_chms+wZn/M_wZn_chms+(1-wO2-wZn)/M_wN2_chms)),y)+DE22_chms * diff(wZn/(M_wZn_chms * (wO2/M_wO2_chms+wZn/M_wZn_chms+(1-wO2-wZn)/M_wN2_chms)),y)+DE23_chms * diff((1-wO2-

		wZn)/(M_wN2_chms * (wO2/M_wO2_chms+wZn/M_wZn_chms+(1-wO2-wZn)/M_wN2_chms)),y)+DE21_chms * (x_wO2_chms-wO2) * diff(P_chms,y)/P_chms+DE22_chms * (x_wZn_chms-wZn) * diff(P_chms,y)/P_chms+DE23_chms * (x_wN2_chms-wN2) * diff(P_chms,y)/P_chms)-DiT_wZn_chms * diff(T_chms,y)/T_chms
cflux_wZn_y_chms	Convective flux, wZn, y component	rho_chms * wZn * v_chms
tflux_wZn_y_chms	Total flux, wZn, y component	dflux_wZn_y_chms+cflux_wZn_y_chms
grad_wZn_chms	Mass fraction gradient, wZn	sqrt(grad_wZn_x_chms^2+grad_wZn_y_chms^2)
dflux_wZn_chms	Diffusive flux, wZn	sqrt(dflux_wZn_x_chms^2+dflux_wZn_y_chms^2)
cflux_wZn_chms	Convective flux, wZn	sqrt(cflux_wZn_x_chms^2+cflux_wZn_y_chms^2)
tflux_wZn_chms	Total flux, wZn	sqrt(tflux_wZn_x_chms^2+tflux_wZn_y_chms^2)
grad_wN2_x_chms	Mass fraction gradient, wN2, x	wN2x
dflux_wN2_x_chms	Diffusive flux, wN2, x component	-rho_chms * wN2 * (DE31_chms * diff(wO2/(M_wO2_chms * (wO2/M_wO2_chms+wZn/M_wZn_chms+(1-wO2-wZn)/M_wN2_chms)),x)+DE32_chms * diff(wZn/(M_wZn_chms * (wO2/M_wO2_chms+wZn/M_wZn_chms+(1-wO2-wZn)/M_wN2_chms)),x)+DE33_chms * diff((1-wO2-wZn)/(M_wN2_chms * (wO2/M_wO2_chms+wZn/M_wZn_chms+(1-wO2-wZn)/M_wN2_chms)),x)+DE31_chms * (x_wO2_chms-wO2) * diff(P_chms,x)/P_chms+DE32_chms * (x_wZn_chms-wZn) * diff(P_chms,x)/P_chms+DE33_chms *

		(x_wN2_chms-wN2) * diff(P_chms,x)/P_chms)-DiT_wN2_chms * diff(T_chms,x)/T_chms
cflux_wN2_x_chms	Convective flux, wN2, x component	rho_chms * wN2 * u_chms
tflux_wN2_x_chms	Total flux, wN2, x component	dflux_wN2_x_chms+cflux_wN2_x_chms
grad_wN2_y_chms	Mass fraction gradient, wN2, y	wN2y
dflux_wN2_y_chms	Diffusive flux, wN2, y component	-rho_chms * wN2 * (DE31_chms * diff(wO2/(M_wO2_chms * (wO2/M_wO2_chms+wZn/M_wZn_chms+(1-wO2-wZn)/M_wN2_chms)),y)+DE32_chms * diff(wZn/(M_wZn_chms * (wO2/M_wO2_chms+wZn/M_wZn_chms+(1-wO2-wZn)/M_wN2_chms)),y)+DE33_chms * diff((1-wO2-wZn)/(M_wN2_chms * (wO2/M_wO2_chms+wZn/M_wZn_chms+(1-wO2-wZn)/M_wN2_chms)),y)+DE31_chms * (x_wO2_chms-wO2) * diff(P_chms,y)/P_chms+DE32_chms * (x_wZn_chms-wZn) * diff(P_chms,y)/P_chms+DE33_chms * (x_wN2_chms-wN2) * diff(P_chms,y)/P_chms)-DiT_wN2_chms * diff(T_chms,y)/T_chms
cflux_wN2_y_chms	Convective flux, wN2, y component	rho_chms * wN2 * v_chms
tflux_wN2_y_chms	Total flux, wN2, y component	dflux_wN2_y_chms+cflux_wN2_y_chms
grad_wN2_chms	Mass fraction gradient, wN2	sqrt(grad_wN2_x_chms^2+grad_wN2_y_chms^2)
dflux_wN2_chms	Diffusive flux, wN2	sqrt(dflux_wN2_x_chms^2+dflux_wN2_y_chms^2)
cflux_wN2_chms	Convective	sqrt(cflux_wN2_x_chms^2+cflux_wN2_y_chms^2)

	flux, wN2	
tflux_wN2_chms	Total flux, wN2	sqrt(tflux_wN2_x_chms^2+tflux_wN2_y_chms^2)

Thermal Fluid Interactions

2. Model Properties

Property	Value
Model name	
Author	
Company	
Department	
Reference	
URL	
Saved date	Feb 23, 2007 10:31:24 AM
Creation date	Feb 23, 2007 9:23:09 AM
COMSOL version	COMSOL 3.3.0.405

File name: C:\Documents and Settings\atclogin\My Documents\MQP\COMSOL\OTALVARO\TRIAL\Non-isothermal\otalvaro-nonisothermal-true.mph

Application modes and modules used in this model:

- Geom1 (Axial symmetry (2D))
  - Non-Isothermal Flow
  - General Heat Transfer (Heat Transfer Module)

3. Constants

Name	Expression	Value	Description
v_max	1.07e-2	0.0107	inlet superficial axial velocity
Tin	720+273	993	inlet reactor temperature

4. Geometry

Number of geometries: 1

5. Geom1

Space dimensions: Axial symmetry (2D)

Independent variables: r, phi, z

5.1. Mesh

5.1.1. Mesh Statistics

Number of degrees of freedom	55687
Number of mesh points	4402
Number of elements	8292
Triangular	8292
Quadrilateral	0
Number of boundary elements	968
Number of vertex elements	6
Minimum element quality	0.47
Element area ratio	0.002

5.2. Application Mode: Non-Isothermal Flow (chns)

Application mode type: Non-Isothermal Flow

Application mode name: chns

5.2.1. Application Mode Properties

Property	**Value**
Default element type	Lagrange - P_2 P_1
Analysis type	Stationary
Stress tensor	Total
Corner smoothing	Off
Non-isothermal flow	On
Turbulence model	None
Non-Newtonian flow	Off
Brinkman on by default	Off
Swirl velocity	Off
Frame	Frame (ref)
Weak constraints	Off

5.2.2. Variables

Dependent variables: u, v, w, p, logk, logd, nrw, nzw

Shape functions: shlag(2,'u'), shlag(2,'v'), shlag(1,'p')

Interior boundaries not active

5.2.3. Boundary Settings

Boundary		1	2
Type		Axial symmetry	Inflow/Outflow velocity
z-velocity (v0)	m/s	0	**v_max*4*s*(1-s)**
Pressure (p0)	Pa	0	0

Boundary	3	5-7
Type	Normal flow/Pressure	No slip
z-velocity (v0)	0	0
Pressure (p0)	**1.01325e5**	0

5.2.4. Subdomain Settings

Subdomain		1	2
Integration order (gporder)		**4 4 2**	**4 4 2**
Constraint order (cporder)		**2 2 1**	**2 2 1**
Density (rho)	kg/m^3	**null (Air, 1 atm)**	1
Dynamic viscosity (eta)	$Pa \cdot s$	**null (Air, 1 atm)**	1

5.3. Application Mode: General Heat Transfer (htgh)

Application mode type: General Heat Transfer (Heat Transfer Module)

Application mode name: htgh

5.3.1. Scalar Variables

Name	Variable	Value	Description
sigma	sigma_htgh	5.67e-8	Stefan-Boltzmann constant

5.3.2. Application Mode Properties

Property	**Value**
Default element type	Lagrange - T_2 J_1
Analysis type	Stationary

Equation form	Non-conservative
Out-of-plane heat transfer	Disabled
Surface-to-surface radiation method	Hemicube
Radiation integration order	4
Radiation resolution	256
Cache view factors	Auto
Turbulence model	None
Predefined multiphysics application	Off
Frame	Frame (ref)
Weak constraints	Off

5.3.3. Variables

Dependent variables: T, J

Shape functions: shlag(1,'J'), shlag(2,'T')

Interior boundaries not active

5.3.4. Boundary Settings

Boundary		1	2, 5
Type		Axial symmetry	Temperature
Shape functions (shape)		**shlag(1,'J') shlag(2,'T')**	**shlag(1,'J') shlag(2,'T')**
Temperature (T0)	K	273.15	**Tin**

Boundary	3	6-7
Type	Convective flux	Thermal insulation
Shape functions (shape)	**shlag(1,'J') shlag(2,'T')**	**shlag(1,'J') shlag(2,'T')**
Temperature (T0)	**Tout**	273.15

5.3.5. Subdomain Settings

Subdomain		1	2
Shape functions (shape)		**shlag(1,'J') shlag(2,'T')**	**shlag(1,'J') shlag(2,'T')**
name			**default**
Enable convective heat transfer (convOn)		**1**	**1**
Thermal conductivity (k)	W/(m·K)	**null (Air, 1 atm)**	400

Density (rho)	kg/m^3	**null (Air, 1 atm)**	8700
Heat capacity (C)	J/(kg·K)	**null (Air, 1 atm)**	385
r-velocity (u)	m/s	**u**	**u**
z-velocity (v)	m/s	**v**	**v**

Subdomain initial value		1	2
Temperature (T)	K	Tin	Tin

6. Materials/Coefficients Library

6.1. Glass (quartz)

Parameter	**Value**
Relative permittivity (epsilonr)	4.2
Relative permeability (mur)	1
Refractive index (n)	2.05
Electrical conductivity (sigma)	1e-14[S/m]

6.2. Glass (quartz)

Parameter	**Value**
Relative permittivity (epsilonr)	4.2
Relative permeability (mur)	1
Refractive index (n)	2.05
Electrical conductivity (sigma)	1e-14[S/m]

6.3. Air, 1 atm

Parameter	**Value**
Heat capacity (C)	Cp(T[1/K])[J/(kg*K)]
Dynamic viscosity (eta)	eta(T[1/K])[Pa*s]
Thermal conductivity (k)	k(T[1/K])[W/(m*K)]
Kinematic viscosity (nu0)	nu0(T[1/K])[m^2/s]
Density (rho)	rho(p[1/Pa],T[1/K])[kg/m^3]

7. Solver Settings

Solve using a script: off

Analysis type	Stationary
Auto select solver	On
Solver	Stationary

Solution form	Automatic
Symmetric	auto
Adaption	Off

7.1. Direct (UMFPACK)

Solver type: Linear system solver

Parameter	Value
Pivot threshold	0.1
Memory allocation factor	0.7

7.2. Advanced

Parameter	Value
Constraint handling method	Elimination
Null-space function	Automatic
Assembly block size	5000
Use Hermitian transpose of constraint matrix and in symmetry detection	Off
Use complex functions with real input	Off
Stop if error due to undefined operation	On
Type of scaling	None
Manual scaling	
Row equilibration	On
Manual control of reassembly	Off
Load constant	On
Constraint constant	On
Mass constant	On
Damping (mass) constant	On
Jacobian constant	On
Constraint Jacobian constant	On

8. Postprocessing

9. Variables

9.1. Boundary

Name	Description	Expression
K_r_chns	Viscous force per area, r component	nr_chns * (2 * eta_chns * ur-(2 * eta_chns/3-kappadv_chns) * divU_chns)+nz_chns * eta_chns *

		(uz+vr)
T_r_chns	Total force per area, r component	-nr_chns * p+nr_chns * (2 * eta_chns * ur-(2 * eta_chns/3-kappadv_chns) * divU_chns)+nz_chns * eta_chns * (uz+vr)
K_z_chns	Viscous force per area, z component	nr_chns * eta_chns * (vr+uz)+nz_chns * (2 * eta_chns * vz-(2 * eta_chns/3-kappadv_chns) * divU_chns)
T_z_chns	Total force per area, z component	-nz_chns * p+nr_chns * eta_chns * (vr+uz)+nz_chns * (2 * eta_chns * vz-(2 * eta_chns/3-kappadv_chns) * divU_chns)
ndflux_htgh	Normal conductive heat flux	nr_htgh * dflux_r_htgh+nz_htgh * dflux_z_htgh
ncflux_htgh	Normal convective heat flux	rho_htgh * C_htgh * T * (nr_htgh * u_htgh+nz_htgh * v_htgh)
ntflux_htgh	Normal total heat flux	ndflux_htgh+ncflux_htgh

9.2. Subdomain

Name	Description	Expression
U_chns	Velocity field	sqrt(u^2+v^2)
V_chns	Vorticity	uz-vr
divU_chns	Divergence of velocity field	ur+vz+u/r
cellRe_chns	Cell Reynolds number	rho_chns * U_chns * h/eta_chns
res_u_chns	Equation residual for u	r * (rho_chns * (u * ur+v * uz)+pr-F_r_chns)+2 * eta_chns * (u/r-ur)-eta_chns * (2 * r * urr+r * (uzz+vrz))+(2 * eta_chns/3-kappadv_chns) * (r * urr+r * vzr+ur-u/r)
res_tst_u_chns	Variational equation residual for u	r * (nojac(rho_chns) * (nojac(u) * ur+nojac(v) * uz)+pr)+2 * nojac(eta_chns) * (u/r-ur)-nojac(eta_chns) * (2 * r * urr+r * (uzz+vrz))+nojac(2 * eta_chns/3-kappadv_chns) * (r * urr+r * vzr+ur-u/r)
res_sc_u_chns	Shock capturing residual for u	r * (rho_chns * (u * ur+v * uz)+pr-F_r_chns)+2 * eta_chns * (u/r-ur)
res_v_chns	Equation residual for v	r * (rho_chns * (u * vr+v * vz)+pz-F_z_chns)-eta_chns * (r * (vrr+uzr)+2 * r * vzz+uz+vr)+(2 * eta_chns/3-kappadv_chns) * (r * urz+r * vzz+uz)
res_tst_v_chns	Variational	r * (nojac(rho_chns) * (nojac(u) * vr+nojac(v) * vz)+pz)-

	equation residual for v	nojac(eta_chns) * (r * (vrr+uzr)+2 * r * vzz+uz+vr)+nojac(2 * eta_chns/3-kappadv_chns) * (r * urz+r * vzz+uz)
res_sc_v_chns	Shock capturing residual for v	r * (rho_chns * (u * vr+v * vz)+pz-F_z_chns)
beta_r_chns	Convective field, r component	r * rho_chns * u
beta_z_chns	Convective field, z component	r * rho_chns * v
Dm_chns	Mean diffusion coefficient	r * eta_chns
da_chns	Total time scale factor	r * rho_chns
gradT_htgh	Temperature gradient	sqrt(Tr^2+Tz^2)
da_htgh	Total time scale factor	r * Dts_htgh * rho_htgh * C_htgh
dflux_r_htgh	Conductive heat flux, r component	-krr_htgh * Tr-krz_htgh * Tz
cflux_r_htgh	Convective heat flux, r component	rho_htgh * C_htgh * T * u_htgh
tflux_r_htgh	Total heat flux, r component	dflux_r_htgh+cflux_r_htgh
beta_r_htgh	Convective field, r component	r * rho_htgh * C_htgh * u_htgh
dflux_z_htgh	Conductive heat flux, z component	-kzr_htgh * Tr-kzz_htgh * Tz
cflux_z_htgh	Convective heat flux, z component	rho_htgh * C_htgh * T * v_htgh
tflux_z_htgh	Total heat flux, z	dflux_z_htgh+cflux_z_htgh

	component	
beta_z_htgh	Convective field, z component	r * rho_htgh * C_htgh * v_htgh
dflux_htgh	Conductive heat flux	sqrt(dflux_r_htgh^2+dflux_z_htgh^2)
cflux_htgh	Convective heat flux	sqrt(cflux_r_htgh^2+cflux_z_htgh^2)
tflux_htgh	Total heat flux	sqrt(tflux_r_htgh^2+tflux_z_htgh^2)
Dm_htgh	Mean diffusion coefficient	r * (krr_htgh * beta_r_htgh^2+krz_htgh * beta_r_htgh * beta_z_htgh+kzr_htgh * beta_z_htgh * beta_r_htgh+kzz_htgh * beta_z_htgh^2)/(beta_r_htgh^2+beta_z_htgh^2+eps)
cellPe_htgh	Cell Peclet number	h * sqrt(beta_r_htgh^2+beta_z_htgh^2)/(Dm_htgh+eps)
res_htgh	Equation residual	r * (-krr_htgh * Trr-krz_htgh * Trz+rho_htgh * C_htgh * u_htgh * Tr-kzr_htgh * Tzr-kzz_htgh * Tzz+rho_htgh * C_htgh * v_htgh * Tz-Q_htgh)
res_sc_htgh	Shock capturing residual	r * (rho_htgh * C_htgh * u_htgh * Tr+rho_htgh * C_htgh * v_htgh * Tz-Q_htgh)

Alt:Go to the postprocessing section
Address:#post
Source:otalvaro-nonisothermal-report_rep/post.png
Alt:Go to the postprocessing section
Address:#post
Source:otalvaro-nonisothermal-report_rep/post.png

[i] Xing, Tal and Stern, Fred. “Introduction to Computational Fluid Dynamics.” Mechanics of Fluids & Transport Processes, University of Iowa, 2003.